Performance Evaluation, Emulation, and Control of Cross-Flow Hydrokinetic Turbines

Robert J. Cavagnaro

A dissertation submitted in partial fulfillment of the
requirements for the degree of

Doctor of Philosophy

University of Washington

2016

Reading Committee:

Brian L. Polagye, Chair

Brian C. Fabien

Daniel S. Kirschen

Program Authorized to Offer Degree:
Mechanical Engineering

University of Washington

Abstract

Performance Evaluation, Emulation, and Control of Cross-Flow Hydrokinetic Turbines

Robert J. Cavagnaro

Chair of the Supervisory Committee:
Professor Brian L. Polagye
Mechanical Engineering

Cross-flow hydrokinetic turbines are a promising option for effectively harvesting energy from fast-flowing streams or currents. This work describes the dynamics of such turbines, analyzes techniques used to scale turbine properties for prototyping, determines and demonstrates the limits of stability for cross-flow rotors, and discusses means and objectives of turbine control. This involves a progression from the analysis of a laboratory-scale prototype turbine to the emulation of a field-scale commercial turbine under realistic control. Understanding of turbine and system component dynamics and performance is leveraged at each phase, with the ultimate goal of enhancing the efficacy of prototype testing and enabling safer, more advanced control techniques.

Novel control strategies are under development to utilize low-speed operation (slower than at maximum power point) as a means of shedding power under rated conditions. However, operation in this regime may be unstable. An experiment designed to characterize the stability of a laboratory-scale cross-flow turbine operating near a critically low speed yields evidence that system stall (complete loss of ability to rotate) occurs due, in part, to interactions with turbulent decreases in flow speed. The turbine is capable of maintaining 'stable' operation at critical speed for short duration (typically less than 10 s), as described by exponential decay. The presence of accelerated 'bypass' flow around the rotor and decelerated 'induction' region directly upstream of the rotor, both predicted by linear momentum theory, are observed and quantified with particle image velocimetry (PIV) measurements conducted upstream of the turbine. Additionally, general agreement is seen between PIV inflow measurements and those obtained by an advection-corrected acoustic Doppler velocimeter (ADV) further upstream. Definitive evidence linking observable flow events to the onset of system stall is not found. However, a link between turbulent kinetic energy of the flow, the system time constant, and the turbine's dynamic response to turbulence indicates changes in the flow occurring over a horizon of several seconds create the conditions under which system stall is likely.

Performance of a turbine at small (prototype) geometric scale may be prone to undesirable effects due to operation at low Reynolds number and in the presence of high channel blockage. Therefore, testing at larger scale, in open water is desirable. A cross-flow hydrokinetic turbine with a projected area (product of blade span and rotor diameter) of 0.7 m^2 is evaluated in open-water tow trials at three inflow speeds ranging from 1.0 m/s to 2.1 m/s. Measurements of the inflow velocity, the rotor mechanical power, and electrical power output of a complete power take-off (PTO) system are utilized to determine the rotor hydrodynamic efficiency (maximum of 17%) and total system efficiency (maximum of 9%). A lab-based dynamometry method yields individual component and total PTO efficiencies, shown to have high variability and strong influence on total system efficiency. The method of tow-testing is found effective, and when combined with PTO characterization, steady-state performance can be inferred solely from inflow velocity and turbine rotation rate.

Dynamic efficiencies of PTO components can effect the overall efficiency of a turbine system, a result from field characterization. Thus, the ability to evaluate such components and their potential effects on turbine performance prior to field deployment is desirable. Before attempting control experiments with actual turbines, hardware-in-the-loop testing on controllable motor-generator sets or electromechanical emulation machines (EEMs) are explored to better understand power take-off response. The emulator control dynamic equations are presented, methods for scaling turbine parameters are developed and evaluated, and experimental results are presented from three EEMs programmed to emulate the same cross-flow turbine. Although hardware platforms and control implementations varied, results show that each EEM is successful in emulating the turbine model at different power levels, thus demonstrating the general feasibility of the approach. However, performance of motor control under torque command, current command, or speed command differed; torque methods required accurate characterization of the motors while speed methods utilized encoder feedback and more accurately tracked turbine dynamics. In a demonstration of an EEM for evaluating a hydrokinetic turbine implementation, a controller is used to track the maximum power-point of the turbine in response to turbulence. Utilizing realistic inflow conditions and control laws, the emulator dynamic speed response is shown to agree well at low frequencies with simulation but to deviate at high frequencies.

The efficacy of an electromechanical emulator as an accurate representation of a fielded turbine is evaluated. A commercial horizontally-oriented cross-flow turbine is dynamically emulated on hardware to investigate control strategies and grid integration. A representative inflow time-series with a mean of 2 m/s is generated from high-resolution flow measurements of a riverine site and is used to drive emulation. Power output during emulation under similar input and loading conditions yields agreement with field measurements to within 3% at high power, near-optimal levels. Constant tip-speed ratio and constant speed proportional plus integral control schemes are compared to optimal nonlinear control and constant resistance regulation. All controllers yield similar results in terms of overall system efficiency. The emulated turbine is more responsive to turbulent inflow than the field turbine, as the model utilized to drive emulation does not account for a smoothing effect of turbulent fluctuations over the span of the fielded turbine's rotors. The turbine has a lower inertia than the demand of an isolated grid, indicating a secondary source of power with a similar frequency response is necessary if a single turbine cannot meet the entire demand.

Major contributions of this work include exploration of the system time constant as an indicator of turbine dynamic response, evidence a turbine experiences system stall probabilistically, a reduced-complexity field performance characterization methodology, and demonstration of the effectiveness of electromechanical emulators at replicating turbine dynamics.

TABLE OF CONTENTS

LIST OF FIGURES

LIST OF TABLES

Table Number Page

NOMENCLATURE

η_b	Gearbox efficiency
η_g	Generator efficiency
η_m	Miscellaneous efficiency
η_s	Total system efficiency
γ	Time constant scale factor
$\hat{U}_\infty$	Turbulent fluctuation speed
κ	Scale factor
λ	Tip-speed ratio
λ^*	Tip-speed ratio at MPP
λ_c	Critical tip-speed ratio (MTP)
μ	Dynamic viscosity
ν	Kinematic viscosity
ω_e	Emulator rotation rate
ω_g	Generator speed
ω_s	Generator synchronous speed
ω_t	Turbine rotation rate
ϕ	Helical sweep angle
ρ	Water density
σ	Rotor solidity ratio
σ_U	Standard deviation of flow speed

τ	Discrete time step
τ_c	Control torque
τ_g	Generator torque
τ_h	Hydrodynamic torque
τ_{em}	Emulator torque
θ	Rotor angular position
θ_p	Helical pitch angle
$\tilde{\omega}_g$	Dynamometry generator rotation rate
$\tilde{\tau}_g$	Dynamometry generator torque
$\tilde{I}$	Dynamometry current
$\tilde{V}$	Dynamometry voltage
ζ	Turbine mechanical time constant
A	Turbine projected area
A_f	Cross-sectional area of flume
A_s	Projected area of in-water test apparatus
B_e	Emulator damping coefficient
B_{eq}	Equivalent damping coefficient
c	Blade chord length
C_P	Coefficient of performance
C_Q	Coefficient of torque
D	Turbine rotor diameter
f	Turbulent frequency
f_{AC}	Frequency of AC power
g	Gravitational acceleration

$G1$	Transfer function: turbulent fluctuations to change in rotor speed
$G2$	Transfer function: change in control action to change in rotor speed
H	Turbine height
h	Channel depth
I	Current
I_U	Turbulence intensity
J_e	Emulator rotational moment of inertia
J_t	Turbine rotational moment of inertia
J_{eq}	Equivalent rotational moment of inertia
J_{pto}	PTO rotational moment of inertia
K	Nonlinear controller gain
K_ω	Linearizion coefficient: rotor speed
K_I	Integral gain
K_P	Proportional gain
K_U	Linearizion coefficient: flow speed
K_V	Generator voltage constant
L	Turbulent or characteristic length scale
m	Mass
N	Number of blades
n	Time of controller action
N_b	Gearbox ratio
N_v	Virtual gearbox ratio
p	Number of magnetic poles
P_e	Electrical power

P_k	Kinetic power
P_m	Mechanical power
P_t	Turbine power
P_{em}	Emulator power
P_{PTO}	Total expected PTO power
R	Load resistance
r	Turbine radius
t	Blade thickness
U_∞	Free-stream velocity
V	Voltage
X	Blockage ratio
z	Depth below surface
ADV	Acoustic Doppler velocimeter
AFT	Axial-flow turbine
CFT	Cross-flow turbine
Conn	MaREI-Beaufort EEM
DFIG	Doubly-fed induction generator
DTC	Direct torque control
EEM	Electromechanical emulation machine
FFT	Fast Fourier transform
Fr	Froude number
IG	Induction generator
LPV	Linear parameter varying
MPP	Maximum power point

MPPT	Maximum power point tracking
MRE	Marine renewable energy
MTP	Maximum torque point
PI	Proportional plus integral
PLC	Programmable logic controller
PMSG	Permanent magnet synchronous generator
PTO	Power take-off
PWM	Pulse-width modulation
Re	Reynolds number
SCIM	Squirrel cage induction motor
SSMTB	Secure Scalable Microgrid Testbed (Sandia EEM)
TKE	Turbulent kinetic energy

ACKNOWLEDGMENTS

I foremost acknowledge my parents, Doreen and Bob, siblings, Steph and Dan, and grandmothers, Teresa and Connie for unwavering support throughout the years and accepting me for the eccentric, city-hopping person that I am. Thanks also to my grandfathers, Dick and John, who were incredible role models but who sadly are no longer with me. Many thanks to the friends who have helped me through the times when I wasn't sure if I was on the right track, notably Alex Malkin and Julia Morley.

My advisor and committee chair for the entirety of my graduate school experience, Brian Polagye, has provided everything I could possibly imagine in the role. His work ethic, scientific acumen, and dedication to students and teaching have been inspirational and formed me into the researcher I am today. I knew I made the right choice in attending UW when Brian informed me of my funding offer over a beer. When I started the program, he asked me what I wanted to work on and proceeded to allow me to pursue a stalling (pun intended) project with little available funding. It has since been an incredible journey. I hope to maintain our professional partnership and grow into better friends now that he's accepted my 'friend' request on Facebook. Thanks also to my supervisory committee, consisting of Professor Brian Fabien, Professor Daniel Kirschen, and Professor Howard Chizeck acting as GSR for their interest in my work and sound advisement. Additional thanks to Dr. Andy Stewart for granting me the opportunity to work on further MHK development projects.

A sizable portion of the work herein was conducted on a US Department of Energy EERE 'Postdoctoral' Research Fellowship spent in Cork, Ireland at MaREI-Beaufort. Much gratitude is due to Ray Alcorn for allowing me to pursue my own research agenda and Judy Rea for being a fantastic mentor, collaborator, and friend.

Special thanks are due to James Joslin, Alicia Clark, Andy Lewis, and Nick Stelzenmuller, who all ended up in the same place at the same time as me. We were acquainted through chance but became friends through many shared interests and experiences. Extra credit to James, Andy, and Nick for rekindling my interest in climbing and getting me back into the great outdoors. Thanks also to Andy, Trevor Harrison, Brad Perfect, and Adam Brown for helping me get down that mountain that one time.

The Marine Renewable Energy Lab has been a fantastic place to learn and work, primarily because of the stellar minds it consists of. Thanks to Chris Bassett, James, Trevor, Hannah Ross, Ben Strom, Dom Forbush, Paul Murphy, Emma Dewitt-Cotter, Kaylie McTiernan, and Curty Rusch for many productive hours of conversation and collaboration. Thanks also to Michelle Hickner and Bill Kuykendall for wonderful lab support, and Danny Sale for advice on all things computing.

Funding for my work has come from a variety of sources, including Dr. Roy Martin who provided a fellowship supporting the first two years of my work. I am deeply grateful for his dedication to education and research in the marine sector. Additional support has come from the University of Washington Royalty Research Fund, the US Department of Energy, Ocean Renewable Power Company, and Naval Facilities Engineering Command.

DEDICATION

To my nieces, Olivia and Giulia, for whom I work to provide a better, more sustainable world.

Chapter 1

INTRODUCTION & BACKGROUND

The developing state of the industry of marine renewable energy (MRE), specifically tidal, ocean, or stream-based hydrokinetic conversion, allows for innovation in the design and implementation of devices, as a single technology has not been converged on. Unlike the wind energy industry, in which three-bladed, horizontal-axis axial-flow turbines (AFTs) with variable pitch dominate the market and landscape, near-commercial hydrokinetic turbines offer a wider variety of designs. Additionally, government and academic research labs are actively involved in device development and are revisiting turbine concepts previously abandoned for large-scale commercial applications by the wind energy industry, such as cross-flow turbines (CFTs). CFTs are a specific class of turbine, in which the primary axis of rotation is orthogonal to the direction of flow (Figure 1.1). Utilizing blades in a circular pattern around this axis and positioned vertically relative to the seabed, this style of turbine rotates in a single direction regardless of the orientation of the incoming flow; no active or passive yawing mechanism is required. Active avenues of research on cross-flow turbines for wind farming applications include densely-packed arrays of counter-rotating devices for increased energy capture, offshore turbines with capacities greater than 10 MW, and community-scale or isolated installations [24, 76, 10].

Though not universal, blade pitching is common on many AFTs developed for both wind and hydrokinetic applications and is utilized to adjust the operating point of the turbine by changing the aerodynamic or hydrodynamic properties of the blades. This mechanism offers a means of regulating the speed of a turbine. Most designs of cross-flow turbines are fixed-pitch during operation with an optimized preset pitch angle [10]. The properties of cross-flow turbines with fixed pitch angles narrow the degrees of freedom of the system to one: angular

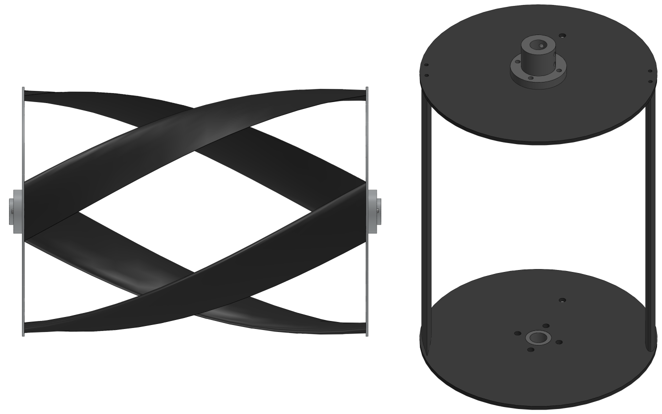

Figure 1.1: Example cross-flow hydrokinetic turbines.

motion around the turbine axis. The system represents the minimal complexity for the purposes of dynamic modeling and control of a rotating turbine, but results in deceptively complicated hydrodynamics.

An additional potential benefit of cross-flow turbines over alternative topologies is the ability to tightly pack them into dense arrays [70]. The performance improvement from the resulting high blockage may make arrays of CFTs economically advantageous relative to AFTs. Many tidal channels and rivers posses a roughly rectangular cross-section, which are well-suited to the form factor of CFTs.

CFTs do suffer from several disadvantages relative to AFTs to the extent that research into their design and performance for wind energy considerably slowed after initial interest in the 1970s and 1980s, possibly due to a lack of early investment in the technology [62]. Furthermore, analysis of the aerodynamics or hydrodynamics of a cross-flow system is more challenging because downstream blades interact with the wake of upstream blades and the angle of attack varies continuously through rotation, giving rise to unsteady aerodynamic effects (e.g., dynamic stall) [62]. The oscillatory forces on the central axis necessitate robust construction and limit the size of turbines. However, the nature of the marine environment may negate this concern, as the size of hydrokinetic turbines relative to their wind analogues are smaller for similar power output due to increased working fluid density (850x increase). Therefore, continued research and development of cross-flow turbine technology is warranted.

Early-stage testing and evaluation of hydrokinetic turbines often involves characterizing only the hydrodynamic (mechanical) performance of the rotor. Even so, prototype testing at reduced geometric scale may yield results that do not correlate well to the full intended scale of a device. Additionally, considerations for conversion to and transmission of electrical power are typically postponed until prototypes are of a scale suitable for field deployment and testing. Control strategies to regulate power output may not be implemented until the final phases of development or after commissioning a device. This dissertation demonstrates how understanding turbine rotor and system component dynamics enables more effective performance evaluation, integration, and control strategies. The ability to effectively carry out these tasks at small scale or in a laboratory enables simpler prototype development, and ultimately a lower cost of energy for the technology. The work explores the dynamics and scaling of cross-flow hydrokinetic turbines in subsequent sections of this chapter, demonstrates a key result of dynamic analysis by experimentally exploring the stability of a turbine in Chapter 2, develops testing methods for full system characterization in Chapter 3, evaluates the effectiveness of dynamic emulation of a characterized turbine in Chapter 4, and presents results of emulation of a field-deployed commercial turbine in Chapter 5. Conclusions are summarized in Chapter 6. The majority of the work in this document has been published, either in peer-reviewed literature or in conference proceedings. This includes two journal articles (Chapters 3 & 4) and a conference paper (Chapter 5). Chapter 2 is in preparation for submission as a journal article as of the time of the publication of this dissertation. Appendices to the document include early work leading to a conference paper on an adaptive control strategy, presentation of a method for estimating performance uncertainty, and a direct comparison of turbine efficiency of two similar turbines of different geometric scale.

1.1 Cross Flow Turbine Dynamics

Turbines typically exhibit peak performance at a unique non-dimensional rotation rate (normalized by the free-stream velocity incident on the turbine) or tip speed ratio (λ) defined as,

$$\lambda = \frac{\omega_t r}{U_\infty}, \tag{1.1}$$

where U_∞ is the free-stream velocity in m/s, r is the radius of the turbine in m, and ω_t is the turbine's rotation rate in rad/s. A performance curve can be created for a turbine, parameterizing its mechanical efficiency (C_P),

$$C_P = \frac{\tau_h \omega_t}{\frac{1}{2}\rho A {U_\infty}^3} \tag{1.2}$$

in which τ_h is hydrodynamic torque developed by the rotor blades, ρ is the density of water, and A is the turbine's projected area, as a function of λ. A cross-flow turbine typically has a single performance curve, produced by measuring rotation rate, torque and free-stream velocity. The curve is a distillation of the system's complex hydrodynamics into a single-parameter space. Such a curve is a convenient idealization of steady-state turbine performance, but it is often subject to considerable experimental uncertainty (Appendix B). Furthermore, it has been shown in previous experimentation that small-scale turbines operating over a range of inflow speeds exhibit variable performance due to variations in blade lift and drag with Reynolds number [57, 4]. It follows that, to reliably describe the hydrodynamic performance of a turbine, a carefully constructed curve or family of curves and knowledge of the uncertainty associated with them is of primary concern.

Knowledge of mechanical efficiency in the form of $C_P(\lambda)$ does not imply knowledge of the total system or water-to-wire efficiency due to the presence of power take-off (PTO) components required to condition and convert mechanical power to electrical power. These components can critically affect the dynamics and performance of hydrokinetic systems [2]. Therefore, prototype tests including a PTO (e.g., gearbox, generator, electrical load) are necessary to quantify overall system performance. Total system efficiency (η_s) is defined as the fraction of kinetic power passing through the rotor projected area, (P_k)

$$P_k = \frac{1}{2}\rho A {U_\infty}^3 \tag{1.3}$$

converted to electrical power (P_e),

$$\eta_s = \frac{P_e}{P_k}. \tag{1.4}$$

A turbine's dynamics can be modeled to the first order utilizing a well-characterized performance curve and a form of the general dynamic equation of a rotating body,

$$\ddot{\theta} = \dot{\omega}_t \tag{1.5}$$

$$\dot{\omega}_t = \frac{\tau_h - B_{eq}\omega_t - \tau_c}{J_{eq}} \tag{1.6}$$

where θ is the turbine's angular position, B_{eq} is an effective damping coefficient, J_{eq} is the moment of inertia of the turbine and coupled rotating components, and τ_c is control torque resisting rotation as a result of PTO loading [11]. The formulation of (1.6) does not account for PTO stiffness or the effects of added mass, which may be significant if angular acceleration is high and variable. Similar to its non-dimensional power, τ_h can be represented in characteristic form as,

$$C_Q = \frac{\tau_h}{\frac{1}{2}\rho A r U_\infty^2}, \tag{1.7}$$

its torque coefficient. Hydrodynamic torque then becomes

$$\tau_h = \frac{1}{2} C_q(\lambda) \rho A r {U_\infty}^2, \tag{1.8}$$

a nonlinear function of λ with quadratic dependence on U_∞. Typical C_P and C_Q curves for an arbitrary cross-flow geometry are shown in Figure 1.2 [7]. For the purpose of incorporation into the turbine dynamic equation, $C_Q(\lambda)$ can be represented by a polynomial. For example, as a cubic function, it becomes

$$C_Q(\lambda) = a\lambda^3 + b\lambda^2 + c\lambda + d \tag{1.9}$$

where a, b, c, and d are empirical coefficients. The curve describes stable operating states that the turbine, on average, converges to.

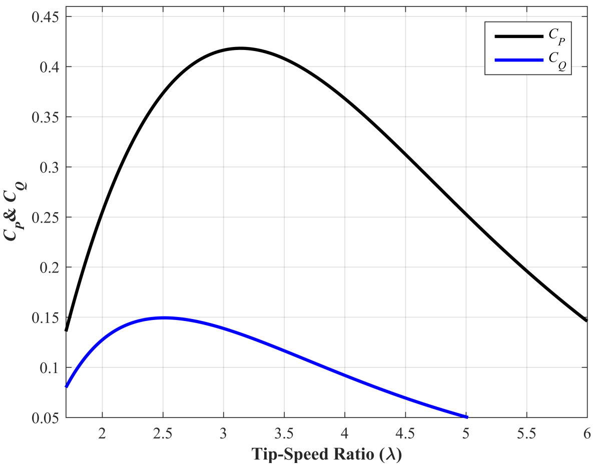

Figure 1.2: Arbitrary turbine performance and torque curves.

1.2 Means and Objectives of Turbine Control

1.2.1 Basic Means of Control of a Cross-Flow Turbine

Fixed-pitch CFTs can be regulated by controlling the only available degree of freedom - adjusting resistance or assistance to rotation, τ_c, leading to a change in rotation rate. This torque can be imposed mechanically or through a generator and PTO apparatus. In the latter case, this translates to regulating the electromagnetic torque of the generator it is coupled to. Utilizing system feedback of shaft torque or rotation rate, closed-loop speed or torque control can be accomplished by varying generator current. The relationship between mechanical power input and electrical power output is largely governed by the type of generator coupled to the system and the nature of its electrical load.

Two main classes of generators suitable for hydrokinetic turbine applications are permanent magnet synchronous generators (PMSG) and induction generators (IG). Differences in the construction of these electrical machines dictate the methods in which speed and power output of the generator are regulated. For a PMSG, magnetization of the machine is provided by the permanent magnets of the rotor. The rotor will contain a number of magnetic poles (p) and the frequency (f_{AC}) of the AC power it produces will depend on this number and the generator's rotation rate so that,

$$f_{AC} = \frac{\omega_g \pi p}{3600}. \tag{1.10}$$

where ω_g is the speed of the generator in rad/s. Control is conducted by setting a current on the PMSG's stator. This current is proportional to the electromagnetic torque of the generator. Control can be closed-loop in either speed or current depending on available feedback, but both methods ultimately set stator current. Lacking an internal source of magnetization, an IG requires setting a magnetizing or quadrature-axis current on the stator to induce a magnetic field in the metallic rotor. The synchronous speed (ω_s) of the generator is proportional to p and the frequency of the AC power produced,

$$\omega_s = \frac{3600 f_{AC}}{\pi p}. \tag{1.11}$$

Induction machines without rotor voltage injection can only generate electricity when their rotation rate is super-synchronous. Thus, the generator can be manipulated to produce power at any speed by modifying the voltage and f_{AC} of its output. Similar to a PMSG, electromagnetic torque is controlled by setting current on the stator, but offset in phase from the supplied magnetizing current, denoted the direct-axis current. A doubly-fed induction generator (DFIG) in which a slip ring grants access to windings of the rotor, common in the wind energy industry, may also be considered a viable generator choice [8].

Industry-standard electrical machines of a given rated power are typically intended for high-speed, low torque applications. This contrasts with the operation of many existing hydrokinetic turbine designs which tend to operate and be optimized for low speed to maintain high mechanical conversion efficiency and reduce the risk of cavitation and adverse environmental interactions. Therefore, shaft torque must be proportionally higher for a given rated power and low rotation rate. Gearboxes can be used to increase the shaft speed and decrease torque at the generator, but have high operating and maintenance costs. Custom generating solutions with high pole counts directly coupled to the rotor are employed in several turbine system designs, but may be large and more expensive than traditional electrical machines [33, 8].

1.2.2 Control Objectives

Major control objectives for a cross-flow hydrokinetic turbine are generally similar to those defined for wind energy. However, the nature of the hydrokinetic resource exhibits differences from wind and warrants modification to these objectives. For example, the forecasts of tidal currents, while not perfect, are far more accurate than those of wind [64]. Three broad objectives for turbine control are defined by [11]: the regulation of energy capture, mitigation of loads, and conditioning of power to meet quality standards. The scope of this work examines the first objective and briefly touches on the second. Objectives for energy capture for variable speed turbines can be further refined for a number of operating regimes based on the intensity of the resource (Figure 1.3): Region 1 is defined as periods when the turbine encounters low speed ($U_\infty < U_{cut-in}$), Region 2 encompasses periods when the resource is fast enough for operation, but below a rated speed ($U_{cut-in} < U_\infty < U_{rated}$), Region 3 is entered when the resource is at or above rated speed but below a maximum speed ($U_{rated} \leq U_\infty < U_{cut-out}$), while Region 4 includes all time spent at or above maximum speed ($U_\infty \geq U_{cut-out}$). With a turbine unable to rotate at low speed, there is no control objective for region 1. In Regions 2 and 3, the objectives become maximizing energy capture limiting energy capture to safe (rated) levels, respectively [38]. In Region 4, the objective is survival at high speed. Region 4 may not be present for all current turbines: tidal and ocean current devices are likely to be designed for known peaks and will not have substantial excursions beyond these points. Torque or direct speed control is used to regulate the speed of a turbine to maintain operation at its optimal λ in Region 2. Torque control may also be used to limit power in Region 3, where the options of increasing or decreasing ω_t are available.

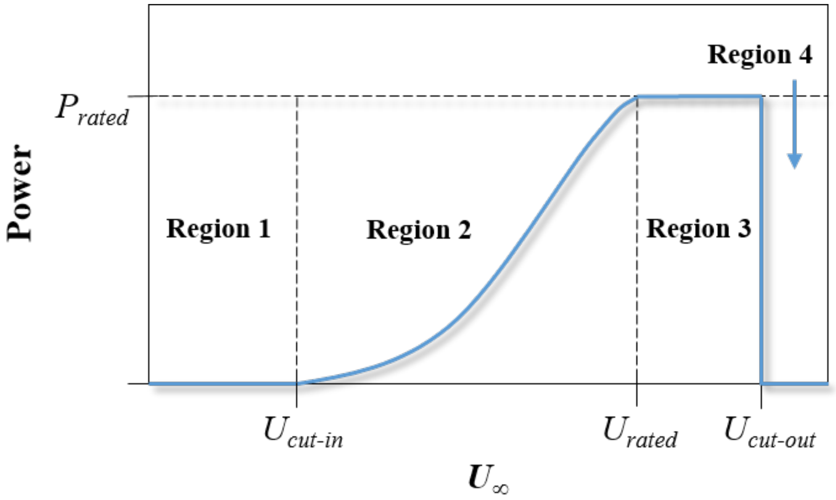

Figure 1.3: Standard operating regimes for a turbine.

1.2.3 Common Controller Architectures

An active area of research for both wind and hydrokinetic systems, the current state of the art in controllers for turbines includes formulations loosely conforming to four broad categories: feedback, feedforward, preview, and model predictive control. The first two categories are described herein, though the third & fourth show much promise for regulating large utility-scale wind turbines [44, 72].

1.2.3.1 Feedback Controllers

Long the workhorses of industrial systems, linear feedback controllers utilize sensor measurements of the state of a system which are compared to predefined set-points. Controller action is taken through some form of actuation to align the system with the desired state (error control). For a fixed-pitch hydrokinetic turbine, an obvious choice for a state to set and track is ω_t. A controller may be formulated to regulate rotation rate directly or normalized in the form of λ. Controller actuation is conducted by setting a value for τ_c. For example,

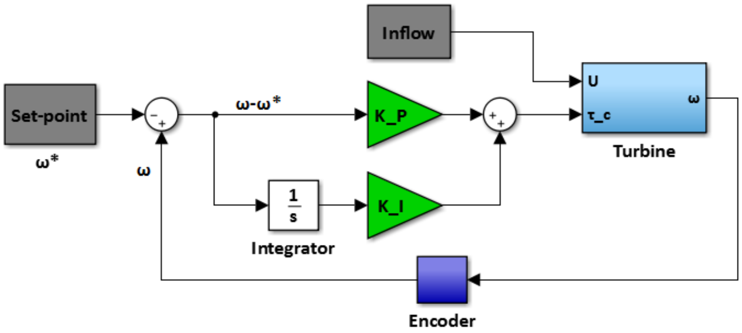

Figure 1.4: PI-ω_t controller schematic.

consider a Proportional plus Integral (PI) controller implemented with the goal of maintaining turbine operation at a rotation rate set-point (${\omega_t}^*$). τ_c is the sum of a proportional gain (K_P) on speed error and an integral gain (K_I) on the integral of speed error over the total time of controller action (n),

$$\tau_c = K_P(\omega_t - {\omega_t}^*) + K_I \int_0^n (\omega_t - {\omega_t}^*) d\tau \tag{1.12}$$

where τ is time in the continuous formulation of the controller or the length of a numerical time step in a discrete system. Gains are tuned to achieve desired performance characteristics such as under/overshoot percentage, rise time, and steady-state error. The performance of this controller is therefore dependent on the selected gains, as well as update rate and quality of the measurement of ω_t. The controller is shown schematically in Figure 1.4.

Similar to PI-ω_t control, PI-λ attempts to maintain a desired tip-speed ratio (λ^*). Control torque becomes,

$$\tau_c = K_P(\lambda - \lambda^*) + K_I \int_0^n (\lambda - \lambda^*) d\tau. \tag{1.13}$$

In addition to ω_t, PI-λ requires an estimate of U_∞ and its performance depends on the quality of this measurement. However, this controller is capable of tracking the instantaneous

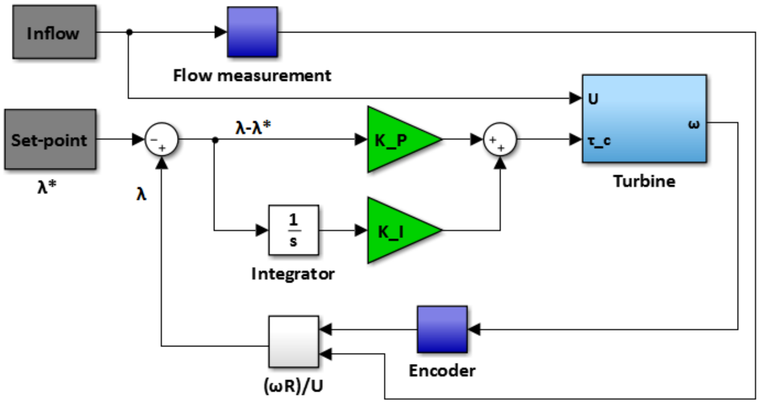

Figure 1.5: PI-λ controller schematic.

maximum power point as defined by a turbine's performance curve. This controller is shown schematically in Figure 1.5.

1.2.3.2 Feedforwrd Controllers

Feedforward controllers rely on system models to determine controller action, with or without additional knowledge of the plant's state. Derived from the dynamic model of turbine operation, the nonlinear feedforward $K\omega^2$ controller commands a torque,

$$\tau_c = K{\omega_t}^2 = \frac{1}{2}\rho A r^3 \frac{\eta(\lambda)}{\lambda^3}{\omega_t}^2 \tag{1.14}$$

which brings the turbine to a desired operating point on its performance curve [38]. In the case where K results in the turbine operating at peak efficiency, this optimal gain is referred to in (1.14) as K^*. K values larger or smaller in magnitude than K^* result in operation to the "left" or "right" of the peak (slower or faster than optimal λ, respectively). Optimal performance requires a well-defined performance curve and accurate measurement of ω_t. Note that unlike a feedback controller, the control torque equation does not explicitly prescribe a fixed set-point. Rather it controls the turbine to a set-point based on the estimate for the plant dynamics. This controller is shown schematically in Figure 1.6. An adaptive version

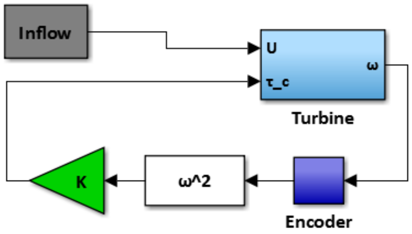

Figure 1.6: $K{\omega_t}^2$ controller schematic.

of $K{\omega_t}^2$ control can be used when a turbine's performance curve is subject to parameter variation (e.g., efficiency is a function of both λ and U_∞). A model of this variation with U_∞ is employed so that

$$\tau_c = K(U_\infty){\omega_t}^2 = \frac{1}{2}\rho A r^3 \frac{\eta(U_\infty, \lambda)}{\lambda^3}{\omega_t}^2 \tag{1.15}$$

in which controller action depends on measurement of U_∞. As variation in free stream velocity is considered an uncontrollable disturbance to a system, utilizing this measurement does constitute a use of 'preview' information, however in a loose sense. As with the standard formulation for this controller, its performance depends on the quality of turbine performance characterization but also the quality of the flow speed measurement. The controller is shown schematically in Figure 1.7. An example of this controller in use is presented in Appendix A.

1.3 *Linearization and System Response*

Linear analysis techniques are widely used to gain insight into the functioning and inform the control of dynamic systems. Therefore, it is desirable to linearize turbine dynamics to better understand the nature of the system. Linearizion is conducted at an operating point and is assumed accurate within small excursions from this point. A CFT's operating point (ϕ) is defined by a stationary velocity and rotation rate pair,

$$\phi = [\bar{U}_\infty, \bar{\omega}_t] \tag{1.16}$$

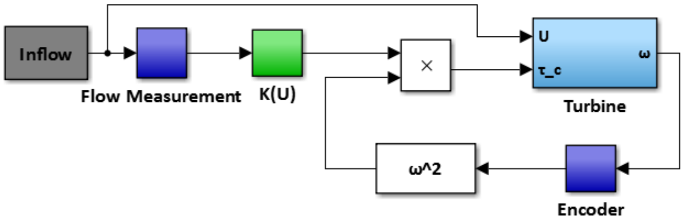

Figure 1.7: Adaptive $K{\omega_t}^2$ controller schematic.

in which the overbar represents a stationary temporal average, and fully defines a steady state. Deviation of measured velocity from the mean is a turbulent perturbation velocity,

$$\hat{U}_\infty = U_\infty - \bar{U}_\infty \tag{1.17}$$

The nonlinearity in (1.8) as a result of (1.9) can be treated by linearizing (1.8) around a value of ϕ, resulting in an expression for fluctuations of τ_h as a result of fluctuations in U_∞ and ω_t,

$$\hat{\tau}_h = K_\omega \hat{\omega}_t + K_U \hat{U}_\infty \tag{1.18}$$

where K_ω and K_U are derivatives of the expression for τ_h, the result of a first-order Taylor Series expansion about ϕ [30]. These derivatives,

$$K_\omega = \left.\frac{\partial \tau_h}{\partial \omega_t}\right|_\phi \tag{1.19}$$

$$K_U = \left.\frac{\partial \tau_h}{\partial U_\infty}\right|_\phi \tag{1.20}$$

take constant values when evaluated at ϕ such that,

$$K_\omega = \frac{1}{2}\rho A \left(r^2 c \bar{U}_\infty + 2r^3 b \bar{\omega}_t + \frac{3r^4 a \bar{\omega}_t^2}{\bar{U}_\infty} \right) \tag{1.21}$$

$$K_U = \frac{1}{2}\rho A \left(2rd\bar{U}_\infty + r^2 c \bar{\omega}_t - \frac{r^4 a \bar{\omega}_t^3}{\bar{U}_\infty^2} \right) \tag{1.22}$$

from substitution into (1.8). The linearized version of (1.6) is then constructed as,

$$\dot{\hat{\omega}}_t = \frac{(K_\omega - B_{eq})\hat{\omega}_t}{J_{eq}} + \frac{K_U \hat{U}_\infty}{J_{eq}} - \frac{\hat{\tau}_c}{J_{eq}} \tag{1.23}$$

describing deviation in rotational acceleration relative to an operating point as a result of deviations in rotation rate and control torque, and turbulence. The linearized dynamic system of (1.23) can be represented as a state space model that varies with ϕ, a first-order linear parameter varying (LPV) system where,

$$\dot{\hat{\omega}}_t = A(\phi)\hat{\omega}_t + B_1(\phi)\hat{U}_\infty + B_2\hat{\tau}_c \tag{1.24}$$

$$\hat{\omega}_t = C\hat{\omega}_t + D\hat{\tau}_c \tag{1.25}$$

with coefficients,

$$A = \frac{K_\omega - B_{eq}}{J_{eq}} \tag{1.26}$$

$$B_1 = \frac{K_U}{J_{eq}} \tag{1.27}$$

$$B_2 = \frac{1}{J_{eq}} \tag{1.28}$$

$$C = 1 \tag{1.29}$$

$$D = 0 \tag{1.30}$$

and the single state and output variable, ω_t [30]. The open-loop response of the turbine can be evaluated using standard linear time invariant (LTI) system techniques at any static value of ϕ. The system can thus be treated as a linear combination of transfer functions - one relating fluctuations in rotation rate due to turbulence, and a second relating fluctuations in rotation rate due to variation in control torque,

$$\hat{\omega}_t = [G_1(s)\ G_2(s)][\hat{U}_\infty\ \hat{\tau}_c]^T \tag{1.31}$$

the combination of which yields the total perturbation of rotation rate [11]. $G_1(s)$ and $G_2(s)$ are obtained from the LPV system as,

$$G_1(s) = C(sI - A)^{-1}B_1 + D = \frac{K_U/J_{eq}}{s + (\frac{B_{eq} - K_\omega}{J_{eq}})} \tag{1.32}$$

$$G_2(s) = C(sI - A)^{-1}B_2 + D = \frac{1/J_{eq}}{s + (\frac{B_{eq} - K_\omega}{J_{eq}})} \tag{1.33}$$

both of which have an identical single pole. The linearized system is analogous to a low-pass filter, where the location of the pole determines the slope of the turbine's response roll-off. The transfer functions can be evaluated in the frequency domain to yield the open loop turbine response in terms of magnitude and phase shift. The magnitude of the transfer function indicates the gain by which the state variable (deviation in rotation rate) increases relative to the inputs (turbulence or control torque fluctuations). A physical intuition for the phase response can be gained by imagining inputs and outputs as purely sinusoidal; the phase shift is the amount by which the output response signal is shifted from the input when viewed in the time domain.

Transfer function G_1 can be evaluated for an arbitrary cross-flow geometry with a typical performance curve (1.2) to investigate the role of individual turbine parameters' contributions to its dynamic response to turbulence. A turbine's rotational moment of inertia, analogous to mass in linear motion, scales the effects of torque acting on the system; a higher inertia imparts better resistance to acceleration due to transient forcing, making the turbine less sensitive. Evaluating G_1 over a range of J_{eq} and frequencies of turbulence clearly shows this effect, as the turbine's response is diminished (lower roll-off frequency) as J_{eq} is increased (Figure 1.8). The system's damping, B_{eq}, represents losses in the system, enacting a torque proportional to ω_t in opposition to the hydrodynamic torque developed by the turbine. Increasing the magnitude of B_{eq} reduces the magnitude of the turbine's response over the entire frequency band, clearly exemplifying a damping effect (Figure 1.9). Thus, the coupling of J_{eq} and B_{eq} grossly define the bandwidth and magnitude of a cross-flow turbine's dynamic response. The ratio of the two can be considered the turbine's mechanical time constant, ζ,

$$\zeta = \frac{J_{eq}}{B_{eq}}. \tag{1.34}$$

Under equivalent turbulent velocity conditions, a system with a longer time constant (inertia-dominated) will be insensitive to smaller scales of turbulence, while a system with a shorter time constant (damping-dominated) will be more reactive to a wider range of turbulent frequencies, but with a diminished response. The same trend is apparent when evaluating transfer function G_2, encoding the turbine's response to changes in τ_c, the controllable input to the system. Thus, if controlling a turbine by adjusting τ_c to drive it to a desired setpoint, a system with a longer time constant will only respond to relatively low frequency adjustment, whereas a system with a shorter time constant is more controllable (faster response).

Dynamic stability under turbulent conditions can also be investigated utilizing transfer function G_1, evaluated at different realizations of ϕ. The global maximum of a turbine's characteristic curve, known as the maximum power point (MPP), and its maximum torque point (MTP) occurring, at a correspondingly lower value of λ, are obvious choices for consideration. The open-loop magnitude and phase response of G_1 are shown at three values of λ: at the MPP, at a higher value, and at the MTP (Figure 1.10). At λ corresponding to the MTP, we observe a phase shift approaching -180° at low frequencies, signifying antiphase response with positive gain (negative gain margin), indicating the system is closed-loop unstable based on Nyquist stability criteria [59]. This is consistent with observations of operating turbines experiencing hydrodynamic stall at values of λ at and lower than that of the MTP, while operating stably above this value. This is consistent with results from quasi-steady stability analysis discussed in detail in Chapter 2.

1.3.1 Relation to Turbulence in a Tidal Channel

Analysis of the flow in a tidal channel is conducted to determine if the turbulent frequencies a cross-flow turbine may be sensitive to would be present in the flow during operation using the linear analysis techniques of 1.1. The turbine is assumed to be rated at 50 kW in 2 m/s flow, consistent with the system studied in Chapter 4. A representative velocity time-series data collected at 32 Hz with a Nortek Vector Acoustic Doppler Velocimeter (ADV) moored 10 m above the seabed in 56 m deep water in Admiralty Inlet in Washington's Puget Sound is utilized for this analysis [80]. The time-series contains the periodic changes in velocity associated with the site's mixed semidiurnal tidal cycle over the span of a day (Figure 1.11).

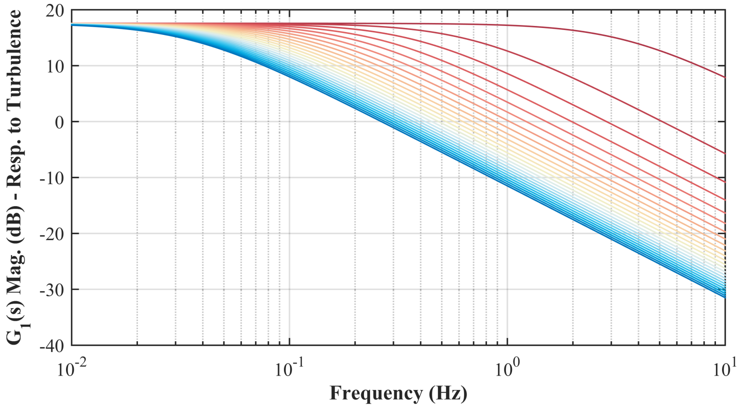

Figure 1.8: CFT magnitude response to turbulence with increasing inertia (red to blue).

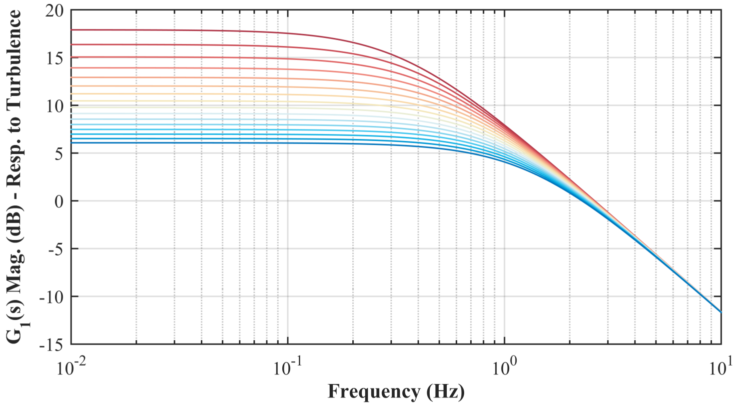

Figure 1.9: CFT magnitude response to turbulence with increasing damping (red to blue).

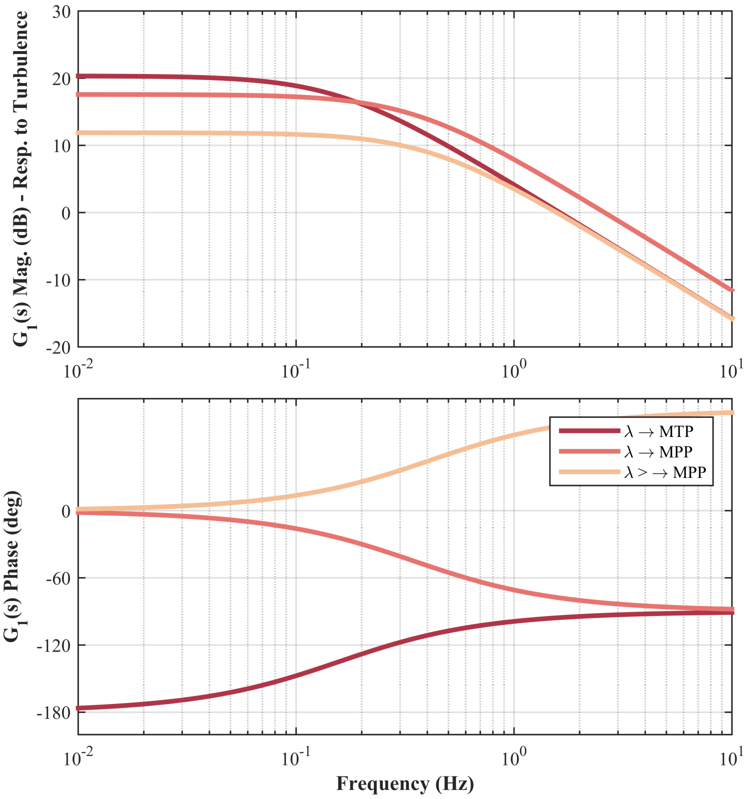

Figure 1.10: CFT magnitude and phase response to turbulence at different operating points.

A relatively stationary (in a mean sense) 10 minute portion of this data is selected near the turbine's rated flow speed during flood tide (mean horizontal velocity of 1.93 m/s). A linear trend is subtracted from the time-series to remove non-turbulent variation. The horizontal velocity is de-spiked to remove spurious points according to a 3-D phase-space algorithm [52]. The time-series is split into windows of 128 s with 50% overlap and processed with a Hamming filter prior to performing an FFT and merging the spectra to obtain a single turbulence spectrum [80]. The magnitude of the resulting spectrum represents the turbulent kinetic energy (TKE) present in the flow over the frequency band of interest. The spectrum of TKE at the Admiralty Inlet site (Figure 1.12) contains three distinct regimes: below 0.1 Hz, the lowest frequency, anisotropic turbulent structures contain the most energy, between 0.1 Hz and 2 Hz there is a classic isotropic eddy cascade, and above 2 Hz the turbulence spectra is masked by Doppler noise inherent to instrument operation [81]. Several aspects of the impact of turbulence on control can be observed by viewing the turbine's response to turbulence from transfer function G_1 and the turbulence spectrum together (Figure 1.13). The turbine is most capable of reacting to turbulence at frequencies with the most intense TKE. At the frequency of unity gain (0.67 Hz), the magnitude of TKE is reduced to 0.7% of its value at 0.01 Hz. In the inertial subrange, the turbine response decreases at nearly the same rate as the TKE. Correlating turbulence frequencies to length scales (L) with Taylor's frozen field assumption so that,

$$L = \frac{U_\infty}{f} \tag{1.35}$$

where f is the frequency of turbulence, indicates eddies between 3 m and 250 m in length are capable of inducing a greater than unity gain in rotation rate fluctuations [78]. These are length scales on the order of the physical dimensions of the turbine or greater. The turbine is significantly less sensitive to turbulence at smaller length scales (i.e., less than unity gain).

A use of understanding a turbine's response to turbulence is found when considering control; the technique can be used to determine the frequency of perturbations that are "worth" responding to, in terms of control effort translating to power production enhancement. For

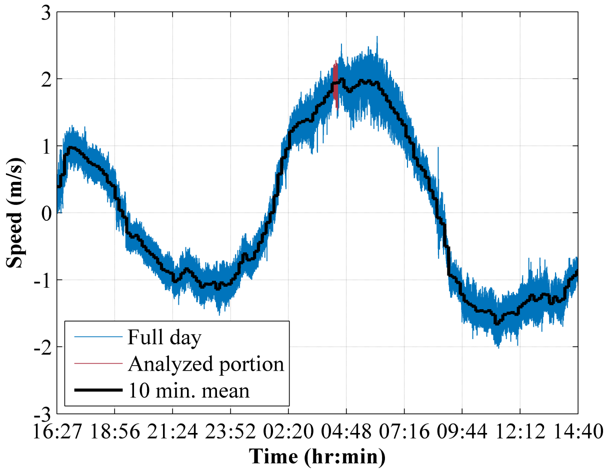

Figure 1.11: Horizontal velocity time series: Admiralty Inlet site [80].

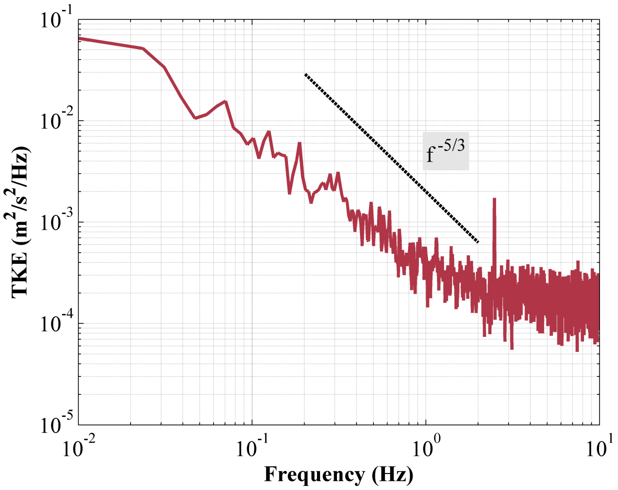

Figure 1.12: Horizontal TKE: 10 minutes with mean of 1.93 m/s, Admiralty Inlet site.

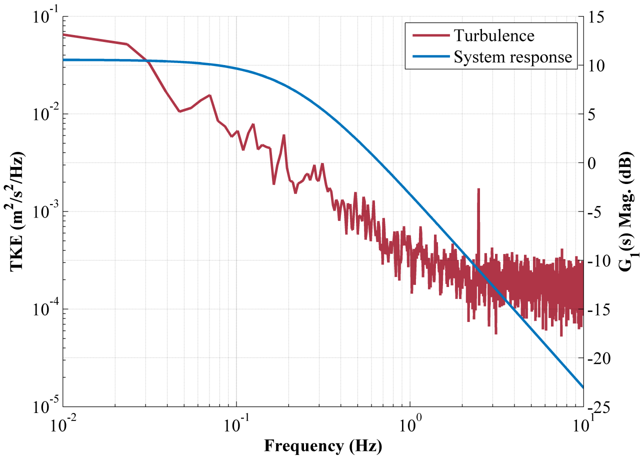

Figure 1.13: Turbulence spectrum and CFT magnitude response to turbulence.

a tidal environment, it is clear that due to the variation of the mean flow over times scales of hours, a control strategy should include adjustment to switch between operational regimes (Section 1.2.2), possibly achieved through the methods of gain scheduling. Additionally, a control strategy actuating to enact changes on the order of seconds to achieve an operational set-point may be desirable, as the water speed is highly variable on this time scale and the turbine is expected to be responsive. This suggests measuring the disturbance (turbulence) could be beneficial for control or load mitigation. Finally, adjustment to track turbulence at scales smaller than a turbine's physical dimensions appears to be of little benefit, as its ability to respond at this rate is low and the amount of energy available at these frequencies is also low.

1.4 Prototype and Resource Scaling for Cross-Flow Turbines

Hydrodynamic systems are typically prototyped at a geometrically smaller scale than intended for final use. Prototypes are used to test the feasibility of a design more rapidly and at lower cost than iterating a full-scale system. Therefore, prototype cross-flow turbines would ideally operate in a manner similar to their full-scale counterparts. Several options are available to attempt to align the characteristics of a small prototype and laboratory experimental conditions with a larger device and field experimental conditions. Each scaling method aims to match the physical, dynamic, or hydrodynamic properties of a turbine and the incident resource tested across scales, but none account for all three; indeed, an 'ideal' scaling method is not apparent and one should be selected based on the goals of the prototyping.

1.4.1 Geometric Scaling

Possibly the most obvious scaling technique is replicating the geometry of a full-scale turbine at a proportionally smaller size utilizing similar materials. However, this does not ensure the prototype turbine will exhibit the same dynamic properties as one of larger scale. For example, consider the case where all dimensions of a full-scale cross-flow turbine's geometry are scaled by a factor of κ, where $\{\kappa \in \mathbb{R} \mid 0 < \kappa < 1\}$. The primary constituents of a turbine's moment of inertia about its axis of rotation (J_{scaled}) are its radius and the mass of its blades (m). J_{scaled} is proportional to mr^2. Assuming constant density, blades scaled by κ will have mass proportional to κ^3 at a radius proportional to κ. Substituting into the form of J_{scaled},

$$J_{scaled} \propto \kappa^5, \tag{1.36}$$

a highly nonlinear scaling. Thus, a prototype built at 50% of full-scale would be expected to have a moment of inertia roughly 3% of full-scale and a correspondingly shorter time constant unless damping is similarly reduced.

1.4.2 Scaling for Geometric and Reynolds Similarity

The Reynolds number (Re) is a non-dimensional indicator of the strength of inertial forcing in a flow relative to viscous forcing. It is a quantity of considerable interest when analyzing the performance of lifting surfaces, such as hydrofoils. Re is proportional to a characteristic length scale which, for the purpose of turbine analysis, is chosen as the blade chord length

(c). Re_c is defined as,

$$\mathrm{Re}_c = \frac{U_\infty c}{\nu} \tag{1.37}$$

in which ν is the kinematic viscosity of the fluid. The choice of U_∞ as a velocity reference is not necessarily obvious for cross-flow systems as this neglects induction (a decrease in flow speed directly upstream of the turbine, discussed in Chapter 2), wake effects, and the apparent relative velocity of the fluid as a result of rotation. Lift and drag forces imparted by the fluid on hydrofoils comprising turbine blades are typically a function of Re_c at lower values up to a critical point where the ratio of lift to drag no longer exhibits this dependence [36]. Therefore, it would appear that, for a geometrically-scaled turbine using the same hydrofoil shape as a full-scale version, Re_c should be similar across scales to ensure appropriately proportional hydrodynamic forcing. However, scaling to maintain Re_c may not be realizable through conventional turbine testing techniques. For example, consider the case where all dimensions of a full-scale cross-flow turbine's geometry are again scaled by a factor of κ. Assuming the prototype and full-scale turbine are designed for operation in the same fluid (maintaining ν), Re_c can only be conserved by scaling the fluid velocity by a factor of κ^{-1} at prototype scale. This requires experimental facilities capable of producing or emulating flow speeds much higher than those observed in natural environments suitable for development of hydrokinetic extraction - a considerable challenge.

An additional peculiarity arises if an expression for the power expected from a geometrically and Re_c-scaled turbine is developed. Under these constraints, scaled U_∞ is proportional to κ^{-1} and all turbine lengths are proportional to κ, resulting in power-capture area proportional to κ^2. Since turbine power is proportional to U_∞^3 and A, this scaling method results in turbine power (P_{scaled}),

$$P_{scaled} \propto \kappa^{-1}. \tag{1.38}$$

As κ is by definition < 1, power output of the prototype is expected to be *greater than* that of the full-scale turbine by a factor of $1/\kappa$. However, this counterintuitive result may not have implications for the operation of a physical prototype due to the complications with achieving this type of similarity. Additionally, this result suggests the use of an alternative velocity reference in the definition of Re, such as relative velocity - a quantity dominated by the speed of the rotor, therefore allowing for higher values corresponding to faster turbine rotation. This would likely be achievable for a smaller-scale device. Comparison of the performance of geometrically similar turbine tested at different U_∞ is described in brief in Appendix C.

1.4.3 Scaling for Geometric and Open-Channel Flow Similarity

The Froude number (Fr), defined as

$$\mathrm{Fr} = \frac{U_\infty}{\sqrt{gh}} \tag{1.39}$$

in which g is gravitational acceleration and h is a relevant length such as channel depth, is a non-dimensional grouping comparing inertial forcing of a flow to gravitational forcing. In the context of open-channel flow, Fr is the ratio of flow speed to the phase speed of shallow-water surface waves and broadly defines the nature of energy in flow [53]. Coupled with geometric scaling of a turbine and channel, scaling to maintain Fr in model or prototype evaluations could be used to match the flow conditions expected at full-scale. As water must adhere to solid boundaries, the velocity distribution (a resource characteristic) in an open-channel such as a river or basin is not uniform [53]. Therefore, matching these characteristics across scales may improve agreement between scaled and designed turbine performance. Additionally, surface effects may influence the loading and wake structure of a device, though waves have been shown to have minimal effect on the average performance of a turbine [87, 47].

As length appears in the denominator of (1.39), scaling to maintain Fr results in lower velocity for prototype testing. Though convenient for conducting tests in experimental facilities, this feature ensures Re_c at prototype scale will be significantly smaller than field scale. As many experimental and computational studies of cross-flow turbines have demonstrated, performance is dependent on Re_c, particularly at lower values [74]. Hence, this method of scaling is unlikely to yield similar $C_P(\lambda)$ across scales.

1.4.4 Scaling for Time Constant Similarity

Experiments involving turbine dynamics, such as the emulation of a turbine on a hardware-in-the-loop testbed, may be scaled to maintain the system's mechanical time constant [56]. As described in Section 1.1, ζ expresses the nature of a turbine's dynamic response to turbulence and control. Scaling to maintain this value is accomplished by multiplying each term on the right hand side of (1.6) by a scale factor. By reducing the torques acting on the system and its inertia by the same degree, $\dot{\omega}_t$ is preserved across scales. This technique assumes $C_P(\lambda)$ is maintained through scaling, a condition that may be difficult to achieve with a physical prototype due to the factors outlined in Sections 1.4.2 and 1.4.3. If τ_h is scaled while $C_P(\lambda)$ and $\dot{\omega}_t$ are maintained, the implication is that the technique effectively reduces the power capture area of a cross-flow turbine by reducing its height in a vertical orientation or length in a horizontal orientation under the influence of the same magnitude flow velocity. This feature is convenient for evaluating the full dynamics of a turbine's response with a lower power output more easily achievable in a laboratory setting. For example, a motor can be programmed to be dynamically similar to a field-scale turbine under turbulent flow conditions but generate a fraction of the electrical power that would be expected in the field - a concept explored in detail in Chapters 4 and 5.

Chapter 2

SYSTEM STALL OF A CROSS-FLOW HYDROKINETIC TURBINE

The text of the following chapter is currently in preparation for publication. Portions of it appear as an extended abstract in Proceedings of the 4th Marine Technology Symposium.

2.1 Introduction

A dynamic model of cross-flow turbine stability resulting from linearization of the dynamic equation of motion (1.6) has been developed in Chapter 1. To summarize, the model indicates a turbine is unstable and thus susceptible to system stall (where the turbine ceases to rotate) while operating near the peak of its $C_Q(\lambda)$ curve or MTP, herein referred to as λ_c. Additionally, the ratio of a turbine's rotational moment of inertia to damping coefficient, the system time constant (ζ), broadly defines the systems bandwidth of response to turbulence. However, these results are purely mathematical deductions and offer no firm explanation as to why the MTP is a limit of stability or the exact nature of turbulent fluctuations leading to instability. Depending on the torque curve's shape and range of λ, its MTP may be in close proximity to its MPP - a zone where stable operation is desirable. Additionally, low-λ operation (underspeed control) aims to regulate power output of a turbine by shifting to λ slower than that at peak C_P [3]. This is advantageous for several reasons. Chief among them is typically lower thrust loading at lower λ. Second, shutdown or emergency stop procedures become safer: if operating at λ faster than that of the MPP, known as overspeed control, shutting down requires moving to a slower speed, through the state in which the turbine produces the most power. In underspeed mode, the turbine would shed load as it sheds speed. Thus, understanding the relationship between the MTP, a turbine's response to turbulence, and system stall is of considerable interest.

The relationship between (1.6) and (1.8) indicates a turbine operating at a steady ω_t will experience an increase in τ_h when subject to a sustained increase in U_∞ and a decrease in τ_h when subject to a decrease in U_∞ under constant τ_c. Step changes in U_∞ ultimately result in step changes in ω_t, with a final speed obtained when the turbine's hydrodynamic torque is again $\tau_h = B_{eq}\omega_t + \tau_c$. Given a known initial state $(\lambda_i, U_{\infty,i}, \tau_{h,i})$, it is possible to determine a final state $(\lambda_f, \tau_{h,f})$ that is the result of a change in U_∞ by solving (1.8) for λ. As complete system stall occurs following deceleration, changes in inflow speed considered herein are decreases, such that $U_{\infty,f} < U_{\infty,i}$.

A valid solution to (1.8) (real-valued, in range where C_Q is defined) exists for a decrease from $U_{\infty,i}$ under the following conditions: 1. the turbine is perturbed from λ_i faster than λ_c and 2. $U_{\infty,f}$ exceeds a certain threshold. Condition 1 exists because the turbine cannot decelerate to a state that produces higher torque when U_∞ decreases if it starts at $\lambda_i \leq \lambda_c$; the resistive torque command held at the initial state will always be higher than $\tau_{h,f}$, as λ_c corresponds to the global maximum of the $C_Q(\lambda)$ curve. For condition 2, the magnitude of drop in U_∞ a turbine perturbed from λ_i can withstand (i.e., settle at another stable rotation rate, $\omega_{t,f}$) increases as λ_i is increased; intuitively, the further to the right on the $C_Q(\lambda)$ curve the turbine begins at, the more stable final operating states are available to it. This conclusion depends on the properties of the function used to model the $C_Q(\lambda)$. However, they will be valid for any model that includes a global maximum of C_Q and no local extrema.

The maximum possible step decrease in U_∞ as a function of λ_i and $U_{\infty,i}$ was analytically evaluated for an arbitrary CFT geometry with known $C_Q(\lambda)$. For a given initial condition, the system is perturbed with a drop to $U_{\infty,f}$, and valid solutions to (1.8) that minimize the difference between $\tau_{h,f}$ and $B_{eq}\omega_{t,f} + \tau_c$ are identified. The minimum ratio of final to initial U_∞ an arbitrary turbine with a cubic-modeled characteristic curve is capable of withstanding before system stall is shown to depend on both initial λ and U_∞ (Figure 2.1); distance from λ_c and a lower $U_{\infty,i}$ are the most stable conditions the turbine can operate under. More stable operation at lower $U_{\infty,i}$ is a result of τ_h being more dependent on C_Q relative to U_∞

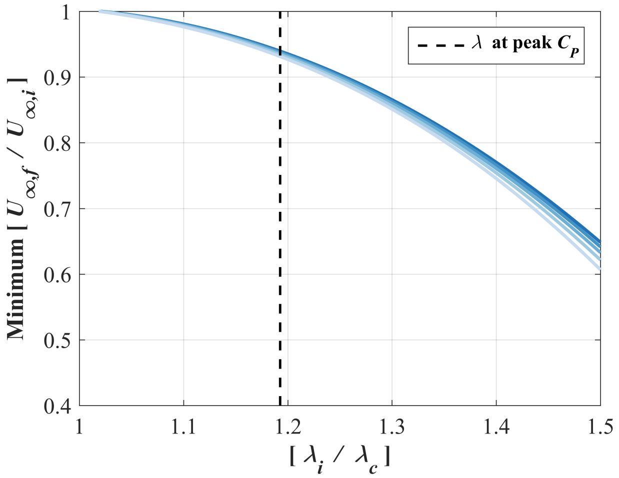

Figure 2.1: Critical ratio of final to initial speeds given λ_i. Darker lines indicate faster $U_{\infty,i}$, vertical line at peak C_P.

at lower speeds; achieving a stable $\tau_{h,f}$ is easier. However, while operating at peak C_P under constant torque control, the modeled turbine can only withstand a sustained drop in inflow speed to roughly 90% of its initial value before being susceptible to system stall.

The method does not consider the effects of turbulent inflow or finite turbine response due to inertia. Assuming performance is independent of Reynolds number, these factors would make the turbine more robust to system stall resulting from a decrease in inflow speed. Therefore, this analysis may be considered a conservative estimate of a turbine's stability and quasi-steady response to turbulent fluctuations.

Experiments characterizing the performance or evaluating control techniques of a laboratory-scale CFT have found that system stall occurs when rotating near λ_c (Appendix A). Here, a further suite of experiments was conducted to create a robust statistical model of the probability of system stall as λ approaches λ_c. Additionally, measurements of the turbine operating and environmental conditions during system stall were taken to determine if the event could be definitively correlated to changes in inflow. The statistical model of system stall is intended as a simple and practical description, as well as an acknowledgment that the process leading to it is stochastic in nature (i.e., it has been observed that system stall does not *always* occur immediately when reaching λ_c) with complex hydrodynamics resulting from dynamic stall [51]. A system stall model developed for an individual turbine may be used in numeric dynamic simulations to more realistically treat the probability of catastrophically stalling if λ_c is reached.

2.2 Methods

2.2.1 Laboratory-Scale Turbine & Experimental Setup

Experiments to quantify the operating and environmental conditions of a turbine undergoing system stall were conducted with a laboratory-scale helical cross-flow device. This turbine, shown in Figure 2.2, is a one-quarter geometrically-scaled prototype of the field-scale turbine evaluated in Chapter 3. However, it differs in that its blades were mounted with a preset pitch angle (β) of 6°at the blade mounting point (half-chord), a configuration a parametric study of similarly sized cross-flow turbines determined to produce higher performance [75]. Its parameters are described in Table 2.1. An estimate of its system time constant is 1.7 s. Performance of the turbine was evaluated in a recirculating flume with a cross-sectional area (A_f) of 0.76 m^2, with the rotor and in-water test apparatus (projected area of A_s) producing a blockage ratio (X)

$$X = \frac{(A + A_s)}{A_f} \tag{2.1}$$

of 6.7%. This level of blockage is low enough to not significantly affect turbine performance. The rotor was supported by a central shaft between rotary bearings, the upper of these flexibly coupled to a servomotor above the surface. Six-axis load cells measured reaction forces at the servomotor and lower bearing. The servomotor's *in situ* high-resolution optical encoder enabled precision closed-loop velocity control in addition to torque/current control. The rotor and experimental setup are shown in Figure 2.3.

$C_P(\lambda)$ was calculated as in (1.2) at nominal U_∞ of 1 m/s, utilizing average kinetic and mechanical power over 30 s runs under velocity control (setting ω_t), such that discrete values

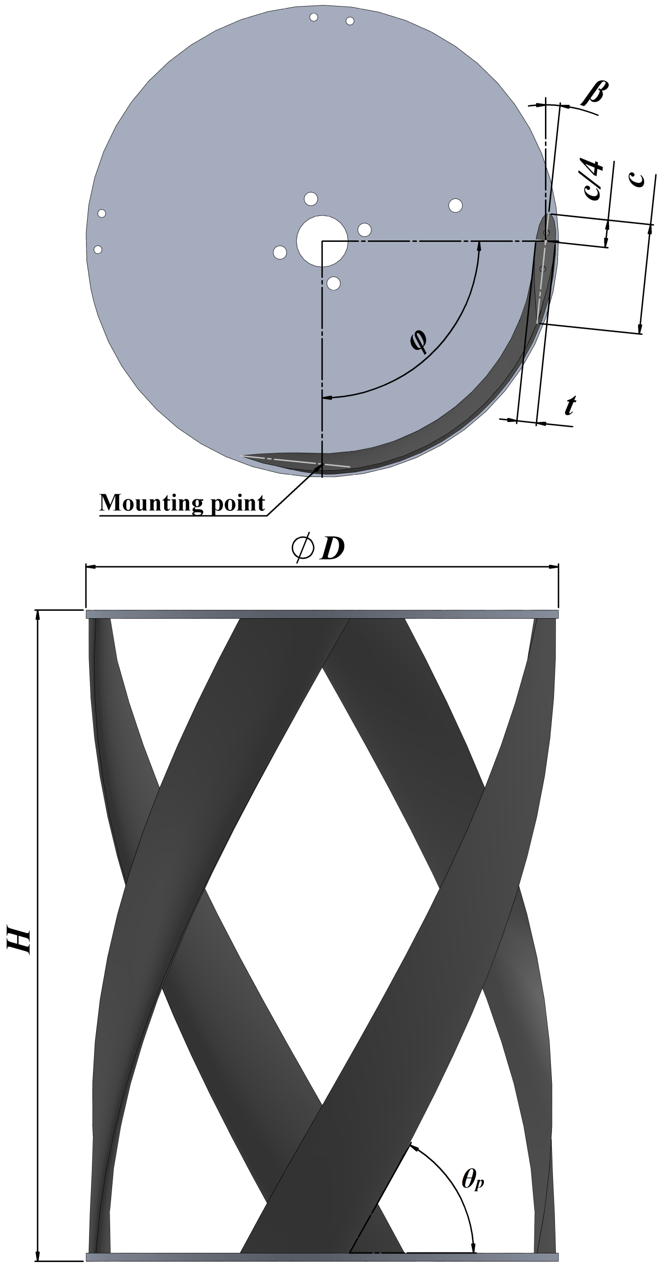

Figure 2.2: Laboratory-scale turbine schematic.

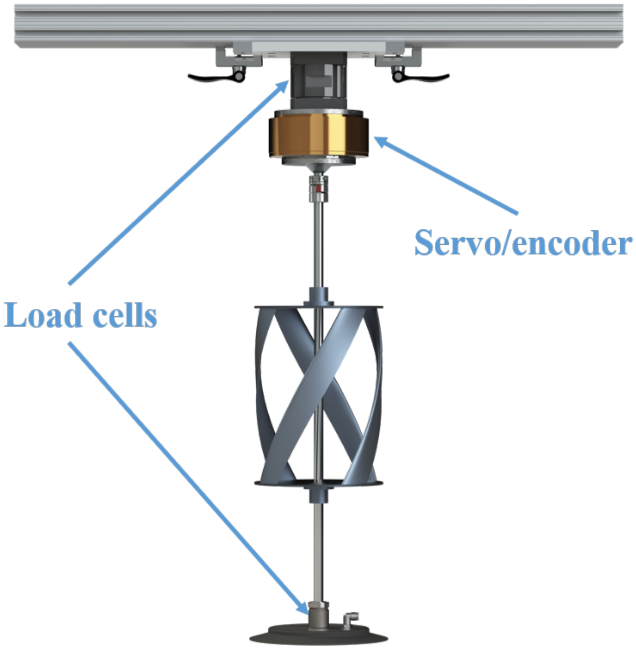

Figure 2.3: Laboratory-scale experimental setup.

of λ were maintained to produce a fuller curve including points lower than λ_c but where net power remained positive. Results of this characterization for both $C_P(\lambda)$ and $C_Q(\lambda)$ are shown in Figure 2.4. λ_c determined from characterization was 1.1.

2.2.1.1 Experimental Procedure

The following test procedure was conducted to systematically generate many realizations of system stall. The turbine was first allowed to accelerate to a freewheel state (highest λ achievable with no applied load) while the free-stream velocity was maintained at 1 m/s. Subsequently, the servomotor, acting as the turbine PTO, was commanded to enact a τ_c predetermined to decelerate the rotor to its critical speed, λ_c. This level of resistive torque was maintained until the turbine experienced complete stall or failed to stall within 60 s. The progression from operating at freewheel to reaching a rotation rate of 0 rad/s is referred

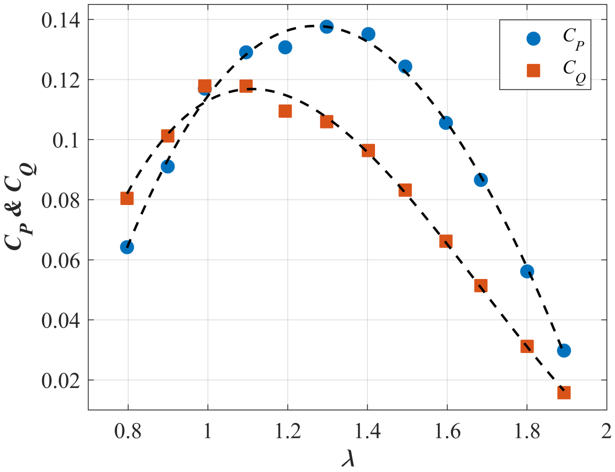

Figure 2.4: Characteristic performance and torque curves at 1 m/s.

to as a stall event. 288 stall events were carried out to create a robust dataset of conditions and a statistical distribution of time the turbine was able to maintain stable rotation before stalling. Turbine performance data were sampled at 1 kHz.

2.2.1.2 System Stall Identification

The experimental procedure for characterizing system stall was conducted systematically such that each iteration of 60 s consisted of the same sequence of events occurring in time. The homogeneity of the realizations and distinct modes of operation (i.e., bringing the turbine to λ_c, stable rotation, etc.) enabled the use of a cluster analysis method to objectively quantify the duration of stable operation at λ_c. The k-means method was selected for its ability to cluster the time series of turbine rotation rate. k-means partitions observations into a specified number of distinct groups such that points in each group are as similar as possible to each other and as dissimilar as possible to those in other groups [50]. Groupings were evaluated both quantitatively and qualitatively: a ‘silhouette’ value was computed, indicating distinctness of clusters and the identified groups were compared to physical modes

Table 2.1: Laboratory-scale turbine parameters.

Parameter	Value
Radius (D)	0.172 m
Height (H)	0.234 m
Moment of inertia (J_{eq})	0.005 kg m^2
Damping coefficient (B_{eq})	0.003 N m s/rad
Chord length (c)	0.04 m
Blade thickness (t)	0.0073 m
Preset pitch angle (β)	6°
Helical pitch angle (θ_p)	60°
Helical sweep angle (ϕ)	90°
Blade profile	NACA 0018
Number of blades	4

of the stall event [50]. Dimensionality of input to the algorithm was systematically evaluated to reduce complexity, with the number of available data series required to produce quality groupings reduced to two: turbine rotation rate and acceleration clustered into 5 groups. Measurements of U_∞, τ_c, and thrust force, though available, were not utilized in the selected realization.

2.2.1.3 Particle Image Velocimetry

Particle image velocimetry (PIV) utilizing a single-camera LaVision system was performed upstream of the turbine to measure and visualize inflow conditions over a broad spatial domain. A laser sheet was generated to illuminate naturally occurring particles at the plane

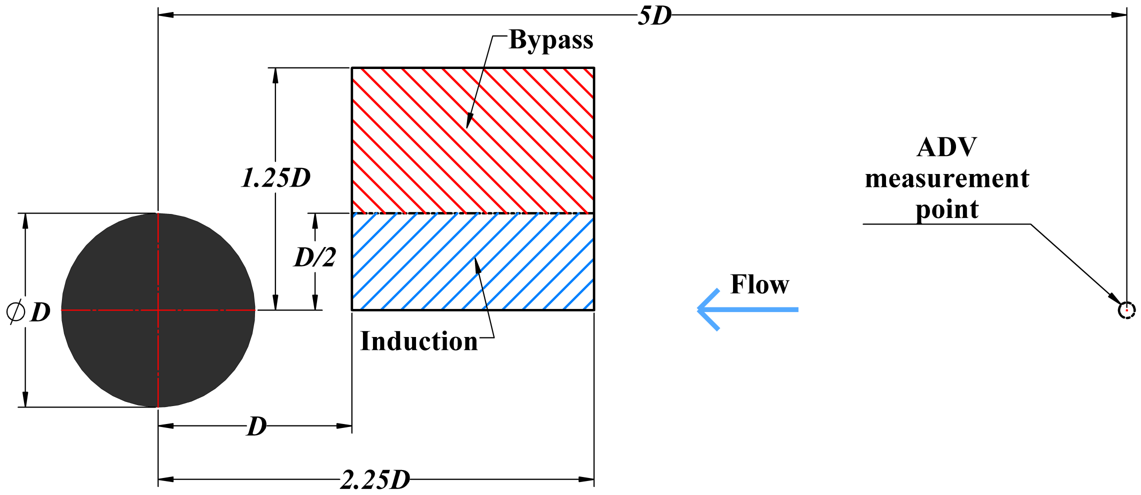

Figure 2.5: Flow measurement schematic with dimensions relative to turbine

of the turbine centerline for the camera, positioned to image a region 1D to 2.25D upstream of the rotor. This window bordered the turbine centerline and spanned to 1.25D in the cross-stream direction. The imaged region corresponded to inflow to the quadrant of the turbine in which blades begin their upstream (power stroke) pass and the region of flow bypassing the rotor to the side. The rotor was directly downstream of 40% of the interrogation window in the cross-stream direction. This region is referred to herein as the 'induction' zone, while the remaining portion of the window is referred to as the 'bypass' flow. A schematic detailing the position of the turbine (in plan view) and imaged region is shown in Figure 2.5. Time between exposure for image pairs (dt) was 1 ms and the camera captured pairs at a rate of 13 Hz. Four events for cases where the turbine did not immediately experience system stall were imaged.

Image pairs were preprocessed to remove background noise and even the intensity of visible particles. Velocity vectors were computed from image pairs in windows of $16x16$ pixels with 50% overlap at the finest resolution, resulting in velocity fields of $127x127$ vectors from the raw $1024x1024$ pixel images [77]. The resulting velocity fields were filtered for peak height, to maintain a high signal to noise ratio, and to remove outlying vectors.

2.2.1.4 Acoustic Doppler Velocimetry

The three components of inflow velocity were measured using analog output from an acoustic Doppler velocimeter (ADV, Nortek Vector) positioned 5D upstream of the rotor, as shown in Figure 2.5, with its sampling volume at the depth of the turbine centerline. Measurements from the ADV were used to correlate flow conditions with ω_t during stall events. Due to the instrument's position upstream of the turbine, Taylor's frozen field hypothesis was employed to account for advection time of turbulent structures downstream [78]. ADV measurements were de-spiked to remove spurious data [52]. Time series of inflow speed magnitude were smoothed with a moving-average filter with a window size of 500 samples (0.5 s) to reduce high-frequency noise. The correlation coefficient between normalized ω_t and U_∞ was calculated to gauge how well the turbine's rotation rate tracked changes in inflow conditions. Turbulence intensity, defined as

$$I_U = \frac{\sigma_U}{\bar{U_\infty}} \tag{2.2}$$

where σ_U is the standard deviation and $\bar{U_\infty}$ is the temporal mean of inflow speed, was also calculated. These quantities were compared between cases where system stall occurred 20 s - 40 s after test initiation and cases where the turbine did not stall after 60 s. For the latter cases, heavier moving-average smoothing was performed on U_∞ and the correlation coefficient recalculated to determine the time scales of turbulence the turbine was capable of responding to. It was hypothesized ω_t and U_∞ should be well-correlated, with a distinct observed decrease in U_∞ preceding system stall, as predicted by the quasi-steady analysis previously discussed. In addition, as the turbine system has been shown to behave similarly to a low-pass filter on flow (Chapter 1), correlation is expected to peak with a level of smoothing of U_∞ corresponding to the turbine's response plateau.

Turbulent kinetic energy (TKE) spectra were also computed as a means of evaluating and comparing flow conditions between stalling and non-stalling test realizations. For cases when system stall occurred between 20 s and 40 s after initialization, spectra were computed for the first 10 s and 10 s preceding an identified point at which the turbine had definitively stalled. These segments were further processed into two windows with 50% overlap and a Hamming filter was applied. The two resulting spectra were averaged. These spectra for each realization were subsequently averaged to yield individual spectra representing TKE for these segments of interest. Similar processing was used on 10 s segments of U_∞ measured during cases when the turbine did not experience system stall during 60 s of operation.

2.3 Results

2.3.1 Cluster Analysis of Stall Events

The k-means method was successful at identifying distinct regions of interest in time series of ω_t during system stall events. The effectiveness of the algorithm was enhanced by performing the clustering on data from all realizations of the experiment, as opposed to clustering individual events. An example of a typical time series of ω_t showing the five identified clusters is presented in Figure 2.6. These identify when the turbine is brought to λ_c, stable operation at λ_c, a convex region while the turbine is stalling, a concave region as ω_t reaches 0 rad/s, and after the turbine has fully stalled.

As shown in Figure 2.7, the turbine is most likely to stall after a short period of time, but capable of maintaining operation at λ_c for a wide range of time. The median time classified as ‘stable’ is 9 s. Average λ of this ‘stable’ region is 1.1, in precise agreement with the predicted λ_c determined from prior characterization. The probability of system stall after a given time is qualitatively similar to a Pareto distribution, with probability of stalling after longer periods decreasing according to a power law [50].

Rotor angular position was queried at the point identified by the k-means algorithm as the transition between ‘stable’ and ‘stalling.’ Although turbine position was not utilized as an input for clustering analysis, blade position at this point is consistent (noting the turbine’s four blades), as shown in Figure 2.8. As the k-means method groups data based solely on

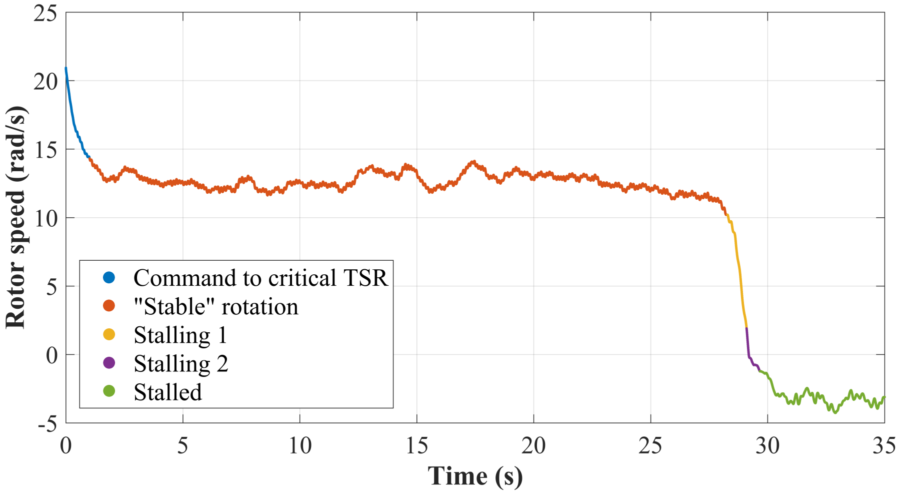

Figure 2.6: Time series of ω_t during typical stall event clustered into distinct regions.

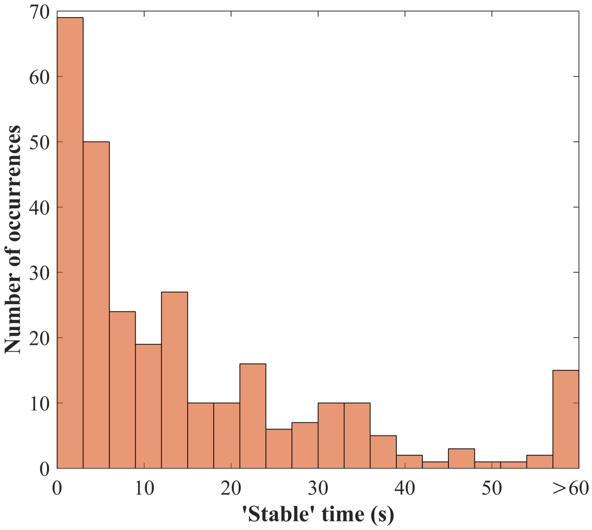

Figure 2.7: Distribution of time classified as ‘stable’.

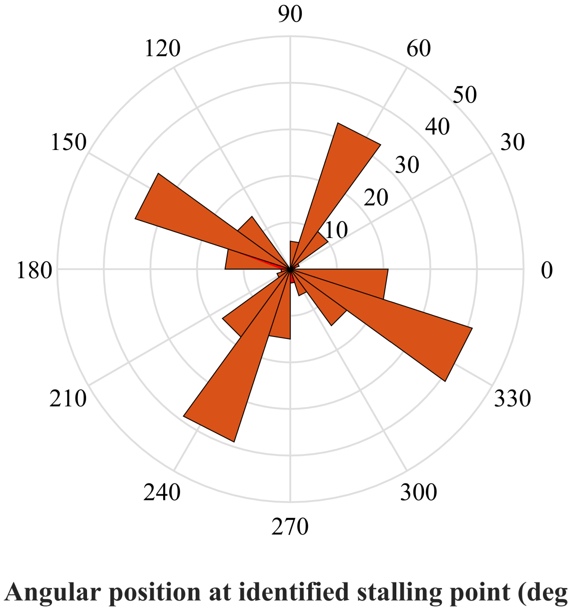

Figure 2.8: Distribution of angular position at cluster transition point of system stall.

similarity, the identified angular position at this point is not considered the definitive rotor state at the onset of system stall; indeed, this 'stalling' point shifts with changes to the input to the identification algorithm such as number of groups or included parameters. However, the presence of this distinct, repeatable pattern does indicate angular position is playing a role in the onset of system stall, as will be subsequently discussed.

2.3.2 Inflow Conditions Leading to Stall

The correlation coefficient between ω_t and U_∞ (ADV measurements with advection correction) is 0.33 for cases where stall occurred between 20 s and 40 s after test initiation and 0.37 for cases where the turbine did not stall. Additional moving-moving average smoothing of U_∞ over 2000 samples (corresponding to 2 s) yielded the highest correlation for non-stalling cases, increasing it to 0.46. Turbulence intensity averages 5% for stalling cases as well as non-stalling cases. Mean inflow speed is nearly identical for all cases at 1.00 m/s. Lower

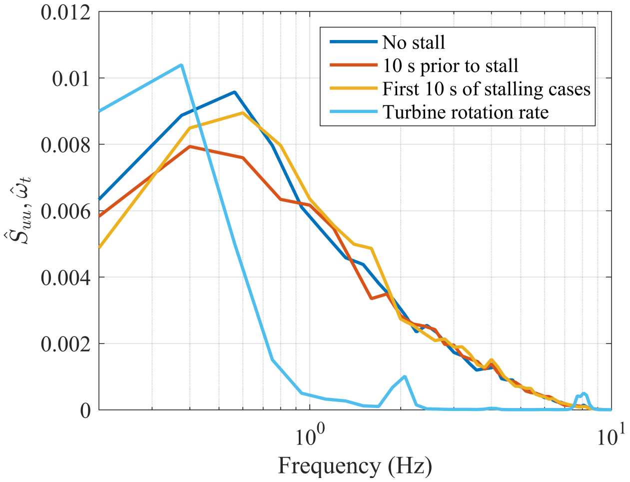

Figure 2.9: TKE of inflow & power spectral density of ω_t for no-stall cases and TKE of first 10 s and 10 s preceding system stall for instances of stall between 20 s and 40 s.

correlation for the stalling instances indicates a simple method of tracking inflow magnitude over time upstream of the turbine may not be sufficient for predicting system stall.

However, frequency domain analysis of the inflow reveals that, in cases where the turbine experiences system stall between 20 s and 40 s after test onset, there is less TKE at peak energetic frequencies in the 10 s prior to stalling than in 10 s samples of inflow speed in cases where the turbine does not stall (Figure 2.9). Additionally, TKE in the first 10 s of cases in which stall occurs is nearly identical to the no-stall cases. Rotation rate of the turbine varies with greatest intensity at low frequencies, with a sharp roll-off occurring between periods of 1.8 s and 2.8 s. The turbine's primary rotational frequency at λ_c of 2 Hz and blade passing frequency of 8 Hz are both visible as peaks.

Results from PIV flow analysis are presented for a case in which the turbine stalls after 19 s of time at λ_c. Average velocity magnitude over the 30 s realization and the entire interrogation window is 0.99 m/s. As the flow is non-homogeneous in both space and time, turbulent fluctuations ($\hat{U}_\infty$) are defined as a point-wise deviation from this ensemble average

[1] as,

$$\hat{U}_\infty = U - \infty - \langle \bar{U}_\infty \rangle_{x,y} \tag{2.3}$$

in which the overbar denotes a temporal mean and the brackets denote a spatial mean. Various modes of upstream flow are visualized in Figure 2.10. Over time, flow in the interrogation window oscillates about a mean configuration comprising of induction flow directly upstream of the rotor (lower than the mean), flow towards the center similar to the mean, and bypass flow higher than the mean adjacent to the rotor (Figure 2.10a). Periodic turbulent decreases (Figure 2.10b) and increases (Figure 2.10c) are shown to envelop the entire interrogation window. Induction is more apparent in the time prior to bringing the turbine to λ_c (Figure 2.10d), consistent with linear actuator theory which predicts higher thrust and axial induction at faster λ [14, 31]. While the turbine is in the process of decelerating to 0 rad/s, large turbulent gusts are observed (Figure 2.10e). After the rotor ceases rotation, flow is more homogeneous across the interrogation window (Figure 2.10f), consistent with a significant reduction in turbine thrust.

Differences in the flow in the induction and bypass zones are further quantified by averaging magnitudes in separate segments of the interrogation window over the cross-stream direction and time. Locations and dimensions of the zones are given in Figure 2.5. These means are then normalized by the cross-stream mean of the entire domain. Figure 2.11 shows that as the flow approaches the turbine in the streamwise direction, the velocity magnitude increases for the bypass flow and decreases in the induction zone, consistent with expectations. This averaging method necessarily smooths out cross-stream variation within the segmented regions, which tends towards faster flow with increasing y/D. Bypass flow is 3% faster than the mean, while induction flow is 2% slower. Flow uniformly increases in speed in the cross-stream direction from the rotor centerline out towards the bypass region when averaged over the entire x/D range, as seen in Figure 2.12, with flow at the edge of the interrogation window 5% faster than flow at the turbine centerline. Similarly, this method smooths out variation in the streamwise direction which tends towards faster flow further upstream from the rotor. As these figures show time averages of inflow speed, periodic and

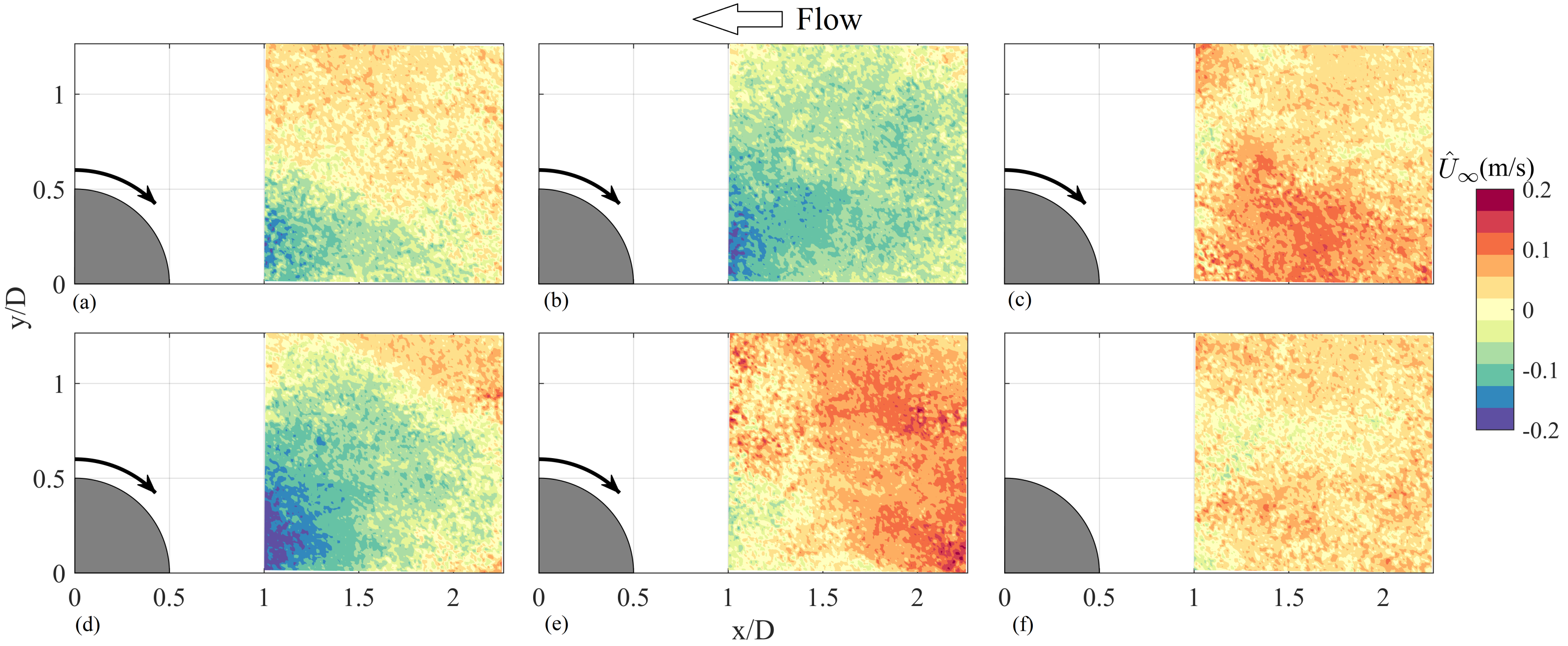

Figure 2.10: Summary of PIV velocity: (a) Typical operation, (b) Turbulent decrease, (c) Turbulent increase, (d) $\lambda > \lambda_c$, (e) While stalling, (f) Post-stall

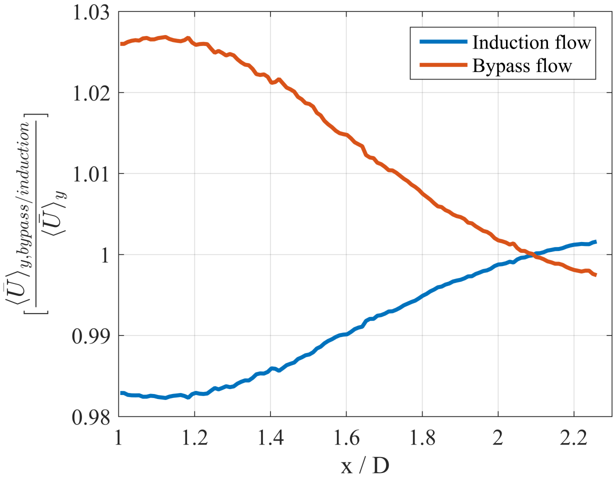

Figure 2.11: Variation of flow speed in the streamwise direction.

symmetric turbulent gusts and deficits are not represented.

Induction and bypass flow measured using PIV and upstream flow measured by the ADV are compared in Figure 2.13. The ADV (adjusted for advection) generally reports higher speeds than means computed from PIV vectors. Correlation in peaks between the ADV and PIV measurements indicate shifting velocity measurements taken upstream of a turbine in time according to the frozen field hypothesis is a valid technique. Additionally, after the turbine experiences system stall (indicated by a vertical line in Figure 2.13), flow magnitude in the bypass and induction zones converge to a more similar value.

In general, turbine rotation rate tracks changes to inflow with the rotor accelerating and decelerating in response to turbulent increases and decreases, as shown in Figure 2.14. This is consistent with expectations of changes to the turbine state while under control with constant τ_c. However, there is no clear change in the flow near the time the turbine begins to stall (about 19 s) that can be definitively correlated to system stall.

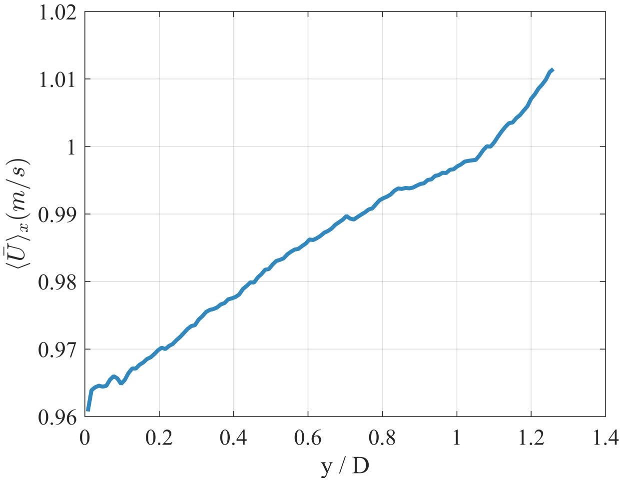

Figure 2.12: Variation of flow speed in the cross-stream direction.

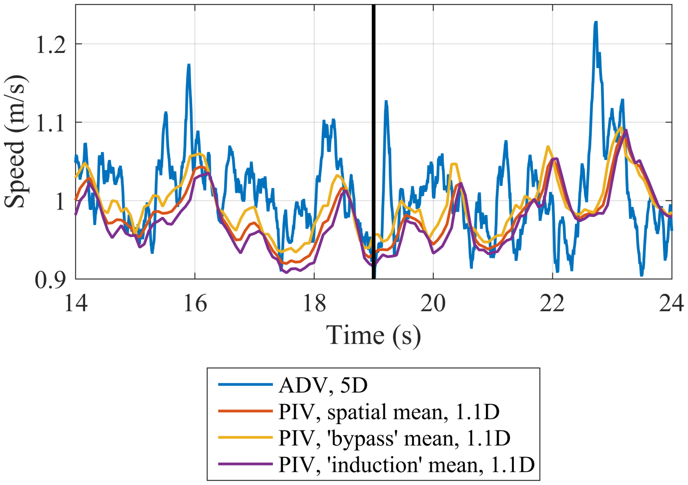

Figure 2.13: Comparison of ADV and PIV time series during stall event. Vertical line indicates onset of system stall.

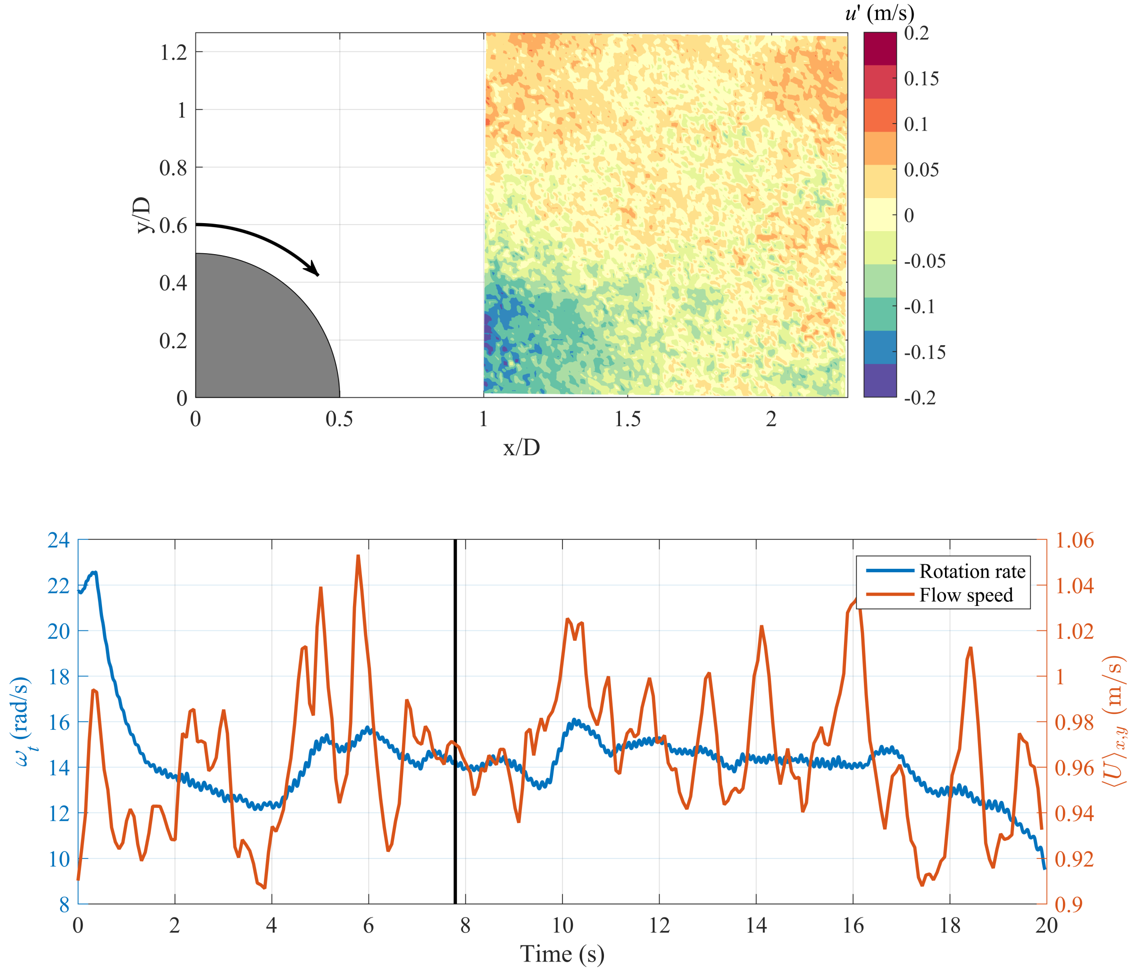

Figure 2.14: Rotation rate and spatial average of PIV speed during stall event with corresponding PIV snapshot indicated by vertical line.

2.4 Discussion & Conclusions

Designers of PTO systems for hydrokinetic turbines are actively investigating hardware and control strategies to operate more effectively in the regime slower than λ at maximum C_P [25, 3]. The methods and results of this work could help in understanding the risks and limitations of operating a turbine in this underspeed region. Marginal stability under torque regulation suggests speed control of the turbine (under which system stall cannot occur) should be utilized if the PTO is capable of enacting it. Otherwise, underspeed control with torque control requires a narrow operating range to avoid λ_c. Additionally, a turbine intended for use in the udnerspeed region would benefit by having performance characteristics tending towards operation at higher λ in general, resulting in further separation between the MPP and MTP.

A hydrokinetic turbine's proclivity to stall at a critical tip-speed ratio has been investigated both analytically and experimentally. Both quasi-steady and dynamic analysis indicate changes in inflow conditions or turbulent interactions with the turbine induce system stall. Additionally, a turbine was shown to be most susceptible to turbulent length scales on the order of and greater than the rotor dimensions (Chapter 1). Evidence of this behavior in an operating laboratory-scale turbine has been presented, with turbulent gusts on the order of the rotor diameter inducing corresponding changes in rotation rate. However, in the 10 s prior to system stall, less turbulent kinetic energy was present in the flow, and correlation between flow and rotation rate was lower. This indicates that for stable operation at λ_c, turbulent gusts may be necessary to maintain rotation but are not a sufficient condition.

Although evidence supporting a relationship between turbulence and system stall has been presented, no definitive events in the time series of inflow speed can be identified as directly culpable for inducing stall when it occurs. In several cases, such as the time series shown in Figure 2.14, the turbine experiences system stall after what appears to be a turbulent increase in flow speed. Instead, it is hypothesized that the time history of turbulence and its effect on the turbine's momentum over a longer time horizon on the order of seconds, or several complete rotations, leads to the conditions under which system stall may occur. This is consistent with indicators of the turbine's response to turbulence: system time constant (1.7 s), roll-of frequency range of variation in rotation rate (1/1.8 s to 1/2.8 s), and degree of smoothing of U_∞ yielding maximum correlation to rotation rate (2 s) are in agreement. Lack of correlation to flow observed within the turbine's bandwidth of response may be linked to three-dimensional flow (i.e., fluctuations at a location other than the turbine mid-plane) and were not capable of being investigated.

The k-means clustering technique did not use rotor position as a means of identifying distinct regions in time series of ω_t. However, the analysis indicated repeatability in the system stall process linked to position; the point identified as the border between 'stable' and 'stalling' predominately occurred at the same blade position. This indicates interactions between flow and the rotor at the scale of the blades are important at the point of marginal stability. These inter-rotational dynamics cannot be described by the characteristic curve model of a turbine, and are an active area of research. Cross-flow turbine power output and thus ability to produce torque has been shown to be a strong function of the angular position of the rotor blades for straight-bladed designs [75]. Though to a lesser degree, this is true of helical turbines under speed control as well, with τ_h varying with rotor position while at an average speed corresponding to λ_c, as shown in Figure 2.15.

Marginally stable operation at λ_c is shown to be possible for variable time, with system stall occurring most frequently after short amounts of time. The empirical probability distribution generated from the experiments may be used to refine dynamic simulations of the turbine. However, application of this result is only valid for the rotor presently studied. A similar experimental campaign would be needed to generate a probability distribution for system stall for any unique turbine geometry.

A linearized dynamic system model, quasi-steady analysis of a characteristic curve, and experimental results confirm the limit of stability for a cross-flow hydrokinetic turbine occurs at λ corresponding to the MTP.

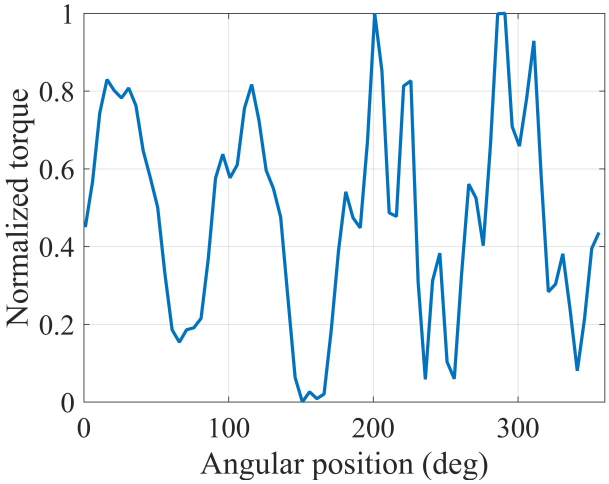

Figure 2.15: Phase-averaged normalized torque at λ_c for turbine regulated with speed control.

Chapter 3

FIELD PERFORMANCE ASSESSMENT OF A HYDROKINETIC TURBINE

The text of the following chapter was accepted for publication in the *International Journal of Marine Energy* in January, 2016. With the exception of reformatting the text, adjusting nomenclature to maintain consistency throughout this document, and including references to other chapters, no changes were made to the content of the article as accepted. The citation for the paper, pending final publication, is as follows:

Cavagnaro, R. J., Polagye, B., Field Performance Assessment of a Hydrokinetic Turbine, *International Journal of Marine Energy (IJOME)*, (*in press*), doi: 10.1016/j.ijome.2016.01.009.

3.1 Introduction

Development of hydrokinetic turbines used for electricity generation involves advancing systems through technology readiness and performance levels to commercialization [71, 85]. Field testing of scaled prototypes is a critical phase of development following laboratory experimentation and addresses two potential limitations under laboratory conditions. First, a turbine's hydrodynamic performance and thrust can be augmented in confined flow (such as a recirculating laboratory flume or tow tank) due to increased mass flux through the turbine and accelerated flow around the turbine, resulting in a higher pressure drop across the rotor [23]. Second, below a critical Reynolds number, where the lift and drag coefficients of hydrofoils depend on current velocity, rotor performance also depends on current velocity [65, 4, 29]. Because hydrofoils in a cross-flow turbine (rotation axis perpendicular to direction of flow) undergo dynamic stall as a consequence of large changes in the angle of attack, a critical Reynolds number cannot be accurately determined from static foil data [51]. In a laboratory setting, it can be difficult to achieve Reynolds independence due to limitations on maximum velocity in experimental facilities and the aforementioned consequences of flow confinement as model size increases.

In addition, laboratory characterization often does not involve a complete PTO. These components can critically affect the dynamics and performance of hydrokinetic systems [2]. Therefore, prototype tests including a PTO (e.g., gearbox, generator, electrical load) are necessary to quantify overall system performance. Total system efficiency (η_s) is defined as the fraction of available kinetic power, (P_k) converted to electrical power (P_e),

$$\eta_s = \frac{P_e}{P_k}. \tag{3.1}$$

A turbine's mechanical efficiency, referred to as the coefficient of performance (C_P), is given by

$$C_P = \frac{P_m}{P_k} = \frac{\tau_h \omega_t}{\frac{1}{2}\rho A U_\infty^3} \tag{3.2}$$

where τ_h is the rotor (low-speed shaft) hydrodynamic torque, ω_t is the rotor rotation rate, together defining mechanical power (P_m), ρ is the density of water, A is the projected area, and U_∞ is the undisturbed upstream water velocity. The projected area of a cross-flow turbine is defined as

$$A = 2rH \tag{3.3}$$

where H is the height of the rotor and r is its radius. The coefficient of performance under a given oppositional load can be compared to the tip-speed ratio (λ), defined as (1.1). In unconfined flow above a critical Reynolds number, the combination of C_P and λ result in a performance curve unique to the turbine geometry.

If τ_h, ω_t, and U_∞ are measured, total system efficiency can be determined with further knowledge of individual PTO component efficiencies, such as those of a generator (η_g), gearbox (η_b), and additional mechanical and electrical losses (η_m),

$$\eta_s = C_P \eta_g \eta_b \eta_m. \tag{3.4}$$

PTO component manufacturers often provide a single value for efficiency at implied peak or rated operating conditions, but the actual efficiency may depend on a number of factors, such as output torque in comparison to rated torque [69].

This chapter presents the system performance of a field-scale hydrokinetic turbine (nominally, 1kW rated mechanical power). Performance is characterized utilizing multiple methods, including one that reduces the number of direct measurements required. The efficiency of the PTO generator and gearbox are explored through laboratory dynamometry. Performance characteristics determined at the scale studied in this work may be compared to those of a quarter-scale model (Chapter 2 & Appendix A) with similar geometry tested in a recirculating flume to demonstrate differences related to scale [65, 17]. A comparison of performance between the laboratory and field-scale turbine is provided in Appendix C. Additionally, sufficient detail of the turbine design, test conditions, and performance is provided such that the results may be used to validate numerical studies. In Section 3.2, the turbine is described and its instrumentation and field testing methodology are detailed. Additionally, the method of laboratory dynamometry used to characterize PTO components is developed. Results from field testing and dynamometry are presented in Section 3.3. The implications of these results are discussed in Section 3.4. Overall, this study provides a detailed picture of the performance of a field-scale hydrokinetic turbine in open-water conditions and recommendations to improve the efficacy of field testing.

3.2 Methods

3.2.1 Turbine and Instrumentation Description

The field-scale turbine (Figure 3.1) is a helical, cross-flow design with circular endplates for blade attachment and a central shaft for support and PTO integration. Its four blades are mounted at the half-chord point with 0°preset-pitch with respect to the tangent of the circumference of the turbine at the endplate. Each blade consists of a straight profile helically swept around 90°(ϕ) of the circumference with a helical pitch angle (θ_p) of 60°. Consequently, the four blades' chords (c) provide complete coverage of the rotor circumference. The turbine is supported with a steel radial ball bearing at the top of the rotor shaft, and a combination radial needle and thrust bearing (Misumi) at the bottom of the shaft. The turbine is enclosed in a four-post support cage that includes mounting points. Turbine solidity (σ) is 0.3, defined as,

$$\sigma = \frac{Nc}{\pi D} \tag{3.5}$$

where N is the number of blades and D is the diameter of the turbine, and represents the fraction of the rotor's total swept area (πDH) occupied by blade and ranges from 0 to 1 [73]. This definition is preferred over a version commonly used for wind turbines as in [62], which compares blade area to rotor projected area. As swept area and projected area are equal for an AFT, defining solidity as (3.5) represents an equivalent quantity for a CFT. The solidity of the presently studied turbine is relatively high and has the effect of increasing starting ability with more consistent torque at the expense of peak C_P and rotation rate [73]. Dimensions for the turbine are reported in Table 3.1.

The PTO consists of a planetary gearbox (Thomson UltraTRUE) and a permanent magnet generator (WindBlue DC-540). The gearbox ratio (N_b) is 10 and the relation between generator (high-speed shaft) rotation rate (ω_g) and torque (τ_g) and low-speed shaft (turbine rotor) values are given as,

$$\omega_g = N_b \omega_t \tag{3.6}$$

$$\tau_g = \frac{\tau_h}{N_b} \eta_b \eta_m \tag{3.7}$$

where $\eta_b \eta_m$ is the balance of system efficiency, primarily associated with torque losses through the gearbox. Three-phase, AC power produced by the generator is transformed through a full-wave diode rectifier to yield DC power. This is dissipated through a 10-position adjustable resistive bank with loads (R) ranging from 0.3 Ω to 1000 Ω, providing discrete torque control on the turbine through the PTO. Angular position of the drive shaft is measured with a submersible magnetic encoder (RLS RM22) and thru-shaft optical encoder (Futek TRS605). ω_t is calculated by a first-order backwards difference of the angular posi-

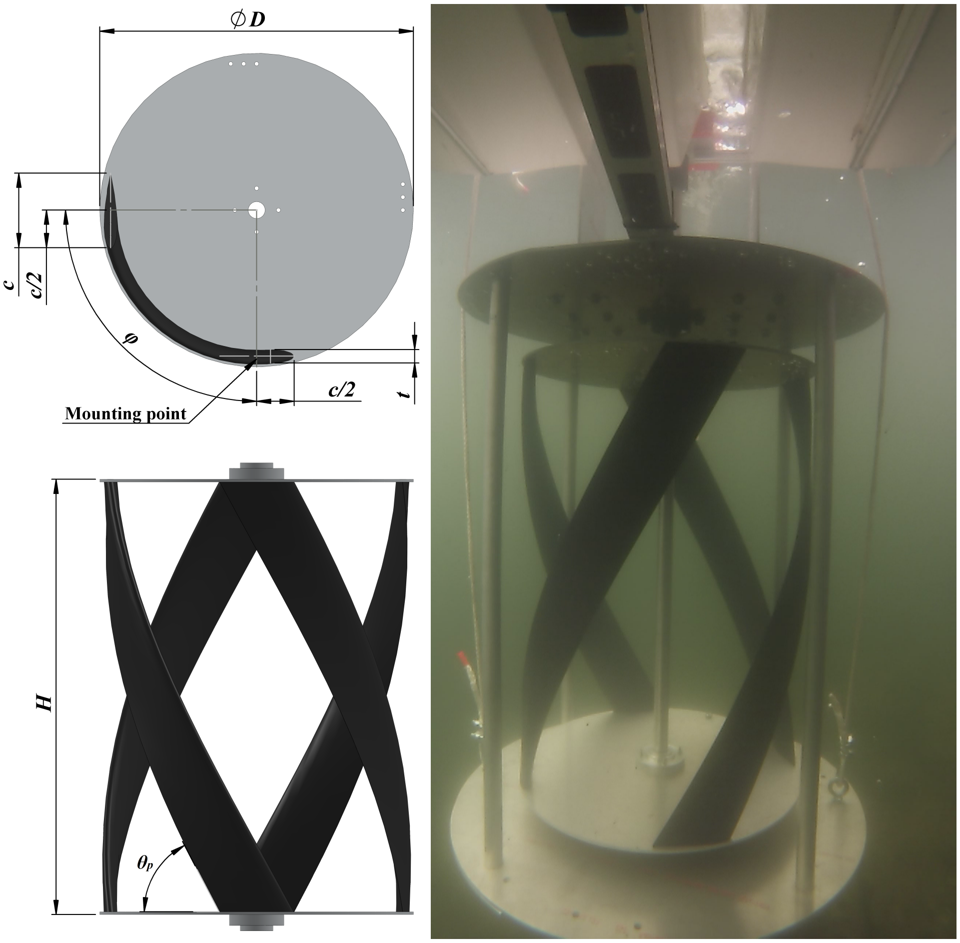

Figure 3.1: Field-scale hydrokinetic turbine.

Table 3.1: Turbine parameters and dimensions.

Parameter	**Value**
Blade profile	NACA 0018
Number of blades (N)	4
Blade pitch at mount point	0°
Turbine diameter (D)	0.724 m
Turbine height (H)	1.013 m
Turbine aspect ratio (H/D)	1.40
Helical pitch angle (θ_p)	60°
Helical sweep angle (ϕ)	90°
Blade chord length (c)	0.173 m
Blade thickness (t)	0.031 m
Solidity ratio (σ)	0.30

tion. During field tests, generator instantaneous voltage (V) and current (I) are measured across the resistive load by transducers (LEM LV 25-P and LA 55-P, respectively). Mechanical torque produced by the turbine is measured by a rotary torque sensor (Futek TRS605). Although torque losses associated with bearing friction are unquantified, the output of the torque sensor is considered to be a direct measurement of τ_h. All turbine performance data is acquired at a sampling rate of 100 Hz through a USB DAQ (National Instruments 6210) connected to a laptop computer. Inflow velocity is acquired at 32 Hz near the centerline of the turbine with an acoustic Doppler velocimeter (ADV, Nortek Vector) mounted two turbine diameters upstream of the rotor centerline.

3.2.2 Turbine Testing Method

In the field, relative velocity can be induced by placing a turbine in a moving flow (analogous to a recirculating flume at laboratory scale) or by translating a turbine through quiescent flow (analogous to a tow tank at laboratory scale). The latter method was employed in these tests, towing the turbine through an open portion of a still lake (Lake Washington, WA, USA) with a depth greater than 5 m. Testing occurred on calm days with negligible wind waves. A dimensioned schematic of the test arrangement is depicted in Figure 3.2. The system was mounted to the transom of a small unpowered catamaran-hulled vessel (Livingston LV12) and positioned such that the top of the rotor sat at a depth per diameter ratio (z/D) of roughly 0.7 below the surface of the water. The drive shaft extended above the surface and was coupled to the torque sensor, gearbox, and generator. These were supported by a rigid mounting to the vessel to reduce vertical thrust loads on the shaft. The torque sensor was protected in a water-resistant enclosure, including a double O-ring seal. The generator was connected to the load bank aboard the vessel. The test vessel was tethered to a powered vessel approximately 100 m upstream, reducing the impact of the powered vessel wake on turbine performance. The vessel was piloted at three approximately constant speeds of 1.0 m/s, 1.6 m/s, and 2.1 m/s corresponding to blade-chord Reynolds numbers (U_∞ velocity reference) of $1.5 - 3.3x10^5$. Each of the ten resistive load settings was maintained for approximately 45 s after a steady rotation rate was reached (e.g., after transient from adjusting load settings). Care was taken to avoid contamination by interaction of the towed vessel with large wakes from other vessels on the lake; test runs in the presence of such wakes were aborted. Vessel pitch was monitored with a mechanical level and maintained near-neutral by shifting ballast between the bow and stern under different test conditions. Pitch angle was also recorded throughout testing by the inertial measurement unit (IMU) on the ADV. The ADV measured the upstream velocity in a small sample volume ($1.8x10^{-6}$ m^3) at a distance of 0.15 m below the probe head. The velocity at this point was assumed to be representative of the inflow across the rotor swept area. This is reasonable, given that the turbine was being towed through a quiescent fluid, such that inflow velocity varies in time, but was homogeneous in space. Given the similarity between the upstream tow vessel speed and average inflow velocity, angular and axial induction appear to be minimal at this proximity ($2D$) to the turbine. A square-profile bracket (0.09 m wide) was used to mount the ADV head. Turbulence generated by the bracket is unlikely to significantly affect turbine performance for two reasons. First, the characteristic dimension of the bracket is much smaller than the rotor diameter and smaller than the blade chord, such that the generated turbulence would be unlikely to affect performance [22]. Second, the turbine was 17-times the profile dimension downstream of the ADV, such that the turbulent eddies shed by the ADV would be substantially mixed with the free stream.

Velocity measurements were de-spiked by a 3-D phase-space algorithm [52]. To characterize turbulent inflow conditions, measurement samples of 300 s were selected from extended tows at each of the nominal speeds used for performance characterization tests. Linear trends were subtracted and then each time-series was split into windows of 32 s, a Hamming filter applied, and each window overlapped by 50% [82]. Spectra for each window were averaged to yield a single turbulence spectrum for each speed with narrow confidence intervals [80]. A standard bulk metric for describing turbulence [81], turbulence intensity (I_U) was also calculated as the ratio of the standard deviation of the inflow speed (σ_U) to its temporal

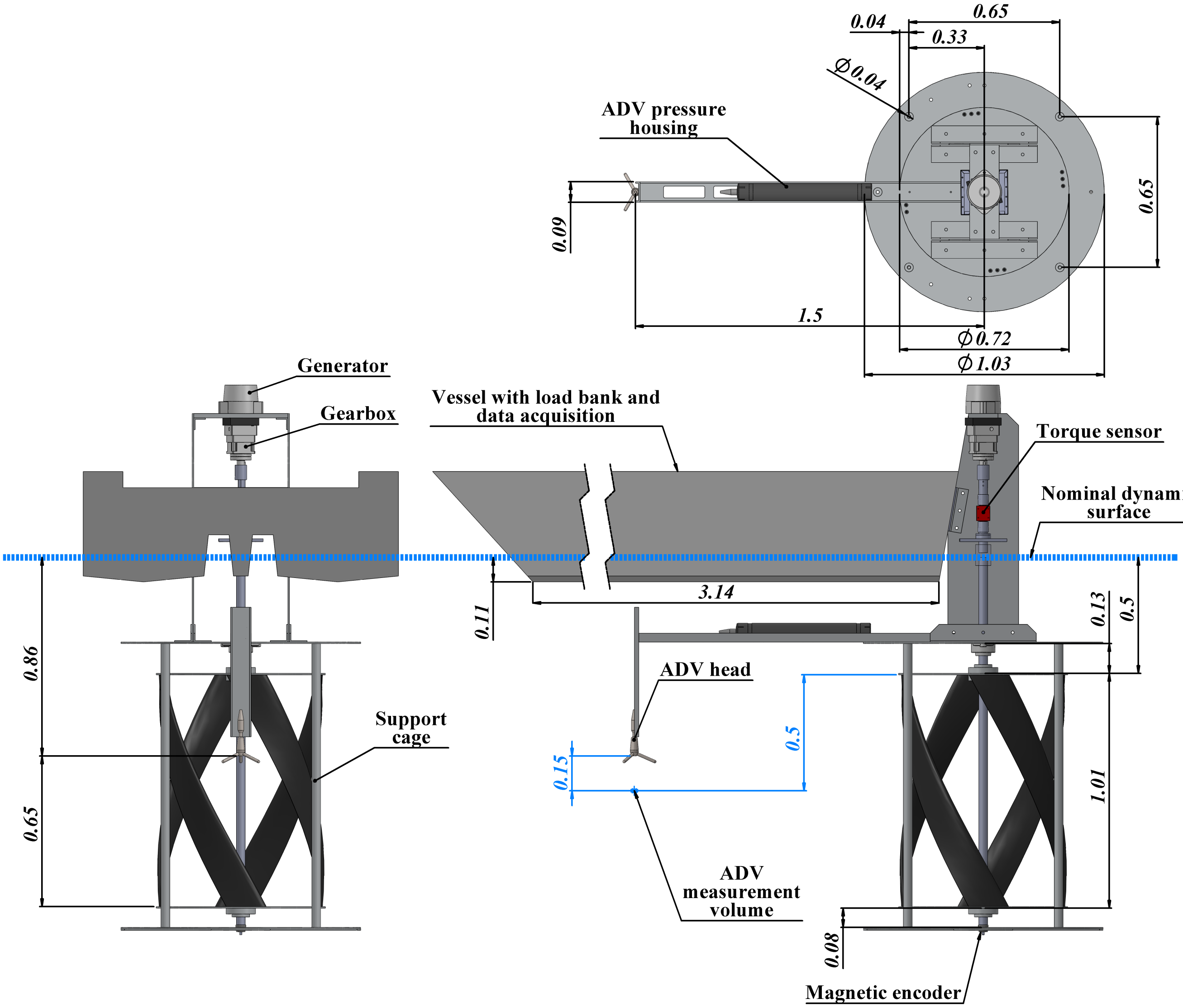

Figure 3.2: Field-scale tow testing schematic.

mean ($\bar{U}_\infty$),

$$I_U = \frac{\sigma_U}{\bar{U}_\infty}. \tag{3.8}$$

3.2.3 PTO Dynamometry

A laboratory dynamometer (Figure 3.3) was used to characterize η_g, using a second generator identical to the one coupled to the turbine as the mechanical power input to the PTO. This generator was operated as a variable speed motor controlled with a variable frequency drive (VFD) (Yaskawa V1000). This motor was mounted to a reaction torque sensor (Futek TFF425) measuring input torque, $\tilde{\tau}_g$, and was flexibly coupled to the generator. Note that here, and for the remainder of the chapter, any quantity with a tilde denotes a laboratory dynamometry measurement. An optical encoder (Encoder Products 260) on the dynamometer shaft recorded angular position (used to determine shaft rotation rate, $\tilde{\omega}_g$). The generator under test was connected to the same 10-position resistive load bank used in the field testing to record dynamometry voltage and current, $\tilde{V}$ and $\tilde{I}$, respectively. The motor was commanded to run over a range of speeds from 10 to 1000 rpm at each of the resistive loads, including specific tests that matched average generator-side rotation rate and resistive load from the field trials. Commanding the same constant rotation rate under the same R electromechanically emulates the turbine at steady state in the laboratory, including the torque produced. Generator efficiency was calculated from these measurements as,

$$\eta_g(R, \omega_g) = \frac{\tilde{V}\tilde{I}}{\tilde{\tau}_g\tilde{\omega}_g}. \tag{3.9}$$

The electromechanically emulated turbine system in the dynamometry experiment differs from the actual turbine system of field testing in its lack of a gearbox and lack of frictional losses associated with the turbine bearings. Therefore, the difference in electrical power output between tests with the same mechanical input (rotation rate and applied load) represents the losses associated with the gearbox and bearings in the field test. If frictional losses in

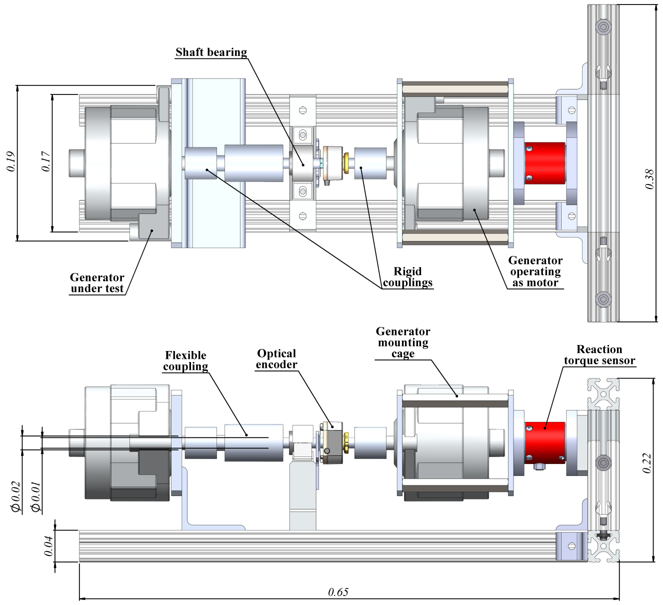

Figure 3.3: Generator characterization dynamometer.

the dynamometer are neglected, $\eta_b\eta_m$ can be expressed as,

$$\eta_b\eta_m = \frac{VI}{\tilde{V}\tilde{I}}. \tag{3.10}$$

3.2.4 Mechanical Efficiency Calculation

Non-dimensional mechanical efficiency ($C_P(\lambda)$) was evaluated through two independent tests: utilizing direct torque and rotation rate measurement from field measurements to solve for C_P in (3.2) directly, and deriving C_P by applying corrections for PTO efficiency to the total system efficiency as in (3.4). Field and laboratory tests are equated by setting the dynamometry generator speed to match those obtained in the field under the same R,

$$\tilde{\omega}_g = \omega_g \tag{3.11}$$

$$\tilde{\tau}_g = \frac{\tau_g}{\eta_b\eta_m} = \frac{\omega_g K_V^2}{\eta_b\eta_m R} \tag{3.12}$$

where K_V is the generator's voltage constant (V/rad/s), which does not change between field and laboratory testing. The relation between mechanical efficiency, resistive load, and rotation rate is apparent by substituting (3.1) in (3.4),

$$C_P(R, \omega_g) = \frac{P_e}{P_k}\frac{1}{\eta_g \eta_b \eta_m} \tag{3.13}$$

and then (3.2), (3.9), and (3.10) in (3.13),

$$C_P(R, \omega_g) = \frac{VI}{\frac{1}{2}\rho A U_\infty^3}\frac{\tilde{\tau}_g \tilde{\omega}_g}{\tilde{V}\tilde{I}}\frac{\tilde{V}\tilde{I}}{VI} = \frac{\tilde{\tau}_g \tilde{\omega}_g}{\frac{1}{2}\rho A U_\infty^3}. \tag{3.14}$$

Consequently, the mechanical efficiency is the ratio between the mechanical power needed to emulate the turbine at steady state and the kinetic power of the resource. While the final form of (3.14) is functionally similar to (3.2), it is important to note that the numerator here corresponds to an emulated, rather than actual, turbine that performs independently of the PTO components. As discussed in Section 3.4, this relation is critical to enabling C_P to be inferred from field data with a limited number of measurements (ω_t, U_∞, and R).

3.3 Results

3.3.1 Inflow Characteristics

During tests, inflow speeds measured by the ADV averaged 1.0 m/s, 1.6 m/s, and 2.1 m/s, in general agreement with target tow vessel speeds of 1 m/s, 1.5 m/s, and 2 m/s with deviation between the two caused by discrete throttle settings for the powered vessel. In Figure 3.4, turbulence spectra in the tow-induced inflow are compared to those measured while the vessel was freely drifting in the lake and with a comparable mean speed at a representative tidal energy site (Admiralty Inlet, WA, USA) [80]. During testing, turbulence spectra exhibited slight variation with tow speed. Low frequency peaks (2-5 s) were present while towing or drifting as a consequence of interactions with small wakes from other vessels, and oscillations in tow vessel velocity. As evidenced by studies of wave-current interaction, low frequency disturbances do not significantly affect mean values [35, 47]. The peak observed at 5.5 Hz for the 1.6 m/s and 2.1 m/s spectra was likely the result of motion contamination

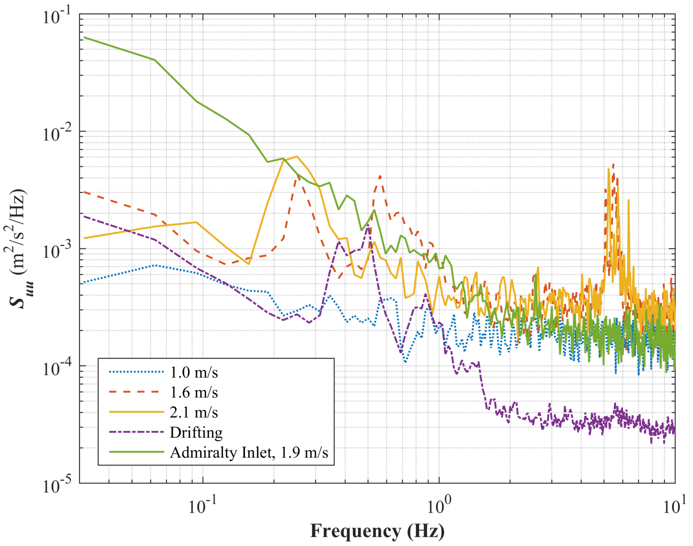

Figure 3.4: Turbulent kinetic energy spectra of field test inflow.

from mechanical vibration transmitted through the cantilevered instrument mounting arm, consistent with increasing energy at higher inflow velocities. Beam correlation averaged 80%, indicating limited interference from surface effects such as bubbles. Speed measured by the ADV while freely drifting averaged 0.07 m/s. The average pitch angle during characterization tests, as measured by the ADV, ranged from 2.2°to 4.0°. Inflow turbulence intensity was 5.6% at 1.0 m/s and 1.6 m/s, and 4.1% at 2.1 m/s. This level of turbulence is ascribed to the wakes, waves, tow vessel propeller wash, and tow speed variation responsible for the spectral peaks. Turbulence intensity was lower than during similar mean flow in Admiralty Inlet (7.5% for the reported sample). The spectra for the tows were flatter than those from Admiralty Inlet, lacking lower frequency, higher energy variation associated with tidal forcing and large anisotropic eddies; these features are not present in the lake.

3.3.2 Turbine Performance

System efficiency, η_s (Figure 3.5a) varied between tests at the three nominal inflow speeds, resulting in three distinct curves with a maximum efficiency of 0.09 at 1.0 m/s and 1.6 m/s, dropping to 0.07 at 2.1 m/s. The $\eta_s(\lambda)$ curve also contracts as inflow velocity increases, with peak efficiency occurring at higher λ. Generator and balance of system efficiencies were estimated for each of these test cases using laboratory dynamometry and (3.9)-(3.10), as shown in Figure 3.5b. The PTO component performance varied non-linearly with λ. PTO efficiency ranged from a minimum of 0.02 to a maximum of 0.67. The PTO efficiency correction from (3.14) was applied to the field results for each test case, yielding a derived $C_P(\lambda)$ curve. In Figure 3.5c, these points are compared to those obtained by measuring torque and rotation rate directly. In all cases, cubic polynomials were fit to the experimental data to more clearly demonstrate trends. Peak measured performance, implied peaks from the polynomial fit, and quality of the fit are summarized in Table 3.2. Through direct measurement and correction for pointwise PTO efficiency, the $C_P(\lambda)$ curves are in general agreement between tow conditions and are significantly less dependent on inflow velocity than the $\eta_s(\lambda)$ curves. Much of the remaining variability in the magnitude of C_P falls within the bounds of random and systematic experimental uncertainty, shown as error bars in the plot (calculation in Appendix B). However, both direct and derived curves for the 1.0 m/s case show lower performance than the faster speeds. The case with largest variation and uncertainty in the observed trends of performance is the 1.6 m/s derived curve, which exhibits peak performance at a 9% lower λ than the direct measurement at this speed. In general, the uncertainty is higher for the derived curves due to the uncertainty in the dynamometer torque measurement calibration (discussion in Appendix B) and may be systematically biased towards lower C_P, though percent difference between measured and derived values is demonstrably low. Reduced performance at the slowest tow speed may be ascribed to either higher relative frictional losses at low rotation rates or exceeding the critical Reynolds number between 1.0 m/s and 1.6 m/s tow speeds.

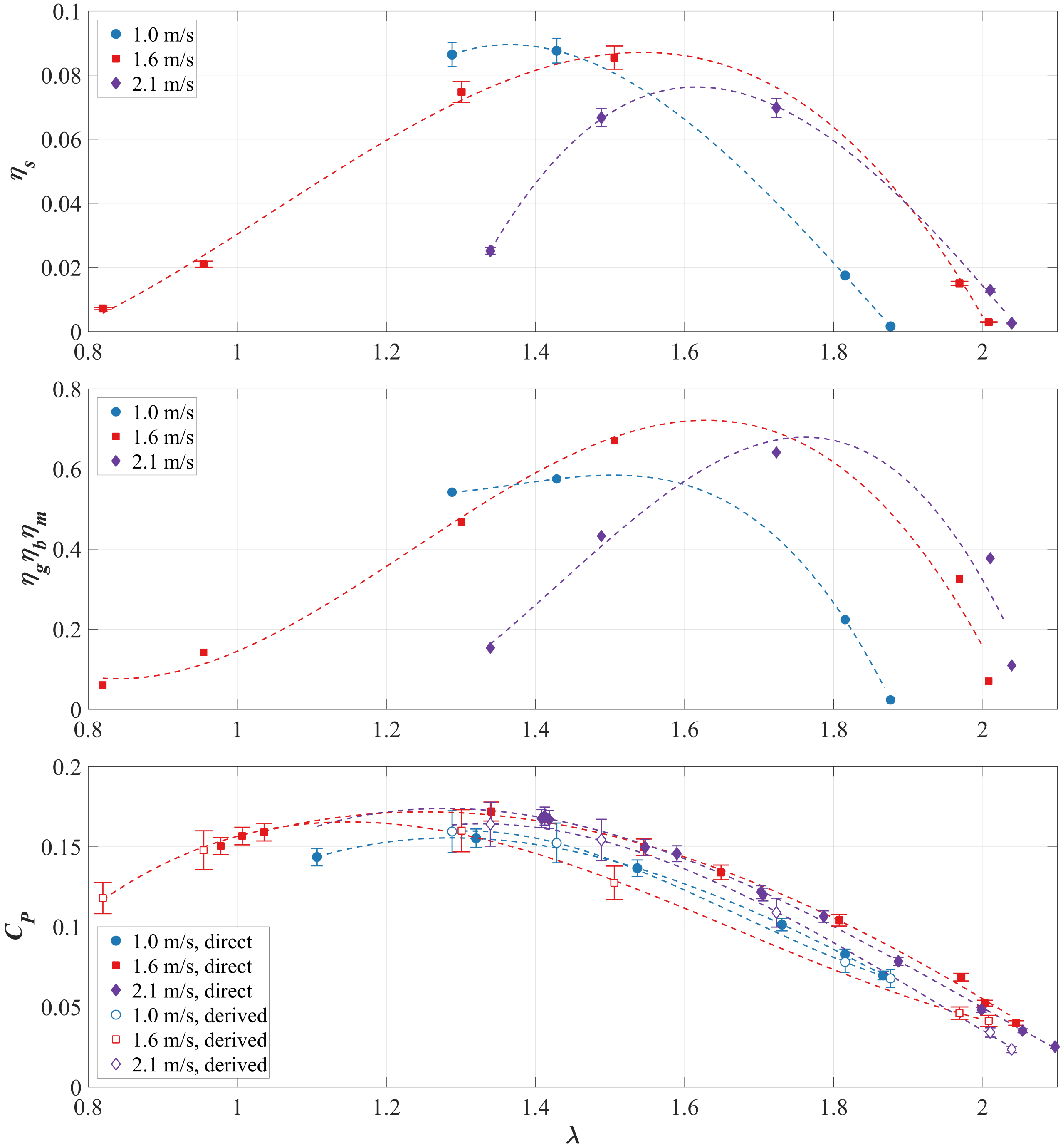

Figure 3.5: System efficiency (a), PTO efficiency (b), and rotor mechanical efficiency (c).

Table 3.2: Peak performance results from measurements and cubic polynomial fits

	Measurement						**Polynomial Fit**								
	Peak Value			**Associated λ**			**Peak Value**			**Associated λ**			**R^2**		
	1.0 m/s	1.6 m/s	2.1 m/s	1.0 m/s	1.6 m/s	2.1 m/s	1.0 m/s	1.6 m/s	2.1 m/s	1.0 m/s	1.6 m/s	2.1 m/s	1.0 m/s	1.6 m/s	2.1 m/s
η_s	0.088	0.086	0.070	1.43	1.50	1.72	0.090	0.087	0.076	1.34	1.54	1.62	1.00	1.00	1.00
$\eta_g\eta_b\eta_m$	0.575	0.670	0.641	1.43	1.50	1.72	0.585	0.722	0.679	1.51	1.63	1.76	1.00	0.97	0.92
C_P (Direct)	0.155	0.172	0.169	1.32	1.34	1.41	0.156	0.172	0.174	1.29	1.25	1.28	1.00	1.00	1.00
C_P (Derived)	0.160	0.160	0.164	1.29	1.30	1.34	0.160	0.165	0.164	1.31	1.15	1.33	1.00	1.00	1.00
% Diff. of Direct and Derived C_P	-3.2	7.0	3.0	2.3	3.0	5.0	-2.6	4.0	5.7	-1.6	8.0	-3.9			

3.3.3 PTO Component Performance

The generator and balance of system (primarily gearbox) efficiencies depend on the combination of load and rotation rate of each steady-state test case. The generator efficiency (Figure 3.6a), determined through dynamometry and the application of (3.9), utilized the electrical output measurements from the generator at known mechanical power points. The results indicate generally poor performance at low power outputs (<45W) regardless of rotational speed. η_g ranged from a minimum of 0.08 to a maximum of 0.70. Balance of system performance (Figure 3.6b) was higher and less variable under the same conditions, with the exception of test points at low power and rotational speed, where the turbine was likely stalling. Excluding these outlying cases, $\eta_b\eta_m$ ranged from 0.66 to 0.98, with no clear trend in performance.

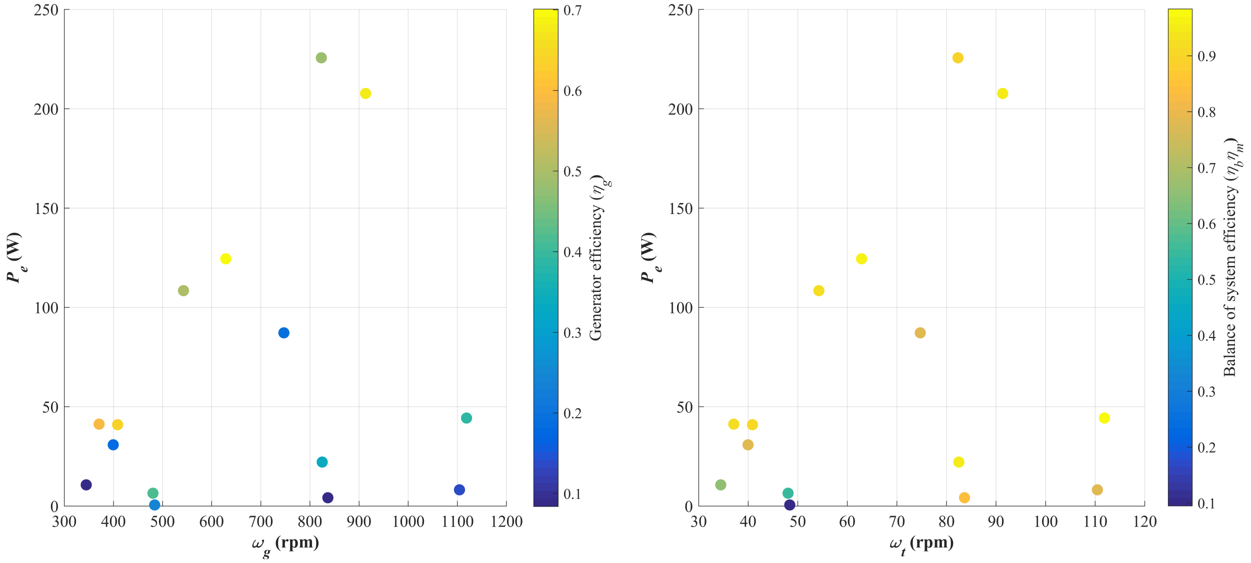

Figure 3.6: Generator (a) and balance of system efficiency (b).

3.4 *Discussion*

A non-dimensional performance curve distills a turbine's hydrodynamic characteristics into a concise functional dependency on its tip-speed ratio as long as the turbine is operating at sufficiently high Reynolds number. Determination of a $C_P(\lambda)$ curve, with an estimate of uncertainty, is an essential step in turbine development and serves as a starting point for advanced control strategies. For example, a variable-speed controller tracking a maximum power point requires accurate knowledge of a turbine's optimal operating conditions [18]. The methods and results of this study provide an accessible example of a field-scale turbine tested in open-water conditions with a complete PTO. Such results are not well-described in the literature.

The lake used for this testing provides lower turbulence than in a tidal channel and eliminates flow confinement effects common in a laboratory. Inhomogeneity in the inflow associated with small waves from wakes can be mitigated by sampling for much longer than the dominant period of the disturbances. An ADV was used to measure inflow conditions at the centerline of the turbine, which is likely representative of flow across the rotor in a quiescent lake. While a current profiler could be used to measure vertical variation along the blade span, this would come at the cost of reduced temporal resolution and higher uncertainty. The ADV provided the resolution to better characterize turbulent flow interaction with the turbine. Future studies utilizing this method may consider also deploying profiling instruments as part of the test.

The helical CFT's peak C_P of 0.17 at λ of 1.3 is 50% lower than previously reported results for a helical turbine at a similar scale tested in a tow tank [5]. Several factors may account for the difference. First, the higher solidity (0.3 vs. 0.14) of the present study's turbine favors an ability to self-start at low speed (0.5 m/s) at the cost of efficiency. Second, the turbine is tested in the absence of blockage, which would augment turbine efficiency. Bachant & Wosnik's [5] experiments were conducted at a blockage of 15%. This would be expected to modestly enhance efficiency, but the effect is difficult to quantify, given that commonly-used blockage corrections have been shown to be unreliable for a quarter-scale model of the presently studied turbine [17]. Similar to the present study, Shiono et al. [73] report a C_P range of 0.20 to 0.23 for a high blockage cross-flow turbine in a flume. Additionally, Kirke [42] describes a peak C_P of 0.25 for a similarly scaled cross-flow turbine with roughly half the solidity of the presently studied design. Laboratory-scale experiments of a two-bladed version of the rotor (currently unpublished) yielded substantially higher performance, but power input was required to commence rotation.

The consistency of the non-dimensional turbine performance at inflow speeds of 1.6 m/s and 2.1 m/s (Reynolds numbers of 2.4 and $3.3x10^5$) suggests that these conditions exceed the critical Reynolds number. The turbine performs with a slightly lower efficiency at the lowest Reynolds number tested ($1.5x10^5$). This discrepancy could either result from a Reynolds independence threshold between 1.5 and $2.4x10^5$ or the turbine experiencing higher relative frictional losses when operating at lower rotation rates.

PTO component performance is shown to substantially influence both the total system efficiency and the tip-speed ratio associated with peak efficiency. Dependence of η_g on both rotation rate and power output results in $\eta_s(\lambda)$ curves that are inflow dependent. Indeed, the poor performance of the generator highlights the importance of properly selecting or designing a generator with an operating range compatible to that of the rotor. This can be challenging for prototype field tests given the limited number of low-cost generators designed to operate at relatively low rotation rates and the limited documentation for such systems. Gearbox and balance of system efficiencies also exhibit a dynamic range, but have a less substantial influence on overall performance. In general, it is recommended to conduct performance testing with a complete PTO system since system efficiency is of critical importance in evaluating technology readiness. However, these field tests demonstrate that PTO component efficiencies must be well-characterized to interpret total system performance.

A method of dynamometry that includes electromechanical emulation of the turbine is used to determine individual PTO component efficiencies. Only a small subset of possible field and lab measurements is required to accurately produce a $C_P(\lambda)$ curve from field trials. By utilizing a discrete and repeatable loading scheme in both the field and laboratory, U_∞ and ω_t become the only necessary field measurements, while $\tilde{\tau}_g$ and $\tilde{\omega}_g$ are the only necessary dynamometry measurements. This is because, with steady loading, a turbine's operating state is fully defined by its rotation rate. This allows field measurements of τ_h, which can be difficult to obtain, to be replaced by an equivalent torque commanded for and produced by a motor in a laboratory setting. Accuracy of the derived performance curve is confirmed through comparison with a curve produced from direct measurement of the turbine's mechanical power. This method has the potential to reduce the complexity and cost of field studies for prototype hydrokinetic turbines.

3.5 Conclusions

The performance curve, PTO efficiency, and individual component efficiencies of a fully-instrumented hydrokinetic turbine are determined through a combination of field and laboratory experiments. Tow testing through a quiescent lake is shown to be an effective method for performance characterization, providing open-water, low turbulence conditions. The relatively poor prototype system performance is attributed to the high-solidity rotor (low peak C_P) and generator (low, variable η_g).

A PTO testing method is presented that allows simultaneous determination of generator and balance of system efficiencies at the same operating points as those realized during field testing. This method emulates the steady-state behavior of the turbine and can be utilized to reduce the number of necessary measurements in the field. The generator is shown to be a poor match for the turbine, while the gearbox and balance of system losses were found to be less significant. Low and highly varying generator efficiency is shown to have a strong impact on total system efficiency, leading to a strong, counter-intuitive variation in performance with inflow velocity, even once the rotor achieves Reynolds number independence.

Chapter 4

EVALUATION OF ELECTROMECHANICAL SYSTEMS DYNAMICALLY EMULATING A CANDIDATE HYDROKINETIC TURBINE

The text of the following chapter was published in the journal *IEEE Transactions on Sustainable Energy* in January, 2016. With the exception of reformatting the text, reducing redundant definitions and conclusions, including references to other chapters, and adjusting nomenclature to maintain consistency throughout this document, no changes were made to the content of the published version. The work was conducted primarily in Cork, Ireland while on a DOE EERE Postdoctoral Research Fellowship. The citation for the document is as follows:

Cavagnaro, R.J.; Neely, J.C.; Fay, F.-X.; Lopez Mendia, J.; Rea, J.A., "Evaluation of Electromechanical Systems Dynamically Emulating a Candidate Hydrokinetic Turbine," in Sustainable Energy, IEEE Transactions on, vol.7, no.1, pp.390-399, Jan. 2016 doi: 10.1109/TSTE.2015.2492943

4.1 Introduction

The high-energy aquatic environments in which hydrokinetic turbines will operate are such that extensive field testing of system prototypes, though necessary, is impractical and expensive. While prototypes are often designed to evaluate the hydrodynamic performance of device concepts such as the work of Chapter 2, electrical power take-off (PTO) components and control systems are often set aside until the final stages of development. Recent work has shown that these critical constituents cannot be developed in isolation from the rest of the system as they strongly influence the dynamics of the converter [2]. Indeed, this is clearly demonstrated in Chapter 3. Due to the difficulty of field testing, it is desirable to replicate the dynamics of a hydrokinetic turbine in a laboratory such that the fully integrated converter, including PTO and controls, may be developed and validated more easily. Such testing is useful for commercial entities developing hydrokinetic systems to demonstrate performance of their prototypes at technology readiness levels of 4 and 5 or stages 2 and 3 of the International Energy Agency Development guidelines [71, 58].

Electromechanical emulation machines (EEMs) used to emulate the dynamics of rotating bodies have been in service for wind energy research for many years. These machines are typically used to evaluate novel control strategies regulating performance of wind energy converters with nonspecific properties and outline how the dynamics of a turbine can be modeled and emulated with an electric machine [46, 54, 66, 43, 32, 63, 55]. Due to the similarity of the physics between wind and hydrokinetic energy conversion, wind turbine emulators have been used to evaluate control strategies for hydrokinetic turbines [9]. However, literature regarding how to translate the characteristics of a *specific* turbine operating in realistic conditions to the emulation framework is lacking; for example, thorough investigation of the effects of emulating a turbine with a high power rating on machines of significantly lower rating is untreated. Appropriate scaling of a turbine's power output and the resource driving the emulation is necessary to maintain an accurate link between a proposed full-scale turbine and its emulated equivalent.

This work demonstrates how a proposed hydrokinetic turbine can be emulated with the intent to mimic the conditions this turbine would encounter in the field as accurately as possible, including a grid connection and the use of realistic power take-off components and control strategies. The dynamic performance of the emulated turbine should thus ideally be repeatable and independent of the hardware the emulation is performed on. As every EEM is constructed of differently sized, controlled, and configured components, demonstrating the success of the emulation technique can be accomplished by performing dynamic emulation of the same proposed turbine on different EEMs. This 'round robin' style of investigation helps to validate laboratory techniques and machines and has the goal of improving the quality of prototype testing. Similar multi-facility evaluation through the Marinet program is ongoing [49]. Additionally, this work treats, compares, and discusses various scaling techniques that could be used to align the torque and speed (and thus, power) output of a proposed full-scale hydrokinetic turbine to what a laboratory scale EEM is capable of achieving, an aspect of PTO-integrated testing previously untreated in literature. These include hydrodynamic scaling techniques often used in the prototyping of systems that interact with flow. The applicability of two such methods is evaluated in terms of their utility for scaling the power output of a hydrokinetic turbine PTO as another original contribution. Finally, the emulation technique is compared to dynamic simulation of the same turbine under turbulent water flow conditions and maximum power point tracking (MPPT) control to highlight a typical use case and to show how emulation may differ from simulation.

Three laboratories have developed EEMs capable of emulating the dynamics of generic rotating prime movers, and consequently, are suitable to emulate hydrokinetic turbines: Sandia National Laboratories in the United States, Tecnalia in Spain, and MaREI-Beaufort in Ireland. Each emulator is designed for an end user to input a mathematical model of a wave, current, or wind converter, specify resource input conditions and a control algorithm or load, and produce detailed feedback from various sensors. In this work, the three EEMs are programmed to emulate the same hydrokinetic turbine - an openly-accessible reference model that was previously emulated on the Sandia emulator [7, 56].

Descriptions of the three EEMs are given in the next section. In Section 4.2.2, the hydrokinetic turbine reference model is presented. In Sections 4.2.2.3 and 4.2.3.1, the dynamic equations governing emulator control are developed, and different scaling techniques for conserving the system time constant, maintaining Froude similarity, and maintaining Reynolds number similarity are examined. Experimental and simulation results are reported in Section 4.3. Specifically, an initial experiment investigates the performance of the machines to determine if the effects of different generator types, power levels, control schemes, and grid connections across the EEMs affect general agreement in the dynamic response of the three

EEMs. Next, an effect of Froude scaling the turbine and resource is evaluated in hardware using the Tecnalia EEM. Finally, realistic input conditions and a relevant MPPT control algorithm are implemented on the MaREI-Beaufort machine to demonstrate a typical use case for the development of a PTO controller on an EEM. A discussion of the results is provided in Section 4.4 and conclusions are presented in Section 4.5. Chapter 5 presents a study utilizing many of the methods described herein to emulate a field-deployed riverine turbine.

4.2 Methods

4.2.1 Electromechanical Emulation Machines

The objective in the design of each of the three EEMs discussed was to create a platform to emulate the dynamics of power systems which include rotating or oscillatory motions. Each system is comprised of the same basic components: a motor and associated control electronics acting as the emulated system or prime-mover, a generator coupled to the motor with associated control electronics, an electrical load, and an array of sensors and monitoring components to measure mechanical and electrical quantities of interest. For loading, the generated electrical power is either dissipated in a resistive load or returned to the grid. For each machine, the prime-mover side was designed for an end user to provide a mathematical model of the system to be studied. Likewise, a user is able to specify a control law or parameters regarding loading on the generator side. The EEMs are built with different individual components, varying in capacity, inertia, and control methods. A general schematic of the EEM layout is shown in Fig. 4.1, and each emulator implementation is described in detail below. Relevant parameters for each EEM implementation are introduced and summarized in Section 4.2.2.3.

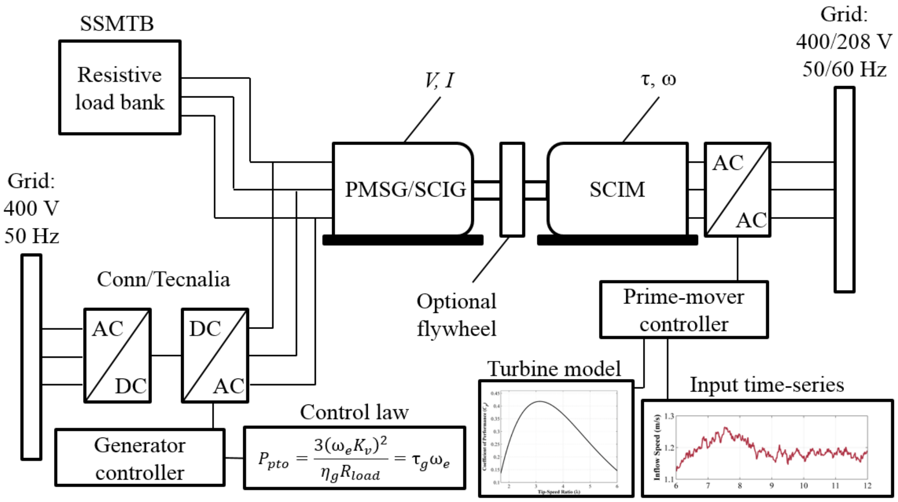

Figure 4.1: Schematic of EEM layout.

4.2.1.1 Sandia National Laboratories SSMTB EEM

Sandia National Lab's Secure Scalable Microgrid Testbed (SSMTB) EEM consists of a Baldor three-phase, four-pole variable speed 11.2 kW induction motor as a prime-mover coupled to a 10-kVA 28-pole Georator 36-013-1 permanent magnet synchronous generator (PMSG) rated for 1714 rpm [56]. The prime-mover is driven by a commercial ABB ACS800 motor drive which is capable of providing direct torque control (DTC). This system can realize a commanded torque in less than 5 ms and with less than 1% error when the system is properly calibrated and uses a speed encoder. This system does not include a flywheel or a torque sensor.

The emulator controls consist of a linear discrete-time generator torque estimator and a nonlinear torque calculation for the prime-mover. The controller and estimator are implemented on a National Instruments NI 3110 platform. The interface with the motor drive is developed in LabVIEW, and the NI 3110 communicates with the motor drive using Modbus/TCP protocol. The control and estimator equations are developed in Matlab and implemented on the NI 3110 using LabVIEW's Mathscript RT toolkit.

4.2.1.2 Tecnalia Electrical PTO Test Bed EEM

The prime mover of Tecnalia's electrical PTO Test Bed is composed of a 15 kW four-pole squirrel cage induction motor (SCIM) from Leroy-Somer rated at 1460 rpm and delta-connected 400 V / 50 Hz which allows peak power up to 28 kW, corresponding to a maximum speed of 3000 rpm. It is driven by a UMV4301 controller from the same manufacturer that follows torque and speed commands with a 5 ms response time. A real-time digital-to-analog board runs device numerical models programmed in a development computer controlling the motor. A flywheel of 1 kg m^2 is positioned on the shaft between the prime mover and generator. The inertia can be virtually increased up to 8 kg m^2. The PTO side is composed of an ABB 11 kW squirrel-cage induction generator rated at 768 rpm at 400 V and an ACS800 back-to-back power converter from ABB connected to an isolated grid and a resistive load bank. A PLC communicates with the controller via a serial interface and controls the converter by executing a state machine sequence which commands the initialization of the equipment, allows the operation of the device, handles errors and deals with survivability issues [79]. Actual power is produced during the normal operation state when control strategies such as a simple torque/speed proportional plus integral plus derivative (PID) controller or a more efficient and optimized control scheme are applied [20].

4.2.1.3 MaREI-Beaufort 'Conn' EEM

MaREI-Beaufort's 'Conn' EEM's prime-mover is a Leroy-Somer LSMV 180LU three-phase, four-pole variable speed 22 kW SCIM rated for 1467 rpm and includes a speed encoder. The motor is controlled with a Leroy-Somer Unidrive SP 33T 3404 PWM motor drive configured to allow for closed-loop speed or current control. The drive communicates with a Mitsubishi Q-Series programmable logic controller (PLC) and Melsec GXWorks2 software through a PROFIBUS interface. This configuration requires programming the drive in PLC structured text format which has limited high-level mathematical functionality. The back end of the motor shaft is coupled to a five-position gearbox and flywheel to allow variable inertia up to 8 kg m^2. The motor is coupled to the generator through a Kistler 4502A rotary torque sensor rated for 500 Nm.

The generator is a Leroy-Somer FLSB 225M three-phase, four-pole wound-rotor 22 kW induction generator with a rated speed of 1472 rpm. Access to the rotor windings is available through a slip ring. By altering the connections of the rotor windings, the generator can be configured to behave like different generator types [67]. The generator is optionally coupled directly to the grid operating at 400 V / 50 Hz, to the grid through back-to-back AC/DC drives in a regenerative mode, or connected to a resistive load bank to dissipate power as an isolated or islanded system. The generator is controlled in regenerative mode with a motor drive identical to the prime-mover side. The drive is operated with the same PLC interface, allowing user-specified control of the generator with either closed-loop speed or current control achieved with a PI controller internal to the drive.

4.2.2 Emulated System: US Department Of Energy Reference Model 2 Hydrokinetic Turbine

4.2.2.1 Turbine Description and Dynamic Model

The device chosen for validation of the EEMs was the US DOE RM2 hydrokinetic turbine [7]. The rotor is a three-bladed vertical-axis cross-flow fixed-pitch design rated for 50 kW at 2 m/s with a power extraction area of 31 m^2. The turbine's size and power output is small in comparison to megawatt-scale commercial utility prototypes, but is representative of the actual scale suitable for use in a riverine environment [7]. No generator type or grid connection is specified. A characteristic curve (Fig. 4.2) relating C_P and λ, defined in Chapter 1, was determined off-line in a turbine hydrodynamic simulator called CACTUS [7]. τ_h, the hydrodynamic torque, is a nonlinear function of λ and defined as in (1.8).

Turbine parameters designed to prevent cavitation and intended operation in channel flows at rated speed of 2 m/s result in a system with a low rotation rate. A gearbox of ratio N_b was added to proportionally increase speed and decrease torque at the generator. The velocity dynamic of the turbine was modeled with the first-order differential equation relating angular acceleration, equivalent moment of inertia, J_{eq}, from both the turbine (J_t) and PTO (J_{pto}), τ_h, parasitic torque present in the system as indicated by a damping coefficient, B_{eq}, and τ_c, the control torque applied to the turbine as a result of loading from the PTO (τ_{pto}),

$$\dot{\omega}_t = \frac{1}{J_{eq}}(\tau_h - B_{eq}\omega_t - \tau_c) \tag{4.1}$$

$$J_{eq} = J_t + N_b^2 J_{pto} \tag{4.2}$$

$$\tau_c = N_b \tau_{pto}. \tag{4.3}$$

Effective system damping is assumed to arise primarily from the gearbox as frictional losses from bearings are estimated to be low. The effects of added mass and the acceleration of fluid entrained by the turbine were considered higher-order constituents of the turbine dynamics and were not included in the model. Numerical values of designed turbine and estimated PTO parameters are presented in Table 4.1 [56].

4.2.2.2 Numerical Simulation

Numerical simulation of the reference turbine over a range of operating conditions was performed in the MATLAB/Simulink environment as a basis for the expected behavior of the turbine. An upstream velocity time series and initial rotation rate were required inputs to the model. At each time step, the simulation used the turbine performance curve, implemented as a 2-D lookup table taking ω_t and U_∞ as parameters, returning a value of τ_h from (1.8). A subsequent value for ω_t was computed from (4.1) using the ode45 numerical integration scheme for discrete time simulation with variable step size. For specifying the turbine control torque from the PTO, τ_c, was a model input and could be constant, based on a control law, or input as a time-series.

4.2.2.3 Scaling Considerations

As the EEMs considered have a lower rated power than the reference turbine, the system must be appropriately scaled. Two options for turbine emulation were considered: scaling

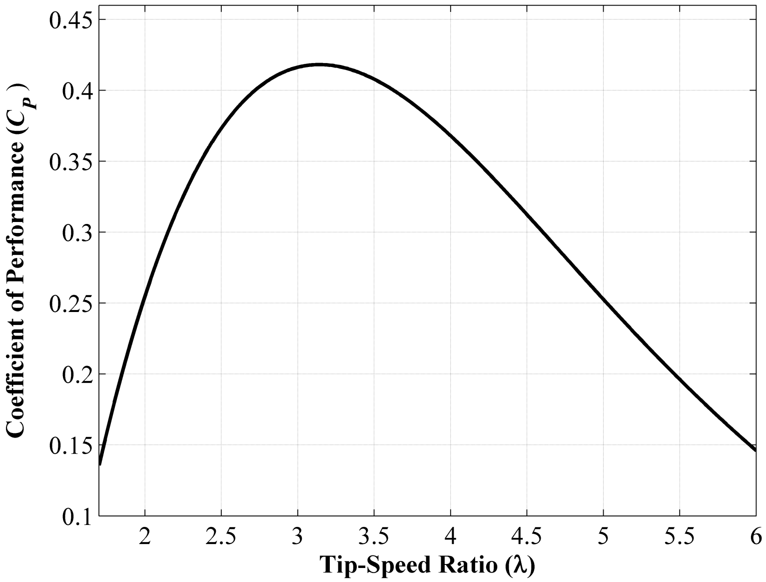

Figure 4.2: DOE RM2 characteristic performance curve.

to maintain the full-scale system time constant at the appropriate power level or scaling to maintain geometric and hydrodynamic similarity at the appropriate power level. The former method was accomplished by applying a scaling factor (γ) to each of the torque, damping, and inertia terms on the right hand side of (4.1). This method ensured that the time constant of the scaled turbine was identical to the full-scale version [56]. The value of γ was defined as the ratio of EEM rated power to turbine rated power,

$$\gamma = \frac{P_{em,rated}}{P_{t,rated}} \tag{4.4}$$

and, due to the above considerations, scaled down the emulated turbine torque, but maintained consistent rotation rate. From inspection of (1.8), utilizing the same performance curve and inflow velocity for the scaled turbine resulted in the scaling factor ultimately reducing the height of the rotor while maintaining its other characteristics.

Prototype MHK systems are often scaled to maintain both geometric similarity and aspects of hydrodynamic similarity to best represent relevant flow physics [87]. As an alternative to scaling with γ, relevant turbine and channel dimensions were scaled by a factor to

Table 4.1: DOE RM2 Turbine Parameters.

Parameter	**Value**	**Units**
r	3.23	m
A	31.22	m^2
$P_{t,rated}$	50.0	kW
J_t	6911	kg m^2
N_b	13.85	-
J_{pto}	7.80	kg m^2
B_{eq}	37.26	Nm s/rad

maintain geometric similarity (κ),

$$\kappa = \frac{r_{scale}}{r_{full}} \tag{4.5}$$

Hydrodynamic similarity can be achieved by maintaining a non-dimensional quantity of importance to fluid flow constant across both scales. Relevant quantities for the case of a hydrokinetic turbine were the Reynolds number (Re), an indication of the strength of inertial forces in the flow relative to viscous forces, and the Froude number (Fr), an indication of the strength of inertial forces in the flow relative to gravitational forces. These quantities were defined as

$$\mathrm{Re} = \frac{\rho U_\infty L}{\mu} \tag{4.6}$$

$$\mathrm{Fr} = \frac{U_\infty^2}{gh} \tag{4.7}$$

where L is a turbine characteristic length, μ the viscosity of water, h is the depth of the water channel in which the turbine operates, and g is acceleration due to gravity. Re and Fr similarity cannot be achieved simultaneously while also maintaining geometric similarity, as discussed in Chapter 1. Analysis of Re-scaling resulted in the conclusion that a perfectly scaled device would produce more power than a full-scale prototype. Re scaling for a physical prototype is often difficult to achieve due to the requirement of proportionally higher fluid flow rates. However, maintaining a similar Re across test scales may be important for maintaining properly proportioned hydrodynamic lift and thrust forces. In the case where similarity cannot be maintained, modifying the turbine geometry to perform similarly at lower Re is an option [87]. Additionally, it has been demonstrated that for certain turbine geometries, performance becomes independent of Re above a certain threshold [4]. Scaling by Re was not conducted for the analysis herein.

To achieve Fr similarity, experimental and turbine parameters were scaled according to the factors in Table 4.2 which can be derived by setting κ and matching quantities so that Fr remains constant. The value of κ for each EEM was determined by matching the final scaled value of rated power to that achieved through scaling with γ such that,

$$\kappa^{3.5} = \frac{P_{em,rated}}{P_{t,rated}} \tag{4.8}$$

Fr scaling allows for experimentation at a smaller scale under similar open channel hydrodynamic conditions. Assuming a full-scale channel depth of roughly twice the height of the rotor (≈10 m) and flow speeds between 0.7 m/s and 2 m/s, the range of Fr was 0.1 to 0.2. Power rating, inertia, damping coefficients and scale factors for each of the EEM implementations are summarized in Table 4.3.

4.2.3 Virtual Gearbox Application

The high torque and low speed characteristics of the reference turbine required additional manipulation for compatibility with the EEMs. This was accomplished through the application of a virtual gearbox so that,

$$\omega_e = N_v N_b \omega_t \tag{4.9}$$

$$\tau_g = \frac{\tau_c}{N_v N_b} \tag{4.10}$$

where ω_e is the rotation rate of the EEM, τ_g is the EEM generator torque, and N_v is the virtual gearbox ratio. N_v was set to a value of 5.91 to align the base speed of the SSMTB

EEM with the rated speed of the turbine PTO [56]. This ratio was maintained during testing on the other EEMs for ease of comparison. While the use of a virtual gearbox is an idealization, it is the result of attempting to emulate much larger, slower systems on conventionally sized, general purpose electromechanical machines.

Table 4.2: Scale Factors

Type	**Dimension**	**Parameter**	**Scale Factor**
Time constant scaling	*Length*	r	γ
	Inertia	J_{eq}	γ
	Torque	$\tau_h,\ \tau_c$	γ
	Power	$P_t,\ P_k$	γ
	Damping coeff.	B_{eq}	γ
Froude scaling	*Length*	r	κ
	Time	-	$\kappa^{0.5}$
	Inertia	J_{eq}	κ^5
	Torque	$\tau_h,\ \tau_c$	κ^4
	Flow velocity	U_∞	$\kappa^{0.5}$
	Power	$P_t,\ P_k$	$\kappa^{3.5}$
	Damping coeff.	B_{eq}	$\kappa^{4.5}$

4.2.3.1 Emulator Prime Mover and Generator Control

The prime-mover for each of the EEMs was an SCIM regulated with a PWM variable-speed motor drive. The SSMTB EEM drive utilized DTC; the Conn and Tecnalia drives each had the option of controlling motor speed or current as prescribed by an external controller. A method for prime-mover torque control was developed for use on the SSMTB using DTC

Table 4.3: EEM Parameters for Each System

Parameter	**Units**	**SSMTB**	**Tecnalia**	**Conn**
$P_{em,rated}$	kW	10.0	15.0	22.0
J_e	kg m^2	0.4005	1.2	1.25
B_e	N m s/rad	0.0174	0.0477	0.0775
γ	-	0.2	0.3	0.4
κ	-	0.6	0.7	0.8

and subsequently modified for use on the Conn and Tecnalia EEMs as a current control scheme using a custom current/torque calibration. The emulator torque command (τ_{em}) was determined using the dynamic equation for an EEM, with speed response defined as

$$\dot{\omega}_e = \frac{1}{J_e}(\tau_{em} - B_e\omega_e - \tau_g) \tag{4.11}$$

where J_e is the emulator's moment of inertia and B_e is the emulator's damping coefficient. By substituting (4.9) and (4.10) into (4.1) and (4.11), τ_{em} was solved for,

$$\tau_{em} = \frac{J_e}{J_{eq}}(N_v\tau_h - B_{eq}\omega_e - N_v^2N_b^2\tau_g) + \tau_g + B_e\omega_e \tag{4.12}$$

which represents the EEM's own torque requirement, plus an additional term to account for the emulated turbine's torque requirement at a higher inertia.

For the SSMTB EEM, a time-series of U_∞ values prescribed the model input. From these, τ_h was determined using (1.8) with C_P computed using a polynomial fit to the data obtained from CACTUS, τ_g was computed using an online estimator, and a torque command was computed using a discrete-time version of (4.12) and sent to the motor drive at each time step [56].

To investigate the performance of speed regulation, closed-loop speed controllers were implemented on the Conn and Tecnalia EEMs with the speed commands computed from (4.9).

For the Conn EEM, a discrete-time version of (4.1) was implemented in PLC structured text code with a tabulated version of the turbine performance curve. Linear interpolation was used to solve for τ_h from (1.8). As with the SSMTB, a time-series of U_∞ values prescribed the model input, and τ_g was obtained from the generator control function block. The Matlab/Simulink model of the turbine was implemented in real-time with the same inputs as the simulation for both speed and current/torque control of the Tecnalia rig.

As an initial test of the EEM dynamic response, the SSMTBs permanent magnet generator was connected to a three-phase resistive load (R) set to a constant value of 12.15 Ω per phase. A generator voltage constant (K_V) and efficiency (η_g) were computed using nameplate information to be 0.67 V s/rad and 0.93 respectively. The total expected PTO power (P_{pto}) was

$$P_{pto} = \frac{3(\omega_e K_V)^2}{\eta_g R} = \tau_g \omega_e \tag{4.13}$$

from which an expected generator torque was calculated. The EEM was programmed to emulate the reference turbine with time constant scaling to evaluate its dynamic response to a step change in inflow velocity from 0.85 m/s to 1.05 m/s. The same loading profile of (4.13) was subsequently used to specify τ_g for comparative testing on the Conn and Tecnalia EEMs to demonstrate the effects of different EEM size, layout, and control methods. The Conn and Tecnalia EEMs both employed induction generators connected to the grid through back-to-back inverter drives. The generator-side drive applied a current to the stator windings corresponding to the commanded torque based on calibration of the generator torque/current characteristics. Emulator speed and torque measurements (torque feedback was unavailable on the Tecnalia EEM) with prime-mover current/torque control were compared to results from simulation of the EEMs and from previously reported results of the SSMTB EEM [56]. The same stepped velocity test was then repeated on the Conn and Tecnalia machines using closed-loop speed control. Turbine parameters were scaled to maintain the full-scale time constant for these tests.

Differences in EEM behavior using time constant and Froude scaling were evaluated on the Tecnalia test rig. Tests were conducted with static velocity inputs ranging from 0.7 m/s to 1.1 m/s for the prime-mover under the PTO loading conditions of (4.13). Inputs and turbine parameters were scaled according to the factors in Table 4.2. Power output was measured at the emulated turbine rotation rate for each inflow speed. Dimensional power curves were created by modeling the turbine's expected power output over a range of R in (4.13) and scaling by γ and then κ for comparison.

Subsequently, to demonstrate a realistic use case, a MPPT nonlinear $K\omega^2$ control law, as in (1.14) was implemented on the Conn EEM. A velocity input time-series with simulated current-stream turbulence around a mean flow of 1.1 m/s with a 0.01 s resolution generated with turbulence simulator TurbSim was used to evaluate the performance of the EEM with MPPT control under realistic conditions [39]. Turbine parameters were scaled to maintain the full-scale time constant for this test.

4.3 Results

4.3.1 Evaluation of EEM Dynamic Capabilities

A comparison of the dynamic response to a step increase in velocity (rise in emulator speed) with the Conn and Tecnalia EEMs under current/torque control is presented in Figure 4.3. The rise and settle time series of the three emulators were compared to dynamic simulation results and those of emulation on the SSMTB. All three EEMs maintained the same virtual gearbox ratio and thus had the same target speed.

The Conn and SSMTB machines overshot the target steady-state speed by 6.6% and 1.5% respectively while the Tecnalia machine undershot by 0.2%. The 10%-90% rise times of the SSMTB, Tecnalia and Conn machines were 0.98 s, 1.10 s and 1.20 s respectively, while the rise time given by simulation was 1.43 s. The difference in EEM scale can be seen in the time series of prime-mover torque, which shows measurements from a torque sensor for the Conn machine and a torque estimate computed by the motor drive for the SSMTB EEM.

Under speed control, the Conn and Tecnalia emulators were able to closely track the target speed (Figure 4.4). In this mode, prime-mover torque was not determined by the turbine mathematical model but rather by the motor drive PI speed control loop. The Tecnalia and Conn EEMs both reached target speed within 0.1% with rise times of 1.35 s and 1.15 s, respectively. The dynamic and steady-state speed response of these EEMs were thus improved with speed control. Increased torque chatter observed in this mode from measurements on the Conn EEM is likely due to the aggressive proportional gain used to achieve fast tracking. The general agreement of the mean torque measurement with simulation indicated the turbine was being emulated correctly in this mode.

Each machine appears to follow the simulation, with the Conn EEM running at roughly twice the steady-state torque of the SSMTB, corresponding to doubling the scale factor and accounting for the higher damping and inertia of the Conn machine. The results suggest that both speed command and torque command modes are valid methods for turbine emulation. Speed regulation resulted in improved agreement with the simulated emulator speed but increased torque ripple on the Conn EEM. The SSMTB machine, which used DTC, demonstrated better agreement with simulation in torque response but greater error in the speed response. In general, the speed performance of the DTC-controlled emulator is likely to be more sensitive to parameter variation, i.e. variations in B_e. These performance trade-offs are intuitive and may be considered according to the experiment objectives.

Having compared the results of dynamic emulation for the Conn and Tecnalia EEMs against the SSMTB and simulation results, further experiments concerning EEM functionality were conducted on the Tecnalia and Conn machines using closed-loop speed control.

4.3.2 Comparison of Scaling Techniques

Dimensional power curves for the full-scale and scaled, emulated turbine on the Tecnalia test rig highlight the effects of the scaling methods (Figure 4.5). Time constant scaling maintained the shape and speed characteristics of the full scale turbine at smaller scale, reducing the magnitude of turbine torque. The selected loading profile from (4.13) resulted in emulation at rotation rate to the right of the MPP at each speed. Fr scaling the turbine

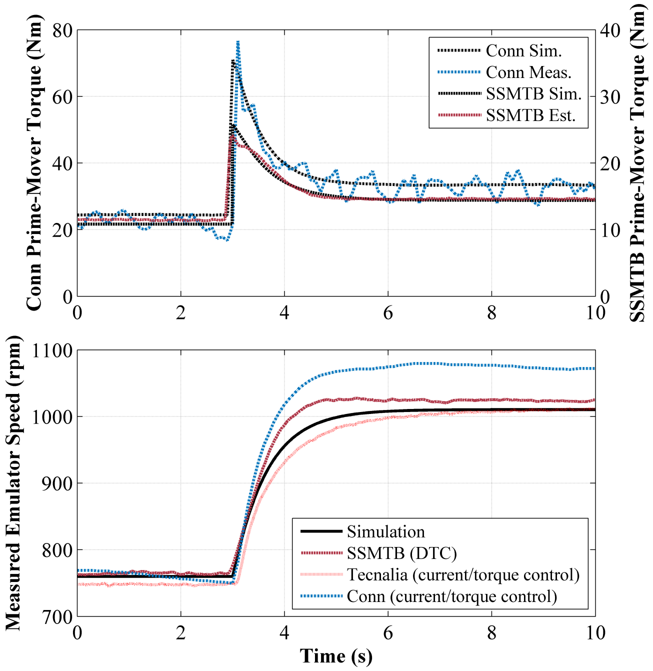

Figure 4.3: EEM response to step change in inflow velocity with loading of (4.13) Tecnalia / Conn EEMs using current/torque control.

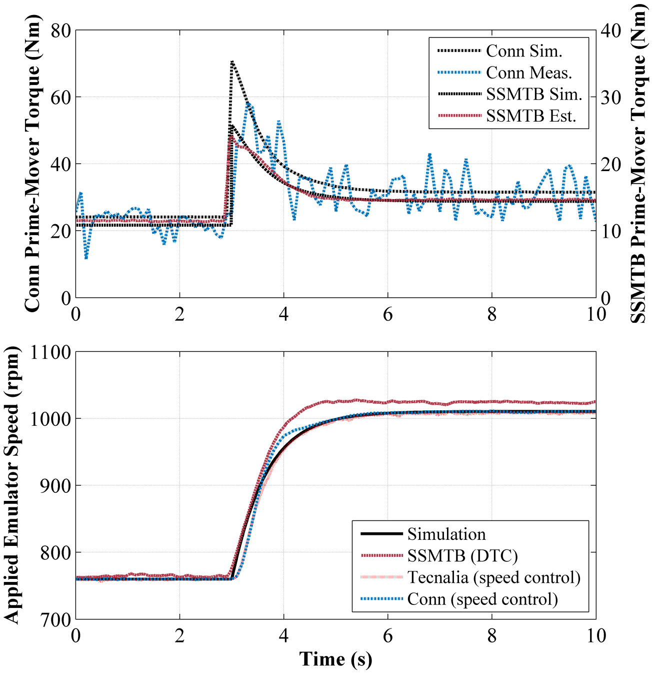

Figure 4.4: EEM response to step change in inflow velocity with loading of (4.13) Tecnalia / Conn EEMs using speed control.

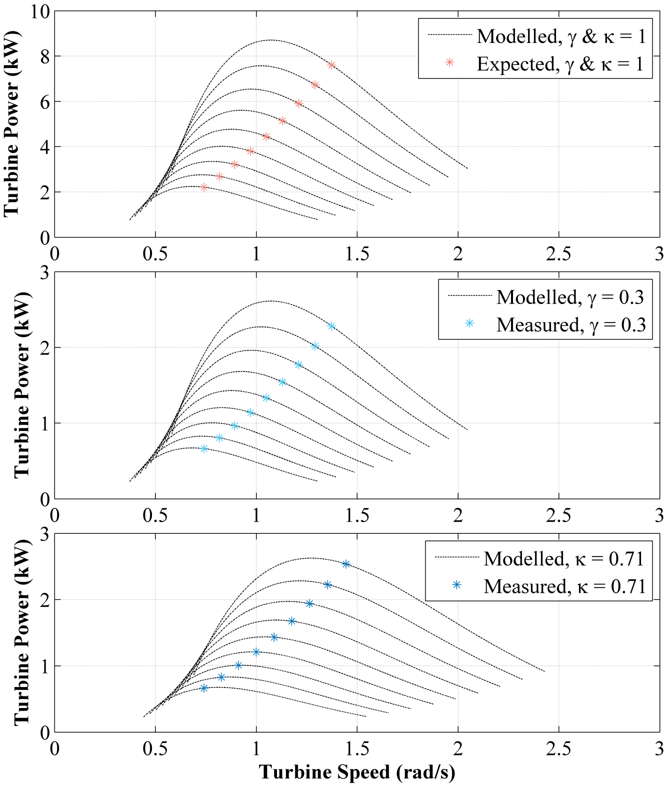

Figure 4.5: Power output of Tecnalia EEM under (4.13) with dimensional power curves for inflow of 0.70 m/s to 1.1 m/s: full-scale, time constant scaling, and Fr scaling, top to bottom.

resulted in power curves that were expanded and shifted towards higher rotation rates. Under the same loading conditions as the time constant scaled tests, the Tecnalia emulator rotated at equivalent turbine rates further to the left, closer to the MPP.

4.3.3 Emulation with Simulated Turbulence and MPPT Control

A 50 s turbulent inflow velocity time-series was used as the input for evaluating the effectiveness of testing control algorithms on the Conn EEM with time constant scaling. The MPPT control law of (1.14) was implemented to prescribe the torque load produced by the generator. The velocity input and equivalent emulated and simulated turbine speed (4.9) over a 6 s window are shown in Figure 4.6.

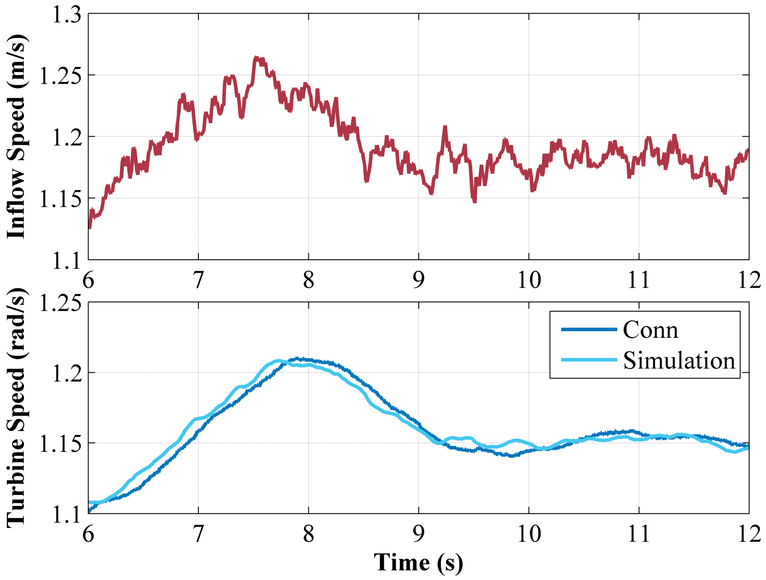

Figure 4.6: Simulated turbulent inflow and turbine speed response using (1.14).

The input included slow variations in the mean flow and faster, turbulent fluctuations. Both the simulation and emulation responded to the changes in mean flow by adjusting rotation rate accordingly. They were not sensitive to high-frequency turbulence due to the turbine's inertia. Closer inspection of the speeds shows a slight delay in response from the emulator. It also appears to have responded to fewer higher frequency changes in the inflow, on the order of 0.5 s. This is more apparent when the emulator and simulator responses are viewed in the frequency domain (Figure 4.7). A fast Fourier transform (FFT) of the input and resulting speed revealed that the emulator speed response contained less power between 1 Hz and 10 Hz than what would be expected from simulation. The emulator's response flattened out above 10 Hz, while the simulation continued to track the inflow fluctuations at these frequencies.

Real and reactive power delivered to the 400 V / 50 Hz grid connection point from the grid-side drive was measured during the MPPT control mode test. The grid-side drive was programmed to deliver power at unity power factor so the reactive power was zero VAr, as

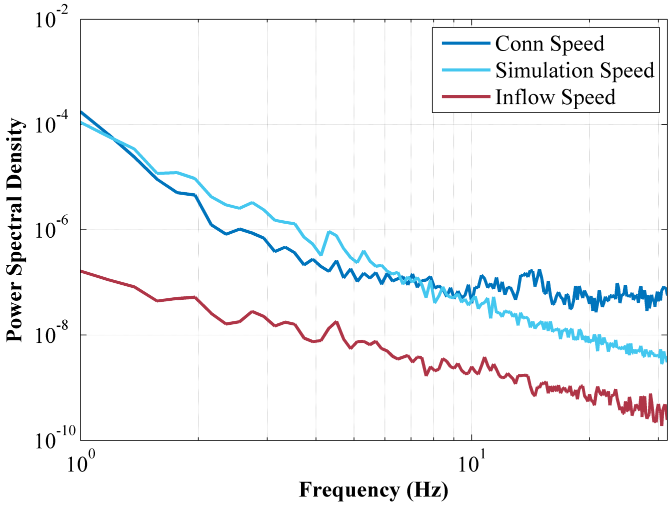

Figure 4.7: Power spectral density of turbine speed response using (1.14).

expected. Real power to the grid fluctuated by more than 100% over the 50 s window (Figure 4.8). These large fluctuations are expected, due to the cubic relationship between the water flow rate, U_∞, and the mechanical power available. Fluctuations of this proportion would be undesirable at larger power scales; though, multiple hydrokinetic devices, separated in space might have a smoother aggregate output [13].

4.4 Discussion

Different approaches to prime-mover control were investigated and included speed control and two variations of torque regulation. While DTC was available as a feature on the SSMTB drive, torque control for the Tecnalia and Conn machines required extremely accurate calibration to relate motor current and torque to achieve desired results. Even with calibration, slight perturbations in the torque on a machine caused deviation from the expected speed result. For the Tecnalia EEM operating in torque mode, the user had to specify a torque offset command for each individual test to track expected results. The closed-loop nature of the speed control subsequently implemented ensured the emulator speed response behaved as expected. Thus, for the Tecnalia and Conn EEMs, tuning the prime-mover drive PI

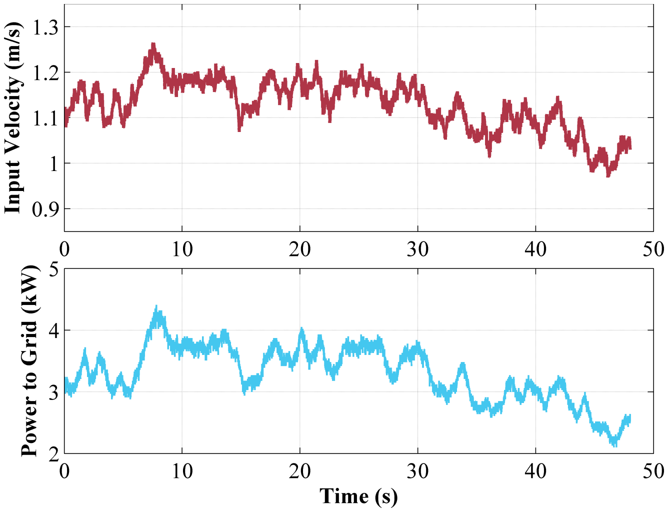

Figure 4.8: Simulated turbulent inflow and power exported to the grid using (1.14).

gains regulating speed control to tightly follow speed command proved less challenging than characterizing the motor torque/current relationships.

Two different scaling methods for electromechanical emulation of turbines are evaluated. Scaling to maintain Fr similarity ensures the turbine is tested under similar flow conditions between scales. This method results in a scaled turbine with a different time constant and fundamentally different behavior under similar loading constraints. The time constant scaling method results in emulating a turbine that would behave as the full-scale version but with a lower power output due to lower torque. However, this method assumes the full and scaled turbines have the same characteristic curve, a constraint that may be difficult to achieve in the implementation of a physical prototype.

The presently reported work compared emulation results of the proposed reference turbine to ideal dynamic simulation of the same turbine. The methods of this paper were utilized to reproduce the results of a physical hydrokinetic turbine operating in a turbulent riverine flow under loading similar to (4.13) with the Conn EEM (Chapter 5) [19].

The implementation and testing of multiple PTO control strategies on an EEM was demonstrated. The Conn emulator appeared less sensitive to high-frequency turbulence during operation at the MPP under turbulent inflow than simulation predicted. This is likely due to a combination of the EEM's finite response time, feedback control, reaching the noise floor of the various sensors, or high-frequency sensor noise, all of which would be present in a full-scale system. This drop-off in tracking of turbulence at high frequencies may not have consequences for grid interactions, but the analysis is useful in determining how a real turbine might react to such turbulence. This is a benefit of emulation over simulation. Additionally, the ability to evaluate aspects of power quality while exporting power to the grid is an important function the EEMs provide over simulation.

4.5 Conclusions

In this work, methods for emulating a candidate hydrokinetic turbine and PTO using laboratory-based motor-generator sets were developed and demonstrated in hardware. Specifically, the US DOE RM2 hydrokinetic turbine was emulated on three different EEMs of different topography and power level with strong agreement seen between the devices and results from simulation of the dynamic response to a step change in input. In addition, several technical issues were addressed in the text and investigated experimentally including: controller implementation, scaling, and emulator performance in a realistic scenario. It is concluded that if an appropriate mathematical model describing the turbine and emulator are used, different EEM rated power, size, and prime-mover control techniques may not affect the ability to achieve similar dynamic performance. It is concluded that two scaling methods may be appropriate for laboratory PTO testing depending on the goals of the experimentation; Fr scaling results in the evaluation of the PTO of a turbine operating under similar conditions of a prototype turbine one might build, while time constant scaling results in testing with properties similar to full-scale but not necessarily conforming to the constraints of geometric and hydrodynamic similarity. It is concluded that the ability to exercise different scaling methods for custom evaluation of PTO output is a useful feature of EEMs.

Finally, the implementation of PTO components and control hardware and software on industrial equipment at high power levels on an EEM closely parallels the same process undertaken for a field test of a prototype device. The ability to iterate and optimize this process confidently in the lab may be the greatest benefit of using EEMs in early stages of system development. This strategy is being put into practice during the development of a vessel-based field-scale turbine test platform at the time of publication of this dissertation.

Chapter 5

EMULATION OF A HYDROKINETIC TURBINE TO ASSESS CONTROL AND GRID INTEGRATION

The text of the following chapter was published in the peer-reviewed *Proceedings of the 11th European Wave and Tidal Energy Conference* in June, 2015. With the exception of the addition of a section containing updated results, reformatting the text, adjusting nomenclature to maintain consistency throughout this document, reducing redundant definitions, and including references to other chapters, no changes were made to the content of the published paper. The citation for the original document is as follows:

Cavagnaro, R. J., Polagye, B., Thomson, J., Fabien, B., Forbush, D., Kilcher, L., Donegan, J., McEntee, J. Emulation of a hydrokinetic turbine to assess control and grid integration, *Proceedings of the 11th European Wave and Tidal Energy Conference, (EWTEC 2015)*, Nantes, France. Sept. 6-11, 2015, p.10A3-4-1:8.

5.1 Introduction

Energy recovery from hydrokinetic sources may be an attractive option for remote communities adjacent to an appropriate resource. These communities often have weak electrical grids and lack advanced distribution capabilities [6]. Consequently, prior to installation, it is beneficial to understand how a hydrokinetic energy conversion system will perform and the effects of integrating it into existing grid infrastructure. Ocean Renewable Power Company (ORPC) is currently developing a horizontally-oriented helical cross-flow hydrokinetic turbine for use in riverine systems. The RivGen turbine (Figure 5.1) is rated to produce 17 kW of electrical power in mean currents of 2.3 m/s. ORPC is characterizing the performance of the turbine in the Kvichak River near Igiugig, Alaska (Figure 5.2), a site representative of a hydrokinetic resource suitable for electricity generation in terms of kinetic power density and isolated electricity demand.

Detailed knowledge of incident hydrokinetic current is necessary to accurately determine the efficiency of a turbine system [26]. Therefore, flow characterization measurements are made concurrent to turbine operation in the Kvichak River. Acoustic Doppler sensing techniques are used to measure variation in mean flow speed, turbulence content, and lateral (across-rotor) shear. This characterization, in addition to allowing a performance curve to be developed, can inform a statistical model of the flow that serves as a representative velocity time-series for simulation and emulation models of the turbine-river system.

As PTO components such as a gearbox and generator strongly influence the behavior of a turbine system, it is beneficial to evaluate the performance of the turbine with a PTO [2]. EEMs are hardware-in-the-loop systems capable of emulating the dynamics of rotating bodies in response to realistic input, include a full, controllable PTO, and are commonly used to evaluate wind energy systems [43]. Previous studies have extended the use of emulators to hydrokinetic turbines to evaluate control strategies, comparing results of emulation to dynamic simulation based on turbine properties [9, 83, 15]. The methods to do so are described in detail in Chapter 4. Additionally, an emulator has successfully matched the performance of a prototype turbine in a laboratory test scenario [34]. However, these studies have not compared results from the emulation technique to those of an actual field-deployed hydrokinetic turbine subject to realistic resource input.

The Conn EEM at MaREI-Beaufort in Cork, Ireland consists of a controllable motor, programmed to emulate the characteristics of a turbine, coupled to a generator. The generator is connected to back-to-back power converters enabling controllable variable-speed operation and integration with the local grid [67]. Details of the EEM's construction are provided in Chapter 4. This machine is herein configured to emulate the dynamics of the RivGen turbine based on performance and resource characterization determined by field trials. Electrical power produced during constant resistive loading in the field is compared to

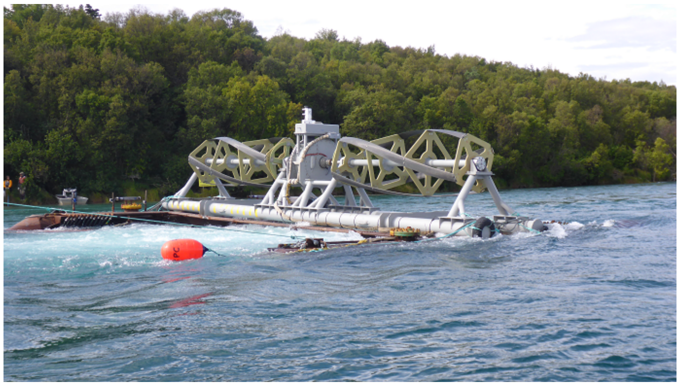

Figure 5.1: RivGen turbine generator unit prior to deployment in Kvichak River near Igiugig, Alaska.

that produced on the EEM under equivalent loads to validate the efficacy of emulation. Once verified, three control schemes intended to minimize the levelized cost of energy are implemented on the EEM to evaluate their performance. Additionally, a typical demand profile for the community of Igiugig is compared to the emulated turbine output to determine possible effects of turbine control strategies on the local grid. The turbine and EEM are briefly described in Section 5.2, in addition to a description of the methods of resource modeling and turbine emulation. Emulation results are presented in Section 5.3 and discussed in Section 5.4 before conclusions are stated in Section 5.5.

5.2 Methods

5.2.1 Turbine Description

ORPC's RivGen turbine consists of two 1.4 m diameter rotors of 4.1 m length bracketing a central generator. The 11.5 m^2 cross-sectional area (A) is centered approximately 3 m above the riverbed. The direct-drive permanent magnet generator output was rectified, transmitted to shore, and dissipated through a load bank of variable resistance (R) for field performance characterization ahead of grid integration. Electrical power (P_e) across the load

Figure 5.2: Kvichak River near Igiugig, Alaska with turbine site and coordinate system denoted.

was measured using a Shark 200 power meter on the DC input to the shore station. Expected P_e is related to R by the generator's voltage constant (K_V) of 513.6 V/rad/s and rotation rate (ω_t) inferred from voltage measurements as,

$$P_e = \frac{\omega_t^2 K_V^2}{R}. \tag{5.1}$$

The total system efficiency (η_s) is the fraction of incident kinetic power converted to electrical power,

$$\eta_s = \frac{P_e}{\frac{1}{2}\rho A U_\infty^3} \tag{5.2}$$

where ρ is the density of water and U_∞ is the reference inflow velocity. The turbine's mechanical conversion efficiency, or coefficient of performance (C_P) was estimated from field measurements of (5.2) with an assumption of the electrical efficiency of the generator and power conversion components (η_g) of 0.9 (based on generator characterization) such that,

$$C_P = \frac{\eta_s}{\eta_g}. \tag{5.3}$$

In [26], η_s was parameterized as a function of (λ). Applying the correction for estimated drive train efficiency yields the characteristic curve for the turbine, shown in Figure 5.3.

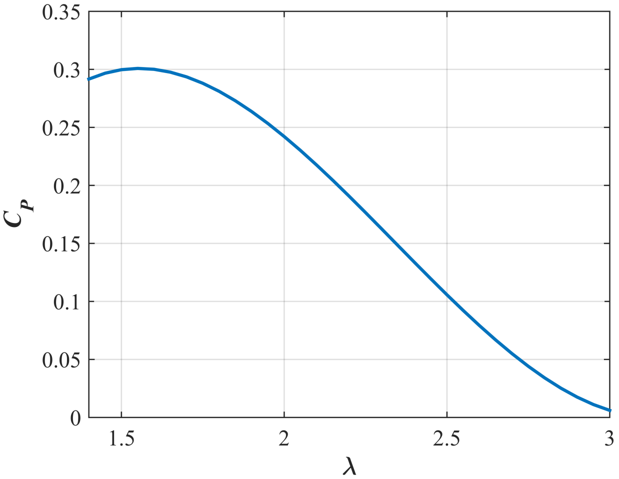

Figure 5.3: Estimated performance curve of the RivGen turbine as implemented in emulation assuming a 90% η_g.

5.2.2 Resource Characterization Modeling

Flow of the Kvichak River 60 m upstream of the turbine site was measured at high temporal resolution using an ADV attached to a sounding weight and manually deployed from a skiff. Motion of the ADV was synchronously recorded by an inertial motion unit and removed from the velocity measurement [41]. This measurement was used to specify input parameters for the National Renewable Energy Laboratory's PyTurbSim code. PyTurbSim is a turbulence simulation tool specifically tailored for generating resource time-series as input for hydrokinetic device simulation [40]. The software utilizes four statistical measurements of inflow: the mean velocity profile, TKE spectrum, Reynold's stress profile, and spatial coherence [40]. TKE from the field ADV measurements was determined and matched in the software output time-series. A mean velocity of 2.0 m/s, representative of average inflow velocity across the turbine rotor [26], was specified for the output over a spatial grid 10 m wide by 5 m deep. A logarithmic mean water velocity profile was specified with a uniform Reynold's stress over the spatial domain while the NWTC 'non-IEC' coherence model was used. A high degree of spatial variability in mean flow in the lateral direction observed in the field was not, however, captured [26]. A temporally representative time-series was generated for 300 s (0.0625 s time-step) of 'stationary' inflow. The grid location chosen for this time series was at turbine hub-height in the center of the channel.

5.2.3 Conn EEM and Emulation Technique

The 'prime-mover' of the Conn EEM (Figure 5.4) used to emulate the turbine is a programmable variable speed squirrel-cage induction motor rated for 20 kW. The motor drive can realize commands of current (converted to torque through calibration) or rotation rate with an internal PI loop. These commands are sent to the drive from a PLC executing a program emulating the RivGen turbine rotor mechanical power output. This program solves for ω_t numerically from an implementation of the first-order dynamic model of angular acceleration, defined as in previous chapters as,

$$\dot{\omega}_t = \frac{1}{J_{eq}}(\tau_h - B_{eq}\omega_t - \tau_c) \tag{5.4}$$

Values of J_{eq} and B_{eq} are estimated for the turbine as 246 kg m^2 and 10 Nm s/rad respectively. A value of τ_h is determined at each emulation time step based on the current value of the representative U_∞ at the turbine hub-height generated with PyTurbSim, and a value of $C_P(\lambda)$ corresponding to the emulated λ.

Though the prime-mover motor of the EEM is rated for a higher average power than the RivGen turbine system, transient instances from turbulent spikes in emulated velocity up to 2.7 m/s resulted in instantaneous power over 30 kW. These transients manifested in current spikes of 75 A, above acceptable limits for the motor drive and system wiring. This required emulating the turbine at a lower power level. Therefore, the turbine PTO output was scaled utilizing a method to preserve the system time constant (J_{eq}/B_{eq}), as discussed in Chapters 1 & 4, by a factor (γ) of 0.5. This scaling is achieved by multiplying the terms in the numerator and denominator of the right-hand side of (5.4) by γ, ultimately resulting in the emulation of a turbine with a reduced cross sectional area (and hence, power output)

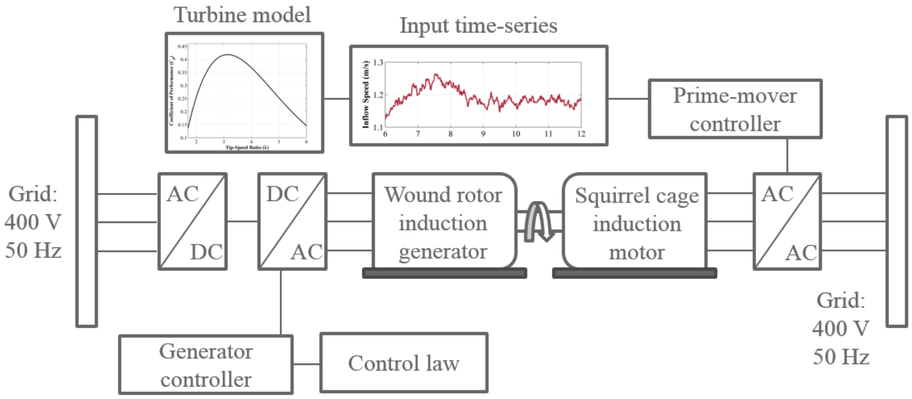

Figure 5.4: Schematic of Conn emulator layout.

by a factor of γ [56]. Additionally, a virtual 20:1 gearbox (gearing ratio N_v) was applied during emulation to align the low-speed, direct drive performance of the actual turbine with the high-speed characteristics of the EEM motor and generator. Utilizing this correction, commanded prime-mover speed (ω_e) during emulation became,

$$\omega_e = N_v \omega_t. \tag{5.5}$$

The PTO of the Conn EEM, as implemented for the testing herein, consisted of a wound rotor induction generator rated for 22 kW with its rotor windings shorted to function as a squirrel-cage induction generator. The generator's stator was connected to a series of programmable variable speed drives, the first regulating generator torque (τ_g), and the second maintaining output power at grid bus voltage and frequency. A PLC program was used to specify loading through the regulation of τ_g, which was similarly virtually geared and scaled as,

$$\tau_g = \frac{\gamma}{N_v} \tau_c \tag{5.6}$$

and relied on a calibration converting commanded torque to generator current demand. As with the prime-mover motor drive, an internal PI loop regulated generator current.

Available measurements from the EEM testing included ω_e from an encoder, τ_g from a rotary torque sensor, generator RMS phase-phase voltage and phase current, and real &

reactive power delivered to or supplied from the grid as reported by the grid-side variable speed drive. These parameters were recorded at 50 Hz.

Generator dynamic performance was evaluated by comparing the power output of the field turbine (sampled at 1 Hz) and emulated turbine output (sampled at 50 Hz) in the frequency domain. Actual turbine output under a 6.4 Ω measured resistive load was scaled by γ to match the power level of the emulator under the same load. Linear trends were subtracted from both time-series, which were split into 64 s windows before processing with a fast Fourier transform. The windowed spectra were averaged to create single power spectral density (PSD) series for each signal. Total variance in output was computed as the integral of PSD over the frequency band analyzed.

5.2.4 Generator Control Schemes

Four schemes for determining τ_g were implemented to validate the emulation technique against results from field testing, and to evaluate the resulting C_P and η_s over a 300 s turbulent input flow. Validation testing was conducted by emulating P_e as if the EEM generator was connected to purely resistive load as in (5.1). Utilizing (5.5) and (5.6), the resulting torque commanded was,

$$\tau_g = \frac{\gamma}{N_V \eta_g} \frac{\omega_t K_v^2}{R} \tag{5.7}$$

in which the value of R matched field testing measured resistances of 12.5 Ω, 10.4 Ω, 8.8 Ω, 7.6 Ω, 6.4 Ω, and 5.2 Ω. Successful emulation was achieved if output power delivered to the grid under the same load and similar inflow conditions matched power produced by the turbine in field, scaled by γ. Power factor during emulation was maintained at 1.0 to match the purely resistive loads present during field testing.

Two PI controllers were implemented in emulation to maintain a constant, optimal value of λ^* and a constant ω_t^* equal to the optimal ω_t corresponding to the mean flow speed of the 300 s input time-series, respectively. Controller action was conducted at a 10 Hz update rate, and proportional (K_P) and integral (K_I) gains were tuned empirically to achieve a balance between tight tracking of λ^* or ω_t^* and overshooting. The rotation rate and TSR PI controllers were formulated as in 1.12 & 1.13 (Chapter 1). The integral term was computed numerically in the controller PLC program.

Furthermore, a nonlinear controller specifying an optimal torque command was implemented. This MPPT controller specified a control torque based on the square of ω_t and a gain (K) based on the turbine's parameters and optimal operating point. In emulation, this resulted in a torque command of,

$$\tau_g = K\omega_t^2 = \frac{\gamma}{N_v}(\frac{1}{2}\rho A r^3 \frac{C_{Pmax}}{\lambda^{*3}})\omega_t^2 \tag{5.8}$$

where λ^* is the tip-speed ratio corresponding to the turbine's maximum C_P.

5.2.5 Isolated Grid Demand

Active and reactive power demand and average grid frequency were recorded for the community of Igiugig to investigate its grid dynamics. Demand in kVA, power factor, and average frequency in Hz were measured at a 1 Hz sampling rate for the duration of the RivGen turbine deployment. This data was monitored on ORPC's SCADA system, and was logged in a database. The grid consisted of two diesel generators rated at 50 kVA. Trends in the frequency domain of the load were compared to the field and emulated generators by normalizing the load and power outputs by their respective means and utilizing the same methods as 5.2.3. Active power demand was only considered for this analysis.

5.3 Results

5.3.1 Velocity Time Series

A single velocity time series (Figure 5.5) generated with PyTurbSim from statistical measurements of turbulence made during field trials was used as the input for subsequent emulation (mean velocity of 2.0 m/s). The turbulence intensity is 10.7% and the time series contains a maximum speed of 2.67 m/s and a minimum speed of 1.23 m/s (11 s apart in the time-series).

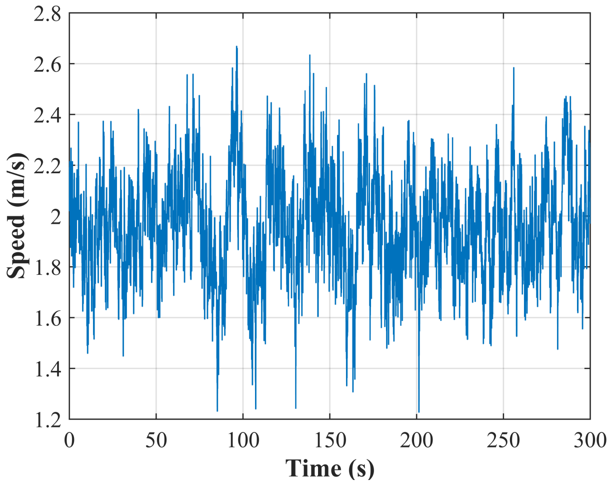

Figure 5.5: Water velocity input time series used for emulation.

5.3.2 Comparison of Field and Emulated Performance - Constant Resistive Loading

Active power output during field testing of the RivGen turbine under steady, purely resistive loads was measured for ≈120 s and averaged. P_e scaled by γ is compared to the real power generated under equivalent loading according to (5.7) during emulation (Figure 5.6). Agreement between scaled field and emulated power ranged from 3% difference at the highest power test to 15% at a lower power. Difference in results is attributed to electrical losses relative to output power which are expected to be higher for lower power tests, as these represent a small fraction of the EEM hardware's rated power of 22 kW. Subsequent controller implementations maintain power output near the higher end of the range, where the emulation matches field results. Additionally, some difference may be ascribed to uncertainty in the measurement of the actual turbine load resistance.

5.3.3 Emulated Controller Performance

Constant λ, constant ω_t, and $K\omega_t^2$ controllers were implemented in emulation to regulate the turbine in response to time-varying inflow conditions. Each controller's effect on emulated

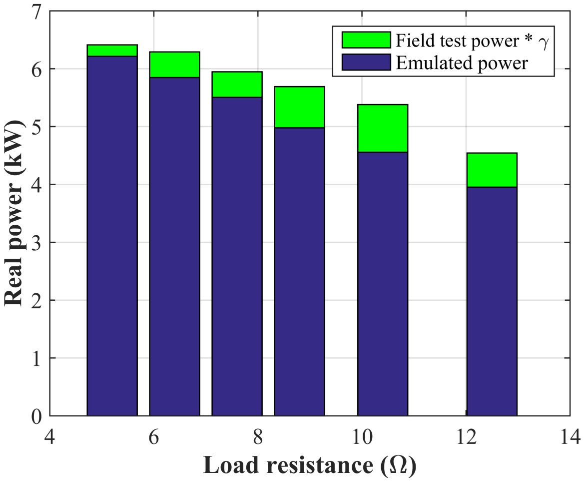

Figure 5.6: Resistive loading field and emulation comparison.

turbine ω_t (from (5.5)) is shown in Figure 5.7. Both constant λ and $K\omega_t^2$ are variable speed controllers attempting to track the optimal performance point of the turbine, and thus regulate speed to the same setpoint. The constant λ controller, however, overshoots and undershoots the optimal point, a symptom of linear control. Constant ω_t control action is clearly seen, as the emulated turbine remains close to the same rotation rate ± 2.5 rpm.

Mean emulated turbine C_P as computed by the PLC-based prime-mover control program was slightly higher for the $K\omega_t^2$ controller at 0.298, followed by the constant λ and constant ω_t controllers at 0.295 and 0.293. Hence, there was no significant difference in emulated mechanical efficiency over the 300 s tests. Instantaneous C_P (Figure 5.8) dropped momentarily for the constant ω_t controller during times when the flow speed differed substantially from the mean, corresponding to low frequency, large turbulent fluctuations. Real power delivered to the grid (Figure 5.9) exhibited a high degree of similarity for the three controllers. This resulted in nearly identical η_s for each case, with the $K\omega_t^2$ controller resulting in a mean efficiency of 0.287, and the constant λ and constant ω_t at 0.280 and 0.284 respectively. The higher system efficiency of the constant ω_t controller is attributed to the EEM's generator operating at a slightly higher electrical efficiency under constant speed operation. Instan-

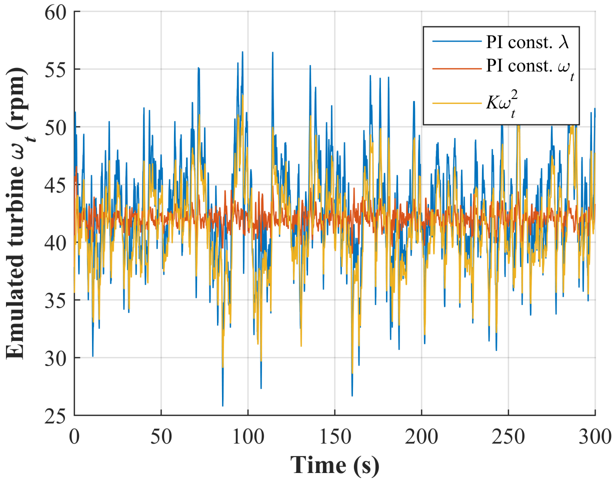

Figure 5.7: Emulated turbine speed under control action.

taneous values of η_s (Figure 5.10) exceed the maximum C_P of the turbine (0.30). This is thought to be due to a combination of measurement noise, imperfect calibration between commanded τ_g and realized generator current, and imperfect tracking of ω_e during emulation.

Peak PTO torque for the emulation tests under the three controllers varied from 135 Nm for the $K\omega_t^2$ scheme to 143 Nm and 150 Nm for the PI λ and ω_t schemes with standard deviations of 15 Nm, 20 Nm, and 22 Nm, respectively. This result indicates the nonlinear controller loads the PTO to a lesser degree by making fewer severe corrections to maintain a setpoint. Conversely, the constant ω_t controller must make the most severe corrections to maintain constant speed in response to large changes in inflow velocity.

Active controller performance is compared to 'passive' control performance with emulated constant resistive load from (5.7). Under a loading equivalent to 5.2 Ω, mean turbine C_P was 0.295 with a mean η_s of 0.279. Performance was therefore nearly identical to the active controllers over the 300 s test. PTO loading with this control scheme was less severe, with a peak torque of 104 Nm and standard deviation of 10 Nm. This result is expected, as no corrective action is taken to maintain a setpoint.

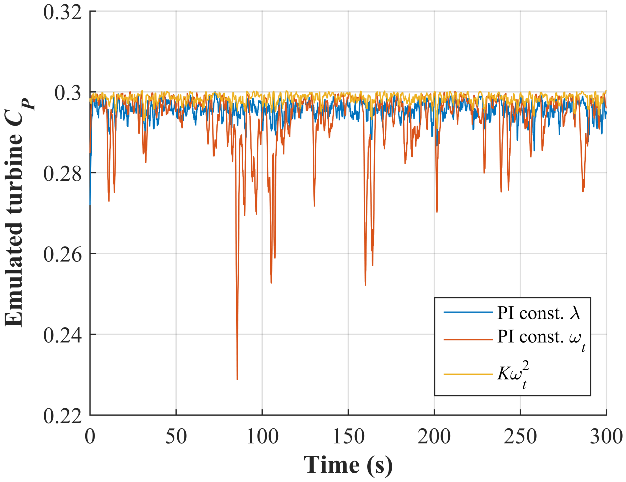

Figure 5.8: Instantaneous emulated C_P with 1 s moving average smoothing.

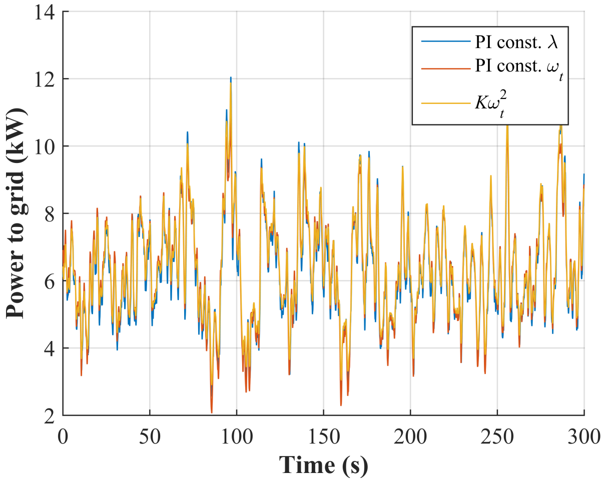

Figure 5.9: Real power delivered to grid with 1 s moving average smoothing.

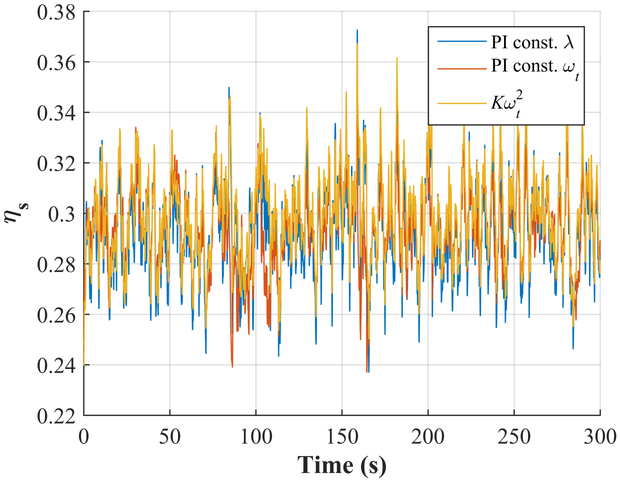

Figure 5.10: Instantaneous system efficiency with 1 s moving average smoothing.

5.3.4 Comparison of Field and Emulated Dynamic Performance

Power spectra for scaled, field turbine power and emulated power under similar loading conditions are plotted on the same axes (Figure 5.11). Though exhibiting a similar trend, emulated turbine output was more variable than field turbine output. Total variance for the turbine was 0.18 kW^2 compared to 1.9 kW^2 for the emulated output. This is thought to be caused by the physical turbine reacting only to turbulent length scales on the order of magnitude of its dimensions (an engulfing gust), and being insensitive to higher frequency turbulence. The turbine's largest dimension is its span-wise length (8.2 m), over which the turbulence and mean flow were substantially variable, thus the turbine may only be reacting to fluctuations of 0.25 Hz or slower assuming an average velocity of 2.0 m/s across the rotor span. The presence and action of internal motor and generator control loops regulating speed and torque may also contribute to the difference.

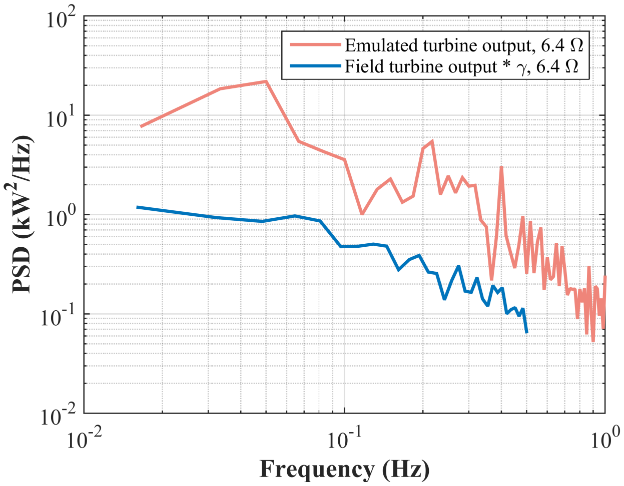

Figure 5.11: Dynamic performance comparison between field-tested and emulated real power output.

5.3.5 Grid Integration Considerations

Real power demand for the town of Igiugig during August 1, 2014 (Figure 5.12(a)) was analyzed to determine the implications of integrating a RivGen turbine into the grid. Demand exhibited a slow trend throughout the day, with mean power remaining stationary on the order of tens of minutes. During the day, there was a high load (neglecting outlying spikes) of 57 kW and a low of 26 kW. A 300 s portion of the time-series (Figure 5.12(b)) at a power level near the low point of demand was selected to match the time scale of the emulated power output testing of the turbine. The demand in this time-frame remained relatively stable on the order of seconds between instantaneous decreases and increases, as loads were switched off and on.

The turbine's emulated output scaled by $1/\gamma$ under a 6.4 Ω resistive load was compared to Igiugig's demand (Figure 5.13) as if the demand profile of Figure 5.12(b) occurred simultaneously with the input profile of Figure 5.5. In these conditions a single RivGen turbine would not be able to meet the demand of the town, while two turbines could produce more

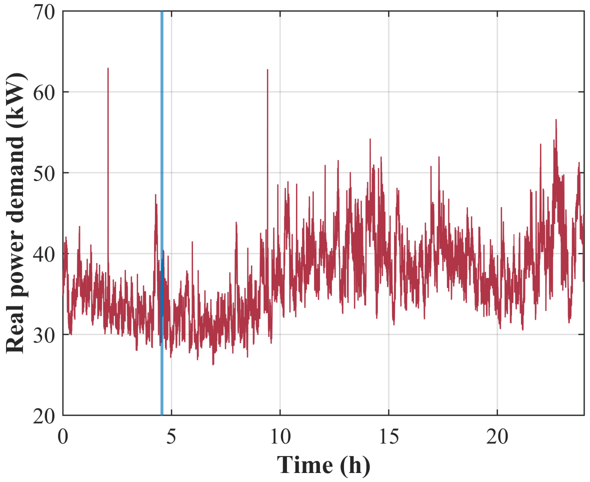

(a) Full day grid demand.

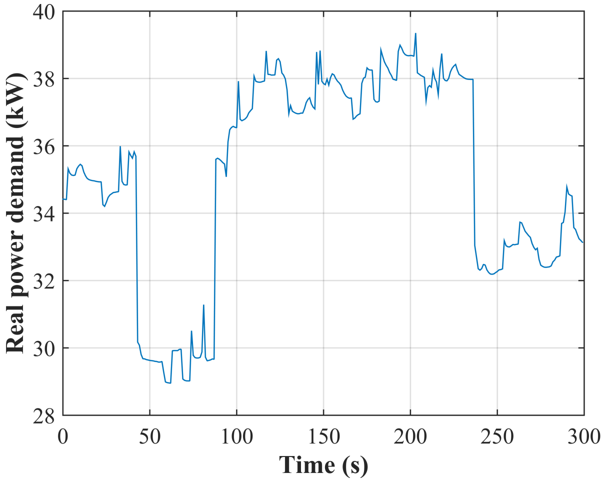

(b) 300 s grid demand, shaded area in (a).

Figure 5.12: Real power demand for Igiugig, 1 Hz sample rate, August 1, 2014.

power than needed at times. For the former case, an additional power source would be necessary for the demand to be met. For the latter case, a control strategy limiting power output or the ability to store energy produced in excess of demand would be needed.

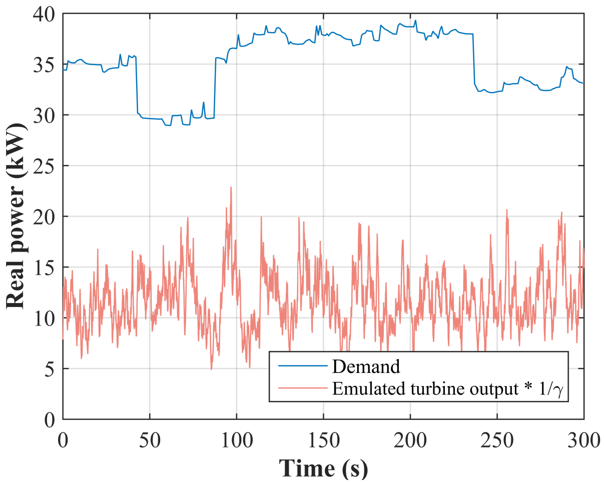

Figure 5.13: Grid demand and emulated turbine output.

Power output from the turbine appears to change at a rate much faster than demand, as the inertia of the turbine is low, allowing it to react to short time-scale fluctuations in velocity. This is quantified by viewing the emulated power demand and turbine output in the frequency domain. These are compared with actual power output near optimal performance of the field-tested turbine on the same axes in Figure 5.14. The turbine is expected to produce power more uniformly over a wider band of frequencies than would be required by the grid; the turbine's inertia is lower than the grid's, as evidenced by the steeper drop-off in frequency response. Therefore, should the turbine be incapable of meeting the full demand, a secondary source of power with a similar dynamic response would be needed to balance the high-frequency variability of the turbine output.

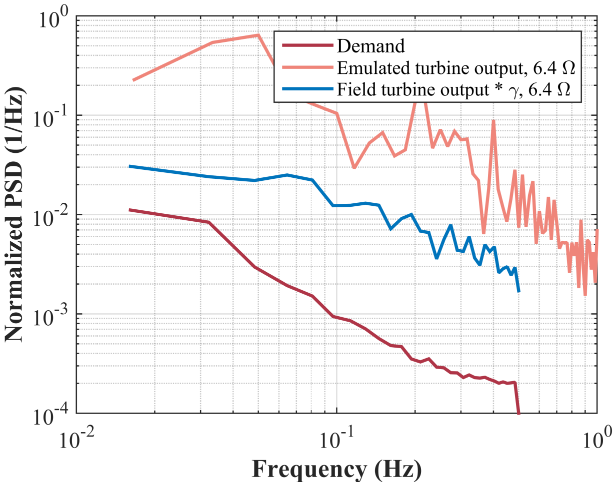

Figure 5.14: Grid demand and emulated and field turbine output normalized PSD.

5.4 Discussion

High-resolution measurements of free-stream river velocity were used to seed synthetic turbulence generation software. Agreement between temporal flow statistics suggests the output of the program can be used as the resource input for simulation and emulation of a hydrokinetic turbine. One benefit of using such software is the ability to create a large number of representative time-series based on a limited number of field measurements. Parameters are randomly seeded in the software such that unique time series with similar statistical characteristics can be created. Additionally, the software's output does not include contamination from sensor motion and Doppler noise, common concerns when utilizing acoustic techniques for flow characterization, but does not preserve all of the real flow information [68]. Finally, the software allows the creation of a spatially-gridded flow field, something difficult to obtain in the field.

Average electromechanical emulated power output is shown to agree with scaled field measurements of power output under similar inflow and loading conditions. Previous studies have compared results of emulation to hypothetical turbines and dynamic simulation [15, 56].

Emulation occurred at a lower power level than the actual turbine and with the inclusion of a virtual gearbox. Evaluation of the dynamic performance of the emulated turbine indicates a similarly trending, but higher variance response between 0.02 Hz and 0.5 Hz relative to that of the field turbine. The application of a virtual gearbox is the result of the high-torque/low-speed characteristics of the RivGen turbine being emulated on industry-standard electrical machines rated for low torque and high speed.

All evaluated turbine control strategies perform similarly in emulation given the input velocity time-series utilized for testing. This implies that, with a resource that is turbulent but whose mean does not vary substantially on the order of minutes, an aggressive controller tracking fluctuations in speed at a high frequency may not be necessary to achieve high average efficiency. This is evidenced by the strong performance of 'passive' control, where the loading was set to a static value that corresponded to an operating point near optimal for the mean flow speed. The results suggest a simple controller whose parameters vary on the order of minutes may be suitable. As these results are preliminary, future work will explore the role of control action update rate in obtaining desired performance.

A method was employed which scaled turbine parameters for emulation such that the emulator put out power at 50% of that developed in the field. This method assumed the rotor would behave in the same manner (i.e., perform with the same characteristic curve of Figure 5.3) despite having half the length. The validity of this assumption was bolstered after field trials of the RivGen turbine conducted in the summer of 2015. During operation, conditions allowed for testing with one of the rotors decoupled from the power shaft. Electrical efficiency was measured under similar conditions with both the single and double rotor configurations (Figure 5.15). Strong agreement of the curves indicates, at least during steady operation, reducing the length of the rotor proportionally reduced the power output of the turbine, while maintaining its relationship between efficiency and speed.

The greatest benefits of the emulation technique are the ability to investigate various control strategies and the ability to evaluate actual power delivered to the grid in a laboratory environment. Determination of the viability of control techniques at low cost in the lab is

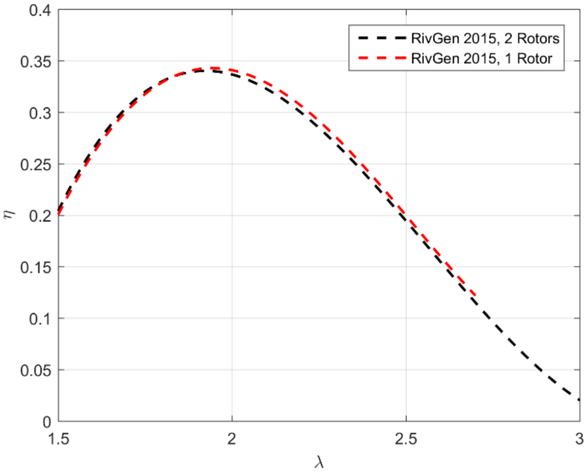

Figure 5.15: Performance of the RivGen turbine with one and two rotors (2015).

preferred to exploratory testing during costly field operations.

Comparison of the turbine's actual and emulated output with the demand of the community near where it may be deployed yields information on how grid integration may occur. The characteristics of a second generation source can be inferred based on the need to balance the turbine's variable output at high frequency under control with the strategies investigated. For example, if two turbine systems are utilized to meet the demand, one may need to employ a control strategy that tracks grid load, rather than maximizing power generation.

5.5 Conclusions

A representative resource model is taken as an input for laboratory emulation of a hydrokinetic turbine. A controllable motor is programmed to mimic the dynamics of the turbine as characterized in the field. Scaled power output during turbine emulation is in agreement with field trials under similar resource and resistive loading conditions, supporting the emulation technique. Nonlinear $K\omega_t^2$ and linear PI constant λ and ω_t control strategies are implemented in emulation. These controllers exhibit similarly efficient performance and maintain power output at near optimal values over a 300 s trial. The dynamic response of the emulated turbine is compared to the field turbine and is found to have a larger response to turbulent inflow, resulting in more variable instantaneous power output fluctuation. The turbine response is also compared to that of the grid of a small community near a potential turbine deployment site. The turbine's inertia is lower than the grid's, necessitating a secondary power source with a high-frequency response to meet power demand in the event the turbine's output cannot meet it alone. The electromechanical emulation technique is shown to be valuable for investigating control strategies and grid integration for a hydrokinetic turbine in a laboratory setting at a lower cost than field trials.

Chapter 6

CONCLUSIONS

A set of analysis, testing, and emulation techniques for the evaluation of cross-flow hydrokinetic turbines are developed, each relying and building upon dynamic modeling and characterization methods. This represents a progression from prototype scaling to stability analysis to full system characterization, and ultimately results in an emulation technique with the demonstrated capability of replicating the power output of a fielded turbine. The analysis, methods, and results are intended to advance the understanding of prototype and medium (field)-scale turbine systems including power take-off and provide a road map for the development of more advanced controllers, all potentially leading to more cost effective development.

6.1 Cross-Flow Turbine Dynamics and Scaling

The constituents of a turbine's dynamic equation of motion are explored to determine contributions to turbine behavior. Moment of inertia is shown to control the bandwidth of frequencies a turbine is capable of reacting to, while damping is shown to influence the magnitude of reaction to a disturbance or control action across all frequency bands it is capable of reacting to. The ratio of the two properties is a mechanical time constant that can be used to determine if a turbine only reacts to large frequency disturbances (inertia-dominated) or a wider range of frequencies, but with a lower magnitude reaction (damping-dominated). A field-scale cross-flow turbine is shown to be most reactive to the most energetic and largest turbulent structures present in a typical tidal current flow. Limits of stability, determined through a linearizion of the turbine dynamic equation, are shown to depend on the magnitude and frequency of turbulent decreases in flow speed, as well as initial operating point and resistance to rotation.

Several scaling techniques intended to allow certain aspects of a prototype turbine to become representative of a full-scale turbine are described and discussed. Linear geometric scaling of a turbine results in a model with highly nonlinearly scaled dynamic properties, such as mechanical time constant. Reynolds scaling may not be achievable in prototype testing due to a requirement of high-speed flow. Additionally, a fully Reynolds-scaled model would be expected to output more power than a full-scale version. Froude scaling for laboratory testing may ensure the properties of the resource are similar to full scale, but turbine performance may not match full-scale due to significantly decreased Reynolds number. Time-constant scaling preserves the dynamic properties of a full-scale turbine at small scale, but assumes its performance curve is maintained through scaling. No scaling method should be expected to match all properties between the prototype and full-scale turbine.

6.2 Cross-Flow Turbine System Stall

System stall occurring at a critical tip-speed ratio (that corresponding to the maximum torque point) is shown through analysis of static decreases in inflow. An experiment characterizing the stability of a cross-flow turbine and the conditions under which it experiences system stall (complete loss of ability to rotate) is described. A classification algorithm is successful at identifying a number of distinct regions in time series of rotation rate during stall events, and is useful for creating a consistent criteria for defining the amount of time the turbine is able to maintain stable operation at a critical tip-speed ratio. Both acoustic and laser visualization methods are utilized to monitor upstream flow during system stall experiments, and agreement is generally good between them; both data sources show some correlation of turbine operation to fluctuations in inflow speed, but definitive flow events are not identified as inducing system stall. Frequency domain analysis of the flow reveals less turbulent kinetic energy in the seconds leading up to the identified system stall point than otherwise. This, along with analysis of the turbine's responsiveness to turbulence present in the flow, indicates the conditions under which the turbine will stall are developed over time on the scale of seconds, at least for cases where the turbine does not stall immediately. Further investigation into inter-rotational dynamics of cross-flow turbines is required to identify distinct precursors or events that definitively bring about system stall once the above conditions are met.

6.3 Cross-Flow Turbine Performance Evaluation

A method for testing a field-scale turbine in the absence of the confounding factors of blockage and low Reynolds number operation is detailed. A mechanical performance curve for the turbine is created utilizing two sets of measurements: direct mechanical power and electrical power produced through a generator. Efficiencies of each system component are determined and used to infer mechanical efficiency from electrical measurements. The dynamometry technique used to develop component efficiencies is equivalent to electromechanical emulation of the steady-state operation of the turbine. A generator is shown to strongly influence the dynamics and overall system efficiency, highlighting the need for properly-specified PTO components. Using steady-state turbine emulation and a PTO, only a subset of measurements are required to characterize a fielded turbine: the speed of the resource and rotation rate of the turbine under a known electrical load.

6.4 Cross-Flow Turbine Dynamic Emulation

A hypothetical field-scale turbine's parameters are scaled to match the power output of three electromechanical emulation machines (EEMs) used to dynamically simulate rotating systems. Each EEM consists of a different motor-generator set where the motor is programmed to behave as if it were the turbine reacting to dynamic inflow conditions. EEM generators coupled to the motors produce power and export it to the grid or dissipate it with a resistive load bank. Under time-constant scaling, all three EEMs exhibit similar dynamic performance in terms of matching the turbine's expected speed response to a step change in inflow speed. A maximum power-point tracking controller is implemented in emulation to demonstrate a realistic use case. The Emulator is shown to be less responsive to turbulent inflow than expected from simulation due to the presence of internal control loops and operation near the noise floor of sensors.

The same emulation technique is used to evaluate a range of controllers acting on a commercial field-scale turbine. Agreement is seen between actual and emulated power output under resistive loading. Optimal nonlinear torque and linear speed controllers are able to maintain near-peak performance under inflow conditions based on measurements from the river where the field turbine was deployed. When viewed in the frequency domain, emulated power output contains more high-frequency content than the field turbine's output. This is contrary to comparison with simulation of the turbine, and attributed to the horizontal orientation of the field turbine across a river with a lateral shear feature; the field turbine may only be responsive to turbulent structures on the order of its largest dimension; the turbulence acting at any point on the rotor will be out of phase with other points until a critical scale is reached. The implementation of controllers in emulation is meant to closely mimic implementation in the field, but at a lower cost and easier ability to iterate.

6.5 Future Work

Future work of interest related to the topics of this dissertation that may be pursued as a postdoctoral researcher or suggested to future researchers are briefly described.

6.5.1 Evaluation of Cross-Flow Turbines Utilizing a Lab-based PTO Test Setup and Vessel-Based Field Turbine Platform

An ongoing project with the broad objective of advancing development of hydrokinetic energy conversion including current stream and wave technology is currently underway, with funding from Naval Facilities Engineering Command (NAVFAC). This includes the design and commissioning of an electromechanical emulation machine (EEM) similar to the systems analyzed and utilized in Chapters 4 & 5. The EEM consists of a permanent magnet generator and variable speed controller that will be utilized during field tests of hydrokinetic turbines. The intent is to fully develop all required data acquisition and control architecture in the lab such that the PTO is instantly integratable upon field deployment. This PTO would allow characterization and control to be performed on field-scale turbines deployed from a vessel. Turbine parameters and controllers could be iterated and optimized in the field at a scale above the critical Reynolds number and free of blockage, with a PTO suitable for efficient energy conversion.

6.5.2 Dynamic Simulation of an Isolated Grid with River Current Turbines

Cross-flow turbines are an attractive option for providing power to isolated loads or communities adjacent to fast-flowing streams or currents for reasons including relatively low mechanical complexity and the ability to densely pack them into arrays. However, the nature of the stream or current resource, namely the sensitivity of power output to minor changes in inflow velocity, may prove challenging for matching demand, as exemplified in Chapter 5. To further explore this concept, the grid of the village of Igiugig, Alaska could be modeled in the Simulink environment. Real and reactive power demand measured from the village could be used to specify dynamic loading conditions. Several cases may be modeled: first, a single RivGen turbine outputting power to the grid under maximum power-point tracking control in conjunction with a diesel generator to produce the balance of power, second, two RivGen turbines connected to the grid and a resistive load bank satisfying the entire demand with various control strategies, and finally, two RivGen turbines connected to the grid and a battery storage system. Results could be used to define appropriate control strategies for maintaining power quality and sufficiently meeting the demand of this community.

BIBLIOGRAPHY

[1] Ronald J Adrian and Jerry Westerweel. *Particle image velocimetry*. Number 30. Cambridge University Press, 2011.

[2] R. Alcorn and D. O'Sullivan. *Electrical Design for Ocean Wave and Tidal Energy Systems*. The Institution of Engineering and Technology, Stevenage, 2014.

[3] Matthias Arnold, Frank Biskup, and Po Wen Cheng. Load Reduction Potential of Variable Speed Control Approaches for Fixed Pitch Tidal Current Turbines. In *Proceedings of the 11th European Wave and Tidal Energy Conference*, pages 07C2–3–1:10, Nantes, France, 2015.

[4] Peter Bachant and M Wosnik. Reynolds Number Dependence of Cross-Flow Turbine Performance and Near-Wake Characteristics. In *Proceedings of the 2nd Marine Energy Technical Symposium*, Seattle, WA, 2014.

[5] Peter Bachant and Martin Wosnik. Performance measurements of cylindrical- and spherical-helical cross-flow marine hydrokinetic turbines, with estimates of exergy efficiency. *Renewable Energy*, 74:318–325, 2015.

[6] S. Baral, S. Budhathoki, and H. Prasad Neopane. Grid connection of micro hydropower, mini grid initiatives and rural electrification policy in nepal. In *Sustainable Energy Technologies (ICSET), IEEE Third International Conference on*, Kathmandu, Nepal, 2012.

[7] Matt Barone, Todd Griffith, and Jonathan Berg. Reference Model 2 : Rev 0 Rotor Design SAND2011-9306. Technical Report November, Sandia National Laboratories, Albuquerque, NM, 2011.

[8] Seifeddine Benelghali, M. E. H. Benbouzid, and J. F. Charpentier. Generator Systems for Marine Current Turbine Applications: A Comparative Study. *IEEE Journal of Oceanic Engineering*, 37(3):554–563, 2012.

[9] Seifeddine Benelghali, Mohamed El Hachemi Benbouzid, Jean Frédéric Charpentier, Tarek Ahmed-Ali, and Iulian Munteanu. Experimental Validation of a Marine Current Turbine Simulator: Application to a Permanent Magnet Synchronous Generator-Based System Second-Order Sliding Mode Control. *IEEE Transactions on Industrial Electronics*, 58(1):118–126, 2011.

[10] Muhammad Mahmood Aslam Bhutta, Nasir Hayat, Ahmed Uzair Farooq, Zain Ali, Sh. Rehan Jamil, and Zahid Hussain. Vertical axis wind turbine a review of various configurations and design techniques. *Renewable and Sustainable Energy Reviews*, 16(4):1926 – 1939, 2012.

[11] F D Bianchi, H Battista, and R J Mantz. *Wind Turbine Control Systems: Principles, Modelling, and Gain Scheduling Design.* Springer-Verlag Limited, London, UK, 2007.

[12] Amir Hossein Birjandi, John Woods, and Eric Louis Bibeau. Investigation of macro-turbulent flow structures interaction with a vertical hydrokinetic river turbine. *Renewable Energy*, 48:183–192, December 2012.

[13] Anne Blavette, Dara L O'Sullivan, Antony W Lewis, and Michael G Egan. Impact of a Wave Farm on its Local Grid: Voltage Limits, Flicker level, and Power Fluctuations. In *IEEE/MTS OCEANS12*, Yeosu, 2011.

[14] Marshall L Buhl et al. A new empirical relationship between thrust coefficient and induction factor for the turbulent windmill state. Technical report, 2005.

[15] R.J. Cavagnaro, J.C. Neely, F.-X. Fay, J. Lopez Mendia, and J.A. Rea. Evaluation of electromechanical systems dynamically emulating a candidate hydrokinetic turbine. *Sustainable Energy, IEEE Transactions on*, 7(1):390–399, Jan 2016.

[16] Robert J Cavagnaro. Impact of Turbulence on the Control of a Hydrokinetic Turbine. In *International Conference on Ocean Energy*, Halifax, Canada, 2014.

[17] Robert J Cavagnaro and Brian Polagye. Control of a helical cross-flow current turbine. In *Proceedings of the 3rd Oxford Tidal Energy Workshop, OTEW14*, Oxford, UK, 2014.

[18] Robert J Cavagnaro, Brian Polagye, and Brian Fabien. Control of a helical cross-flow current turbine. In *Proc. of the 2nd Marine Energy Technical Symposium*, Seattle, WA, 2014.

[19] Robert J Cavagnaro, Brian Polagye, Jim Thomson, Brian Fabien, Dominic Forbush, Levi Kilcher, James Donegan, and Jarlath McEntee. Emulation of a hydrokinetic turbine to assess control and grid integration. In *Proceedings of the 11th European Wave and Tidal Energy Conference*, Nantes, France, 2015.

[20] Salvador Ceballos, Judy Rea, Iraide Lopez, Josep Pou, Senior Member, Eider Robles, and Dara L O Sullivan. Efficiency Optimization in Low Inertia Wells Turbine-Oscillating Water Column Devices. 28(3):553–564, 2013.

[21] L. P. Chamorro, C. Hill, S. Morton, C. Ellis, R. E. a. Arndt, and F. Sotiropoulos. On the interaction between a turbulent open channel flow and an axial-flow turbine. *Journal of Fluid Mechanics*, 716:658–670, January 2013.

[22] L. P. Chamorro, C. Hill, V. S. Neary, B. Gunawan, R. E. a. Arndt, and F. Sotiropoulos. Effects of energetic coherent motions on the power and wake of an axial-flow turbine. *Physics of Fluids*, 27(5):055104–1:11, 2015.

[23] Claudio a Consul, Richard H J Willden, and Simon C McIntosh. Blockage effects on the hydrodynamic performance of a marine cross-flow turbine. *Philosophical transactions. Series A, Mathematical, physical, and engineering sciences*, 371:20120299, 2013.

[24] John O Dabiri. Potential order-of-magnitude enhancement of wind farm power density via counter-rotating vertical-axis wind turbine arrays. *Journal of Renewable and Sustainable Energy*, 3(4):043104, 2011.

[25] S. Djebarri, J.F. Charpentier, F. Scuiller, and M.E.H. Benbouzid. Influence of Fixed-Pitch Tidal Turbine Hydrodynamic Characteristic on the Generator Design. In *Proceedings of the 11th European Wave and Tidal Energy Conference*, pages 08A2–2–1:10, Nantes, France, 2015.

[26] D. Forbush and et al. Performance characterization of a river current turbine in shear flow. (Forthconming).

[27] J Freeman and M Balas. An investigation of variable speed horizontal-axis wind turbines using direct model-reference adaptive control. In *Proceedings of the 18th ASME Wind Energy Symposium*, number c, pages 66–76, Reston, VA, 1999. American Institute of Aeronautics and Astronautics.

[28] Chris Garrett and Patrick Cummins. The efficiency of a turbine in a tidal channel. *Journal of Fluid Mechanics*, 588:243–251, September 2007.

[29] B. Gaurier, G. Germain, J.V. Facq, C.M. Johnstone, A.D. Grant, A.H. Day, E. Nixon, F. Di Felice, and M. Costanzo. Tidal energy round robin tests comparisons between towing tank and circulating tank results. *International Journal of Marine Energy*, 12:87 – 109, 2015. Special Issue on Marine Renewables Infrastructure Network.

[30] Vincent J. Ginter and Jeff K. Pieper. Robust gain scheduled control of a hydrokinetic turbine. *IEEE Transactions on Control Systems Technology*, 19(4):805–817, July 2011.

[31] H. Glauert. The analysis of experimental results in the windmill brake and vortex ring states of an airscrew. Technical report, 1926.

[32] Bing Gong and Dewei Xu. Real time wind turbine simulator for wind energy conversion system. In *2008 IEEE Power Electronics Specialists Conference*, pages 1110–1114, Rhodes, June 2008. Ieee.

[33] M. S. Güney and K. Kaygusuz. Hydrokinetic energy conversion systems: A technology status review. *Renewable and Sustainable Energy Reviews*, 14(9):2996–3004, December 2010.

[34] M Hauck, A Rumeau, I Munteanu, A I Bratcu, S Bacha, D Roye, and A Hably. A 1 : 1 prototype of power generation system based upon cross-flow water turbines. In *IEEE International Symposium on Industrial Electronics (ISIE)*, pages 1414–1418, Hangzhou, 2012.

[35] Tiago A. de Jesus Henriques, Terry S. Hedges, Ieuan Owen, and Robert J. Poole. The Effect of Wave-Current Interaction on the Near-Wake of Horizontal Axis Tidal Stream Turbines. In *Proceedings of the 11th European Wave and Tidal Energy Conference*, number 1, pages 08D2–2–1:10, Nantes, France, 2015.

[36] Eastman N. Jacobs and Albert Sherman. AIRFOIL SECTION CHARACTERISTICS AS AFFECTED BY VARIATIONS OF THE REYNOLDS NUMBER, REPORt No. 586. Technical report, National Advisory Committee for Aeronautics, 1937.

[37] Kathryn E Johnson. Adaptive Torque Control of Variable Speed Wind Turbines Adaptive Torque Control of Variable Speed Wind Turbines. Technical Report August, National Renewable Energy Laboratory, Goldem Colorado, 2004.

[38] Kathryn E Johnson, Lucy Y Pao, Mark J Balas, and Lee J E E J Fingersh. Control of Variable Speed Wind Turbines: Standard and Adaptive Techniques for Maximizing Energy Capture. *Ieee Control Systems Magazine*, 26(3):70–81, 2006.

[39] Neil Kelley and Bonnie Jonkman. Turbsim. `http://wind.nrel.gov/designcodes/preprocessors/turbsim/`, Accessed 9/20/2014.

[40] L. Kilcher. Pyturbsim 0.4.2 documentation. `http://lkilcher.github.io/pyTurbSim/`, 2015.

[41] Levi F. Kilcher, Jim Thomson, and Jonathan Colby. Determining the spatial coherence of turbulence at mhk sites. In *Proceedings of the 2nd Marine Energy Technology Symposium, METS 2014, April 15-18*, pages 1–7, Seattle, WA, 2014.

[42] B.K. Kirke. Tests on ducted and bare helical and straight blade Darrieus hydrokinetic turbines. *Renewable Energy*, 36(11):3013–3022, nov 2011.

[43] Hossein Madadi Kojabadi, Liuchen Chang, Senior Member, and Tobie Boutot. Development of a Novel Wind Turbine Simulator for Wind Energy Conversion Systems Using an Inverter-Controlled Induction Motor. *IEEE Transactions on Energy Conversion*, 19(3):547–552, 2004.

[44] Jason Laks, Lucy Pao, Alan Wright, Neil Kelley, and Bonnie Jonkman. The use of preview wind measurements for blade pitch control. *Mechatronics*, 21(4):668–681, June 2011.

[45] T. Y. Liu, P. J. Tavner, Y. Feng, and Y. N. Qiu. Review of recent offshore wind power developments in china. *Wind Energy*, 16(5):786–803, 2013.

[46] Luiz a C Lopes, Josselin Lhuilier, Avishek Mukherjee, and Mohammad F. Khokhar. A wind turbine emulator that represents the dynamics of the wind turbine rotor and drive train. *PESC Record - IEEE Annual Power Electronics Specialists Conference*, 2005:2092–2097, 2005.

[47] Luksa Luznik, Karen a. Flack, Ethan E. Lust, and Katharin Taylor. The effect of surface waves on the performance characteristics of a model tidal turbine. *Renewable Energy*, 58:108–114, 2013.

[48] James F Manwell, Jon G McGowan, and Anthony L Rogers. *Wind energy explained: theory, design and application.* John Wiley & Sons, 2010.

[49] Marinet. Joint activities standardisation and best practices. `http://www.fp7-marinet.eu/standardisation&bestpractice_tidal_energy`, Accessed 5/18/2015.

[50] MATLAB. *Statistics and machine learning toolbox version 10.1 (R2015b)*. The MathWorks Inc., Natick, Massachusetts, 2015.

[51] W. J. McCroskey. The Phenomenon of Dynamic Stall. Technical report, AVRADCOM Research and Technology Laboratories, Moffett Field, California, 1981.

[52] Nobuhito Mori, Takuma Suzuki, and Shohachi Kakuno. Noise of Acoustic Doppler Velocimeter Data in Bubbly Flows. *Journal of Engineering Mechanics*, 133(1):122–125, 2007.

[53] Bruce R. Munson, Theodore H. Okiishi, and Donald F. Young. Fundamentals of fluid mechanics, 1990.

[54] I. Munteanu, S. Bacha, a.I. Bratcu, J. Guiraud, and D. Roye. Energy-Reliability Optimization of Wind Energy Conversion Systems by Sliding Mode Control. *IEEE Transactions on Energy Conversion*, 23(3):975–985, 2008.

[55] J Neely, S Glover, J Finn, F E White, B Loop, and O Wasynczuk. Wind turbine emulation for intelligent microgrid development. *Cyber Technology in Automation, Control, and Intelligent Systems (CYBER), 2012 IEEE International Conference on*, pages 28–33, 2012.

[56] Jason C Neely, Kelley M Ruehl, Richard A Jepsen, Jesse D Roberts, Steven F Glover, Forest E White, and Michael L Horry. Electromechanical Emulation of Hydrokinetic Generators for Renewable Energy Research. In *OCEANS'13 MTS/IEEE*, pages 1–8, San Diego, September, 2013.

[57] Adam Niblick. Experimental and analytical study of helical cross-flow turbines for a tidal micropower generation system. Master's thesis, The University of Washington, Seattle, WA, 2012.

[58] Kim Nielsen. Annex II - Development of Recommended Practices for Testing and Evaluating Ocean Energy Systems, Summary Report; Document No: T02-00. Technical report, OES-IA, 2010.

[59] Norman S Nise. *Control Systems Engineering, Sixth Edition.* John Wiley & Sons, Inc., Hoboken, NJ, 2011.

[60] P. Novak, T. Ekelund, I. Jovik, and B. Schmidtbauer. Modeling and control of variable-speed wind-turbine drive-system dynamics. *IEEE Control Systems Magazine*, 15(4):28–38, 1995.

[61] American Society of Mechanical Engineers. Test uncertainty. Standard PTC 19.1-2005, ASME, 2005.

[62] Ion Paraschivoiu. *Wind turbine design: with emphasis on Darrieus concept.* Presses inter Polytechnique, 2002.

[63] Luca Peretti, Ville Särkimäki, and Jan Faber. A wind turbine emulator for generator control algorithm development. In *ICIT 2013 - 2013 IEEE International Conference on Industrial Technology (ICIT)*, pages 228–233, Cape Town, 2013.

[64] B. Polagye, J. Epler, and J. Thomson. Limits to the Predictability of Tidal Current Energy. In *MTS/IEEE Oceans 2010*, Seattle, WA, 2010.

[65] Brian Polagye, Robert Cavagnaro, and Adam Niblick. Micropower from tidal turbines. In *Proceedings of the ASME Fluids Division Summer Meeting*, Incline Village, NV, 2013.

[66] B. Rabelo, W. Hofmann, and M. Glück. Emulation of the static and dynamic behaviour

of a wind-turbine with a DC-machine drive. *PESC Record - IEEE Annual Power Electronics Specialists Conference*, 3:2107–2112, 2004.

[67] J. Rea, J. Kelly, R. Alcorn, and D. O'Sullivan. Development and operation of a power take off rig for ocean energy research and testing. In *Proceedings from the 9th European Wave and Tidal Energy Conference*, Southampton, UK, 2011.

[68] J. B. Richard, J. Thomson, B. Polagye, and J. Bard. Method for identification of doppler noise levels in turbulent flow measurements dedicated to tidal energy. *International Journal of Marine Energy*, 3(4):52–64, 2013.

[69] Fredrik Roos, Hans Johansson, and Jan Wikander. Optimal selection of motor and gearhead in mechatronic applications. *Mechatronics*, 16(1):63–72, February 2006.

[70] S H Salter. Are Nearly all Tidal Stream Turbine Designs Wrong? In *4th International Conference on Ocean Energy*, pages 1–7, Dublin, IE, 2012.

[71] Ruben Sanchez. Technology Readiness Assessment Guide, DOE G 413.3-4A. Technical report, US Department of Energy, Washington, D.C., 2011.

[72] D. Schlipf, D. J. Schlipf, and M. Kühn. Nonlinear model predictive control of wind turbines using LIDAR. *Wind Energy*, 16:1107–129, 2013.

[73] Mitsuhiro Shiono, Katsuyuki Suzuki, and Seiji Kiho. An experimental study of the characteristics of a Darrieus turbine for tidal power generation. *Electrical Engineering in Japan*, 132(3):38–47, aug 2000.

[74] Benjamin Strom. The influence of reynolds number on lift type cross flow turbine performance and optimization. In preparation.

[75] Benjamin Strom, Steve Brunton, and Brian Polagye. Consequences of Preset Pitch Angle on Cross-Flow Turbine Hydrodynamics. In *Proceedings of the 11th European Wave and Tidal Energy Conference*, number 4, pages 08D2–4–1:9, Nantes, France, 2015.

[76] Xiaojing Sun, Diangui Huang, and Guoqing Wu. The current state of offshore wind energy technology development. *Energy*, 41(1):298 – 312, 2012. 23rd International Conference on Efficiency, Cost, Optimization, Simulation and Environmental Impact of Energy Systems, {ECOS} 2010.

[77] J. Kristian Sveen. *An introduction to MatPIV v. 1.6.1.* Dept. of Math. University of Oslo, eprint series, ”mechanics and applied mathematics”, no. 2 issn 0809-4403 edition, August 2004.

[78] G. I. Taylor. The Statistical Theory of Isotropic Turbulence. *Journal of the Aeronautical Sciences*, 4(8):311–315, 1937.

[79] F Thiebaut, Dara L O'Sullivan, S Ceballos, J Lpez, J Boake, N Bard, J Brinquete, L Varandas, M Gato, and R Alcorn. Testing of a floating OWC device with movable guide vane impulse turbine power take-off. In *Proceedings of the 9th European Wave and Tidal Energy Conference*, Southampton, UK, 2011.

[80] Jim Thomson, Levi Kilcher, Marshall Richmond, Joe Talbert, Alex DeKlerk, Brian Polagye, Maricarmen Guerra, and Rodrigo Cienfuegos. Tidal turbulence spectra from a compliant mooring. In *Proceedings of the 1st Marine Technology Symposium*, pages 1–9, Washington, D.C., 2013.

[81] Jim Thomson, Brian Polagye, Vibhav Durgesh, and Marshall C. Richmond. Measurements of turbulence at two tidal energy sites in puget sound, WA. *IEEE Journal of Oceanic Engineering*, 37(3):363–374, July 2012.

[82] Richard E Thomson and William J Emery. *Data analysis methods in physical oceanography.* Elsevier Science, Amsterdam, 2001.

[83] Maria Andreica Vallet, Seddik Bacha, Iulian Munteanu, Antoneta Iuliana Bratcu, and Daniel Roye. Management and control of operating regimes of cross-flow water turbines. *IEEE Transactions on Industrial Electronics*, 58(5):1866–1876, May 2011.

[84] Na Wang, Kathryn E. Johnson, and Alan D. Wright. FX-RLS-based feedforward control for LIDAR-enabled wind turbine load mitigation. *IEEE Transactions on Control Systems Technology*, 20(5):1212–1222, September 2012.

[85] Jochem Weber, Ronan Costello, and John Ringwood. WEC Technology Performance Levels (TPLs) - Metric for Successful Development of Economic WEC Technology. In *10th European Wave and Tidal Energy Conference*, Aalborg, Denmark, 2013.

[86] J. I. Whelan, J. M. R. Graham, and J. Peiró. A free-surface and blockage correction for tidal turbines. *Journal of Fluid Mechanics*, 624(March 2009):281, March 2009.

[87] J I Whelan and T Stallard. Arguments for modifying the geometry of a scale model rotor. In A.S. Bahaj, editor, *Proceedings of 9th European Wave and Tidal Energy Conference*, Southampton, 2011.

Appendix A

CONTROL EXPERIMENTS ON A HELICAL CROSS-FLOW TURBINE

This early work of laboratory-scale turbine control is included as an appendix to provide an example of the importance of understanding the implications of prototype scale and turbine dynamics in the development of effective control schemes. Many assumptions made in the work are no longer considered best practices, as the previous chapters have demonstrated. However, the results are likely still reasonable. The majority of the text was published in the *Proceedings of the 2nd Marine Energy Technology Symposium, Global Marine Renewable Energy Conference* in April, 2014. It has been modified to include reference to other chapters in this document. Additional discussion on the relevance of this work is added. The citation for the original document is as follows:

Cavagnaro, R., B. Fabien, and B. Polagye (2014) Control of a helical cross-flow current turbine, *Proceedings of the 2nd Marine Energy Technology Symposium, Global Marine Renewable Energy Conference*, Seattle, WA, April 15-17

A.1 Introduction

A preview-based variable-speed turbine control strategy (Chapter 1, (1.14)) is enacted to maintain optimal performance of a laboratory-scale fixed-pitch helical CFT. Three variations of the scheme are implemented experimentally. These strategies are simulated numerically and compared to a simulation of operation at constant rotation rate. Performance, benefits, and challenges associated with the experimental control implementation are discussed.

A.2 Methods

A.2.1 Turbine and Test Rig Description

The four-bladed, cross-flow helical turbine (Figure A.1) is a quarter-scale geometrically-scaled model of the field-scale turbine evaluated in Chapter 3, and identical to the scaled turbine whose stability was characterized in Chapter 2 except for the preset pitch angle of its blades.

The laboratory test rig, an earlier version of the setup described in Chapter 2, consisted of an optical encoder to measure angular position used to determine rotation rate (ω_t), a controllable particle brake to provide a resistance to rotation, a reaction torque cell to measure the torque resisting rotation, and an ADV positioned 7D upstream to measure the free-stream velocity (U_∞). As only τ_c in opposition to acceleration could be applied by the particle brake, direct control of rotor speed, which may require power input from a PTO, was not possible. More recent work indicates the ability to control the rotation rate of a turbine has many advantages, as noted in Chapter 2. Flume velocity was controlled by an adjustable recirculation pump frequency. The torque measurement was considered the sum of τ_c applied by the brake, and torques associated with bearing friction, vibration, and other losses, (τ_m). For experimental testing, it was assumed τ_c was much greater than τ_m, and the latter was neglected - an assumption no longer necessary with direct measurement of all system torques in an updated test rig.

Turbine and flume dimensions lead to an average blockage ratio as defined in (2.1) of 15%. Blade-chord Reynolds numbers, calculated as in (1.37) achieved during experiments were in a transitional range from $2x10^4$ to $3x10^4$. The range of Froude number based on an average water depth of 0.47 m was 0.12 - 0.15. Flume turbulence intensity under steady-flow conditions was approximately 4%.

Table A.1: Micropower rotor parameters.

Parameter	**Value**
Blade profile	NACA 0018
Turbine diameter (D)	0.172 m
Turbine height (H)	0.234 m
Turbine aspect ratio (H/D)	1.36
Helical pitch angle	60°
Blade chord length	0.04 m
Blade thickness	0.0073 m
Solidity ratio	0.30

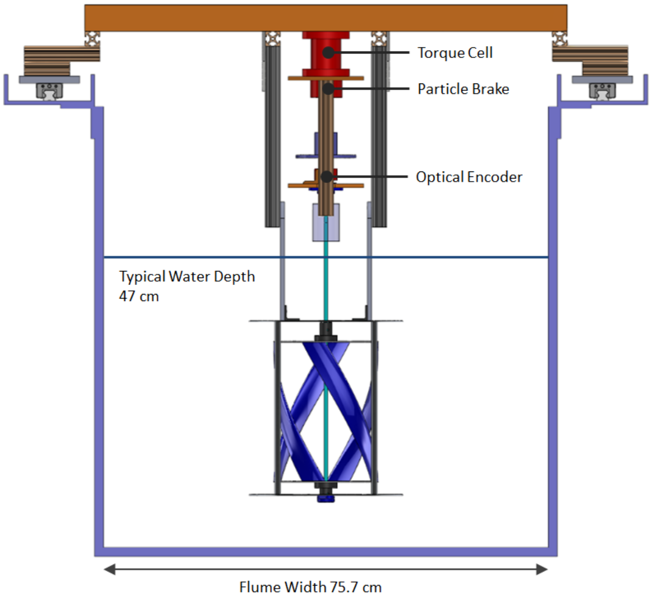

Figure A.1: Lab-scale turbine and experimental test rig utilized for control experiments.

A.2.2 Performance Characteristics

As in previous chapters, the performance of a hydrokinetic turbine was defined by a characteristic curve relating the coefficient of performance (C_P) to the tip speed ratio (λ). As a consequence of experimental blockage at a transitional Reynolds number, multiple performance curves that are a function of inflow velocity existed for this iteration of the laboratory-scale turbine [17]. For a field-scale turbine, variable efficiency for balance of system components (e.g., gearbox, generator) can produce a family of maximum power points with inflow velocity dependence, as demonstrated in Chapter 3. Therefore, a controller that can adapt to a time-varying maximum power point was desirable.

A set of idealized performance curves for inflow velocity ranging from 0.55 m/s to 0.70 m/s are shown in Figure A.2. Third-order polynomials were fit to the experimental data to obtain continuously differentiable curves. Optimal C_P and corresponding λ estimates were approximated as a linear function of inflow velocity.

A.2.3 Disturbance Characteristics

As inflow velocity cannot be controlled in a natural environment, it is considered to be a variable disturbance to the system. A series of velocity profiles (Figure A.3) were obtained by manually keying the flume pump controller through a predetermined sequence. Current velocity was measured using the analog output from a Nortek Vector ADV and post-processed to remove statistical outliers [52]. Though each test comprised an independently performed experiment with a slightly different time series, the inflow conditions and velocity were similar for all experiments. The velocity measurements were not smoothed for use in the control schemes in an attempt to allow the controller to react to turbulence at all measured scales, although later analysis and much of the work in previous chapters indicates the turbine is naturally unable to respond to high frequency turbulence or control action.

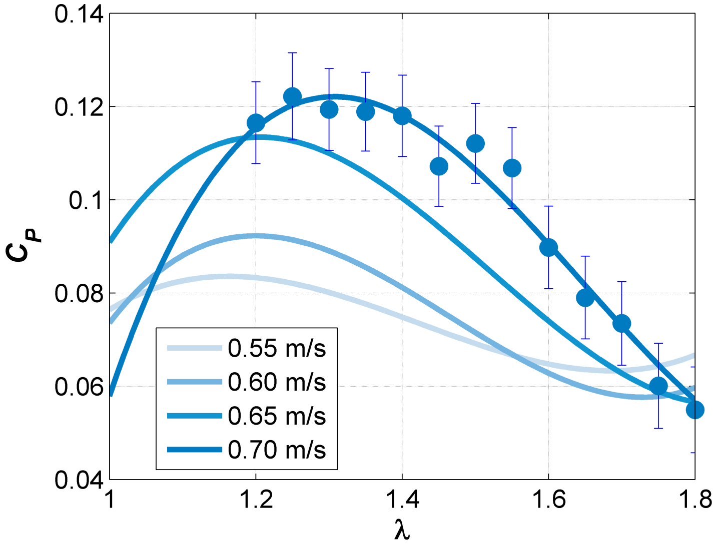

Figure A.2: Performance curves with typical experimental scatter and uncertainty shown for an inflow velocity of 0.7 m/s.

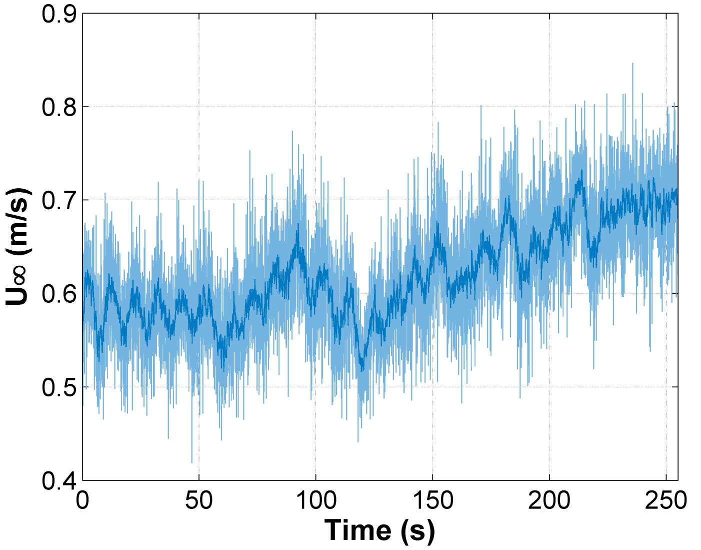

Figure A.3: Typical inflow velocity for controller validation, raw (fine line, 100 Hz) and smoothed (10 Hz).

A.2.4 Experimental Control Strategies

The experimental turbine's rotation rate was adjusted by varying the voltage supplied to the particle brake. Neglecting a damping term, for which a suitable estimate was unavailable at the time, the dynamics of the turbine were modeled as a simplified version of (1.6) in the following treatment as

$$\dot{\omega}_t = \frac{1}{J_{eq}}(\tau_h - \tau_c), \tag{A.1}$$

an assumption no longer considered best practice. Hydrodynamic and control torque were considered equal in this formulation when the turbine's rotation rate was steady. Three variations on a torque control scheme were evaluated for their ability to optimize mechanical power generation. In order of increasing complexity, these variations were constant gain control, feedforward adaptive gain control, and hybrid feedback/feedforward adaptive gain control. These were specific implementations of the controller topologies described in Chapter 1.

For all three schemes, the control torque was related to peak C_P at a corresponding λ^* as

$$\tau_c = \left(\frac{1}{2}\rho A r^3 \frac{C_{Pmax}}{\lambda^{*3}}\right)\omega_t^2 = K\omega_t^2 \tag{A.2}$$

where K is the control law gain [37]. This controller was implemented in emulation in Chapters 4 and 5. In the case of a unique maximum power point, K is time invariant. Linearizing C_{Pmax} and λ^* as functions of velocity for the experimental performance curves (Figure A.2), the adaptive gain, defined as K^*, becomes

$$K^* = \frac{1}{2}\rho A r^3 \frac{[0.273U_\infty - 0.068]}{[0.920U_\infty + 0.645]^3} \tag{A.3}$$

and is a non-linear function of inflow velocity (U_∞). The control torque was dominated by the ω_t^2 term, which was on the order of 10^2, while the gain (K) was on the order of 10^{-4}. Therefore, slight changes in the inflow velocity (and, subsequently, K^* for adaptive schemes) were expected to have limited effect on control torque command, as $\frac{dK^*}{dU_\infty} \approx 10^{-4}$.

Control schemes were evaluated by comparing the average power produced during an experiment to the power that would result from the turbine operating at C_{Pmax} for the same experimental velocity time series. The ratio of these quantities forms a non-dimensional term (P_{loss}) as

$$P_{loss} = 1 - \frac{\bar{P}_{actual}}{\bar{P}_{ideal}}. \tag{A.4}$$

This evaluation method assumed previously derived performance curves perfectly defined optimal performance points, when in actuality, there was considerable uncertainty ($\approx 10\%$ of C_P) associated with them. A calculation of uncertainty for a performance curve power point is presented in Appendix B. Consequently, for the experimental measurements it was possible for the actual performance to exceed the "ideal" performance due to this uncertainty, and a discovery made after the conclusion of this work that rotor efficiency is improved through rapid oscillations of τ_c, as was applied here. This was not the case for the numerical simulations described later in this appendix.

Each control strategy was implemented in LabVIEW. A Virtual Instrument (VI) was created to collect angular position, torque, and inflow velocity utilizing a data acquisition board (National Instruments USB-6341) at a sampling rate of 100 Hz. The sampling rate was chosen to enable measurement of the turbulent fluctuations of inflow velocity on a small time-scale. Moving average smoothing of the previous 10 samples was performed on calculations of ω_t prior to computation of the control torque setpoint to reduce short-term variability in ω_t. τ_c was computed at each time step utilizing ω_t and, for some schemes, U_∞ measured at the beginning of the time step. Control actions were accomplished by setting the voltage level of the particle brake (Placid Industries B2-12-1) power supply. The voltage command was set to saturate at 4 V, introducing a nonlinear element that provided robustness for strong perturbations associated with spikes in ω_t or U_∞. A higher saturation voltage caused the turbine to experience system stall if control torque was suddenly elevated. This was likely the result of turbulent gusts temporarily increasing the rotor speed, to which the controller overcompensated for; τ_c was set too high for the turbine to recover from once the gust had passed (Chapter 2).

The dynamic response of the controlled turbine was characterized by computing power spectra for the inflow power and mechanical power output. Time series from each test were

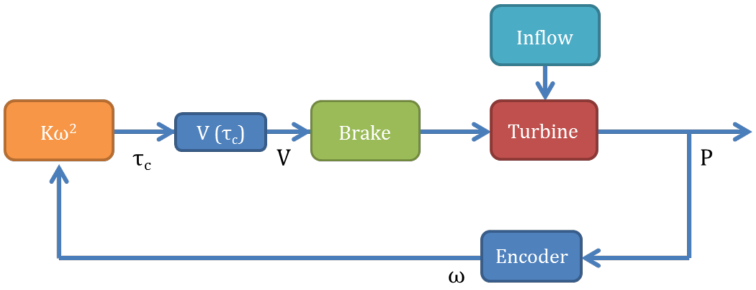

Figure A.4: Block diagram of constant gain scheme.

divided into ≈20 s windows with 50% overlap before application of a fast Fourier transform with a Hamming filter.

A.2.4.1 Constant Gain Control Implementation

The simplest of the controllers, constant gain (Figure A.4), was implemented by computing a value for K from a single characteristic maximum power point corresponding to a velocity of 0.63 m/s using (A.3) (average velocity for the experimental sequence). Torque command was a nonlinear function only of the measured turbine rotation rate. The applied torque was found to have a quadratic relationship to brake command voltage (determined in previous experimentation), which was solved for each loop iteration to obtain the appropriate voltage command. In the absence of torque feedback, this controller assumed the relationship between the brake command and actual applied braking torque was perfectly modeled.

A.2.4.2 Feedforward Adaptive Gain Control Implementation

For the feedforward with adaptive gain controller implementation (Figure A.5), the previous scheme was modified to include velocity measurements in the computation of K. The gain was adapted based on upstream velocity (A.3).

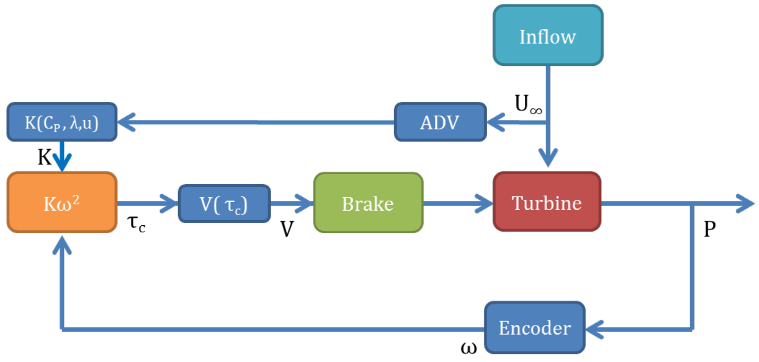

Figure A.5: Block diagram of feedforward adaptive control scheme.

A.2.4.3 Hybrid Feedback/Feedforward Control Implementation

The most complex of the controllers introduced a torque feedback loop, replacing direct brake control - a practice now considered standard for controller implementation. At the beginning of each loop iteration, the control torque measurement was fed into a PI control VI where it was compared to the control torque setpoint. The control action set the particle brake command voltage. Initially, a LabVIEW auto-tuning function was used to coarsely set PI gains. These gains were manually adjusted from their baseline values through a process of trial and error to maintain smooth rotation through all operating conditions tested, including cut-in during a ramp-up of inflow velocity and cut-out during a ramp-down of inflow velocity. A block diagram depicting this control scheme is shown in Figure A.6.

A.2.5 Numerical Simulations

The effectiveness of the control algorithms was also investigated with time-domain analyses of constant-speed control (i.e., constant rotation rate), feedforward adaptive gain control, and constant gain control. For the constant gain case, controller gain was simulated for the average velocity of the time series, as well as for poor guesses of velocity less than and greater than the mean. The idealized characteristic curves used to identify the maximum

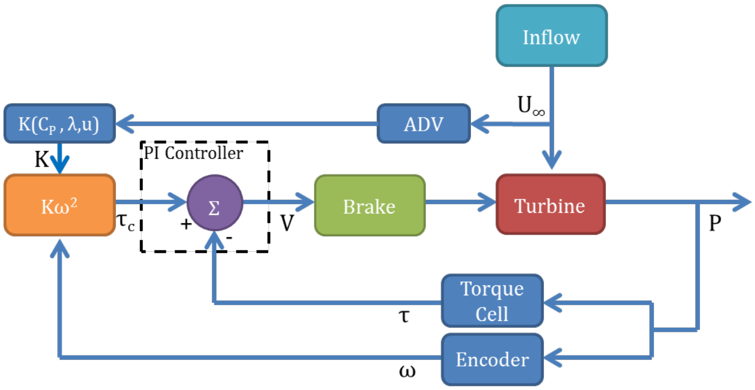

Figure A.6: Block diagram of hybrid control scheme.

power point were also used for the control simulation (Figure A.2). However, for simulation, two-dimensional interpolation was performed on the families of performance curves to calculate hydrodynamic performance and the controller gain at each time step. These curves defined both the turbine performance and controller gain, whereas in the experiments, the controller gain was defined by the curves, but turbine performance could depart from these curves (i.e., the characteristic curves describe average, not instantaneous performance for the experiment).

Simulations were performed using a single, despiked velocity time series from the experiments. At time $t = 0$, the simulation was initialized with a rotation rate corresponding to optimal performance at the initial velocity. The simulation then stepped through time ($\Delta t = 0.005$ s) with the turbine rotation rate evolving as

$$\omega_{t,i+1} = \omega_{t,i} + \dot{\omega}_t \Delta t \tag{A.5}$$

where $\dot{\omega}_t$ and K were determined as for the experiments. For the constant rotation rate case, $\dot{\omega}_t$ was taken to be zero for all time - an assumption no longer considered valid, as a turbine's finite inertia plays a critical role in system performance for a constant speed controller under torque regulation. At each time step, both the power produced by the turbine and power that would have been produced if the turbine was operating at maximum efficiency was calculated and P_{loss} evaluated for the full time series.

The moment of inertia estimated for this implementation was roughly double that measured for the nearly identical rotor studied in Chapter 2. However, differences in in-line components comprising the test setups (e.g., particle brake vs. servomotor) likely account for this discrepancy.

A.3 Results

A.3.1 Experimental Controller Performance

Ideal power was compared against the actual power to evaluate controller performance. The time series for the hybrid controller (Figure A.7) indicates the controller was generally successfully at tracking target power, with a tendency to undershoot by a small amount (moving average smoothing over 0.5 s was performed for ease of visualization). Changes to the bulk flow (on the order of seconds) were handled well by the hybrid controller. The constant gain and adaptive gain feedforward controllers performed similarly, with a higher degree of undershoot. Power loss for the three controllers is summarized in Table A.2. The hybrid controller outperformed both feedforward adaptive gain and constant gain control. Unexpectedly, constant gain control performed slightly better than feedforwad control with adaptive gain. This result may have been a combination of uncertainty in the performance curves used to derive adaptive gain values and the control scheme's low sensitivity to changes in velocity. Additionally, the adaptive controller did not account for advection of measured disturbances upstream in the flow to the turbine. In more recent work, this was shown to improve correlation between ADV measurements and changes in ω_t (Chapter 2). The improvement in performance due to the feedback loop of the hybrid control is attributed to this scheme's ability to ensure the commanded control torque is achieved, a feature absent in the other two controllers and later considered standard practice.

Response to turbulent fluctuations at higher frequencies was evaluated by comparing

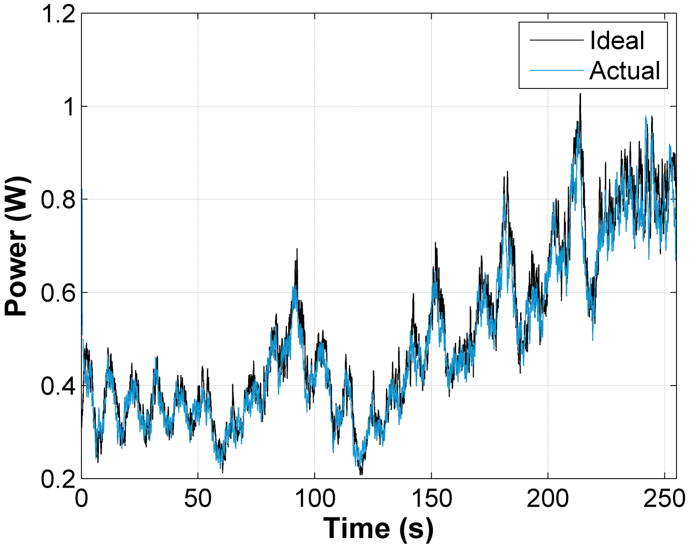

Figure A.7: Hybrid controller performance.

the power spectra of turbine power output and inflow power (Figure A.8). The range of turbine rotational frequency (between vertical lines) corresponded to a wide plateau in the power output spectra associated with control actions. A steep drop-off occurs beyond 1.8 Hz, indicating the system was non-responsive to turbulence on time scales on the order of $\approx$ 0.5 s or faster. The upward trend in the output power spectrum above 5 Hz is thought to be the product of experimental noise; the torque sensor was sensitive to high frequency vibration of the flume and test frame. This result informed future designs of experimental test rigs with isolated force sensing from the flume. All control schemes exhibited similar dynamic characteristics.

A.3.2 Numerical-Experimental Comparison

P_{loss} for each case is listed in Table A.2. For the numerical simulations, turbine performance under feedforward control with adaptive gain was within a few percent of ideal performance. Because the controller gain was dominated by variations in ω_t^2, performance under feedfor-

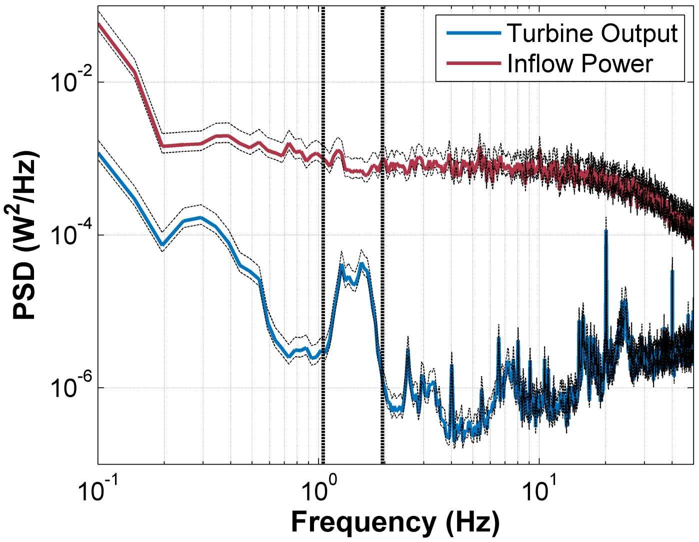

Figure A.8: Experimental power spectra with primary rotational frequency range (solid vertical lines).

ward control with constant gain, even with a poor assumption for inflow velocity, was only somewhat worse than adaptive feedforward control. However, constant speed control (simulation) performed significantly worse than any of the torque control simulations, reducing power generation by 21% relative to an ideal system in simulations. The unrealistic nature of the implementation of the constant speed controller casts some doubt on this result.

A.4 Discussion and Conclusions

An adaptive gain control scheme for a laboratory-scale hydrokinetic turbine was implemented, allowing the turbine to remain close to its maximum power point despite inflow disturbance. The turbine performance was such that the maximum power point was close to λ_c conditions and PI controller gains needed to be tuned to prevent system stall for the hybrid scheme or allowed to saturate for feedforward control. This highlights the importance of understanding rotor stability, as investigated in Chapter 2, or regulating the turbine with

Table A.2: P_{loss} for experiments and simulations.

	Experiment	**Simulation**
Constant Speed	N/A	21%
Constant Gain		
$U_{guess} = 0.63$ m/s	11%	3%
$U_{guess} = 0.5$ m/s	N/A	5%
Feedforward adaptive gain	12%	2%
Feedback/Feedforward adaptive gain	4%	N/A

a PTO capable of controlling rotor speed.

The turbine considered in this investigation had a family of characteristic performance curves that were a function of inflow velocity, similar to overall system efficiency of the field-scale rotor of Chapter 3. For such a system, an adaptive control technique may be applicable and worthwhile to investigate. However, the benefits of preview may be unapparent on many systems with relatively low time constants, for which reaction time is fast enough for a constant gain optimal controller to maintain near ideal performance.

Experiments with the described control techniques were only used for Region 2 control where performance optimization is the goal. Preview-based methods may also have utility for Region 3 control, where maintaining operation at rated power is the goal, and for smooth transitions between these regions. The latter objective appears promising, as abrupt changes to the control method can be eliminated by anticipating switches to and from constant power output, obviating the need for a separate "Region 2.5" control scheme [44].

More advanced control strategies, investigation into the role of sensor noise in performance, and the effects of filtering have since been the topics of investigation into active regulation of CFTs. Though the work presented in this chapter is somewhat primitive when compared to the later work (primarily conducted by other researchers in the Marine Renewable Energy Lab), it laid the groundwork and uncovered fundamental challenges to controlling laboratory-scale turbines and demonstrated the importance of understanding stability at low λ. Additionally, the adaptive controller whose performance is described in this chapter was reevaluated with the turbine and test setup of Chapter 2 over a wider range of U_∞. Results were nearly identical, with a constant gain controller performing no worse or better than the adaptive scheme.

Appendix B

EXPERIMENTAL UNCERTAINTY IN A PERFORMANCE CHARACTERIZATION

The following work appears as an appendix in the published version of Chapter 3, Cavagnaro, R. J., Polagye, B., Field Performance Assessment of a Hydrokinetic Turbine, *International Journal of Marine Energy (IJOME)*, (*in press*), doi: 10.1016/j.ijome.2016.01.009.

B.1 Instrumentation Uncertainty

In Tables B.1 & B.1, systematic uncertainty for each of the sensors used for field and dynamometry testing of Chapter 3 is compiled based on manufacturers' specifications and sensor calibrations. A description of the nature and probable cause of random errors is also presented.

B.2 Uncertainty Formulation

Uncertainty is estimated for each point on the turbine performance curve ($C_P(\lambda)$) following the standard on test uncertainty, ASME PTC 19.1-2005 [61]. Random errors are quantified as the standard uncertainty of the sample mean, defined as

$$s_{\bar{X}} = \sqrt{\frac{1}{N}\sum_{j=1}^{N}\frac{(X_j - \bar{X})}{N-1}} \tag{B.1}$$

where $\bar{X}$ is the sample mean, N the number of data points, X_j each sample point. Also known as the standard deviation of the mean, this quantity is the standard deviation of the sample normalized by the root of the number of data points collected and reflects the value of increasing the sample size in reducing uncertainty and gaining confidence in the mean.

Table B.1: Tow testing instrument uncertainty

Instrument	Measured Quantity	Units	Systematic Uncertainty	Random Uncertainty
Nortek Vector ADV	Inflow water velocity	m/s	Sensor accuracy: ± 0.5% of measured value ± 1 mm/s	Uniformly distributed Doppler noise, normally distributed variation in tow speed
RLS RM22 magnetic encoder	Rotor angular position	radians	Sensor accuracy: ± 0.012	Normally distributed variation in rotation rate
LEM LA 55-P current transducer	Generator electrical current	Amperes	Sensor accuracy: ± 0.9% of measured value	White electrical noise, normally distributed variation in current
LEM LV 25-P voltage transducer	Generator voltage	Volts	Sensor accuracy: ± 0.9% of measured value	White electrical noise, normally distributed variation in voltage
Futek TRS605 rotary torque sensor	Hydrodynamic torque	Nm	Sensor accuracy: ± 0.03 Nm from nonlinearity hysteresis and nonrepeatability	Normally distributed variation in torque

Table B.2: Dynamometry testing instrument uncertainty

Instrument	**Measured Quantity**	**Units**	**Systematic Uncertainty**	**Random Uncertainty**
Encoder Products model 260 optical encoder	Generator angular position	radians	Sensor accuracy: ± 0.00017	Normally distributed variation in rotation rate
LEM LA 55-P current transducer	Generator electrical current	Amperes	Sensor accuracy: ± 0.9% of measured value	White electrical noise, normally distributed variation in current
LEM LV 25-P voltage transducer	Generator voltage	Volts	Sensor accuracy: ± 0.9% of measured value	White electrical noise, normally distributed variation in voltage
Futek TFF425 reaction torque sensor	Generator reaction torque	Nm	Calibration uncertainty: ± 4.0% of measured value, based on calibration of torque sensor in dynamometry configuration	Normally distributed variation in torque

Systematic uncertainties, defined as the constant component of error in a measurement, are estimated to the best of the experimenters' knowledge from instrument specification sheets and calibration data. Standard systematic uncertainties are denoted as $b_{\bar{X}}$. The total uncertainty for any individual test quantity is sum of the squares of the random and systematic uncertainty,

$$u_{\bar{X}} = \sqrt{(b_{\bar{X}})^2 + (s_{\bar{X}})^2}. \tag{B.2}$$

For 95% confidence levels, the uncertainty is defined for large N as,

$$U_{\bar{X}} = 2u_{\bar{X}} \tag{B.3}$$

resulting in a final value of,

$$\bar{X} \pm U_{\bar{X}}. \tag{B.4}$$

When the desired result is the function of multiple variables,

$$R = f(\bar{X}_1, \bar{X}_2, ..., \bar{X}_I) \tag{B.5}$$

sensitivity is defined as

$$\theta_i = \frac{\partial R}{\partial \bar{X}_i} \tag{B.6}$$

such that the absolute random standard uncertainty for a test result is

$$s_R = \sum_i^I [(\theta_i s_{\bar{X}_i})^2]^{\frac{1}{2}} \tag{B.7}$$

and likewise for the systematic uncertainty,

$$b_R = \sum_i^I [(\theta_i b_{\bar{X}_i})^2]^{\frac{1}{2}}. \tag{B.8}$$

Combining the two, the total uncertainty with 95% confidence is

$$U_{R,95} = 2\sqrt{(s_R)^2 + (b_R)^2}. \tag{B.9}$$

B.3 Uncertainty in typical test case

An uncertainty calculation for a C_P measurement from Chapter 3 for a typical test case (1.6 m/s nominal tow speed, maximum performance) is presented as a tutorial example. The turbine radius, height, and water density are assumed to have no significant uncertainty. Restated, the kinetic power efficiency of the rotor is,

$$C_P = \frac{\tau_h \omega_t}{\frac{1}{2}\rho A {U_\infty}^3}. \tag{B.10}$$

Sensitivities can be analytically found,

$$\theta_{\tau_h} = \frac{\partial C_P}{\partial \tau_h} = \frac{2\omega_t}{\rho A {U_\infty}^3} = \frac{C_P}{\tau_h} \tag{B.11}$$

$$\theta_{\omega_t} = \frac{C_P}{\omega_t} \tag{B.12}$$

$$\theta_{U_\infty} = \frac{-3C_P}{U_\infty}. \tag{B.13}$$

A tabulation of uncertainty is presented in the style of the ASME standard in Table B.3.

This analysis shows measurement of C_P was most sensitive to changes in inflow velocity due to the cubic dependency. Consequently, the velocity measurement contributes the greatest experimental uncertainty.

Table B.3: Uncertainty calculation for C_P, nominal 1.6 m/s, max efficiency

Independent Parameters								
Symbol	Description	Unit	Nominal value	Absolute systematic standard uncertainty $b_{\hat{X}_i}$	Absolute random standard uncertainty $s_{\hat{X}_i}$	Absolute sensitivity θ_i	Absolute systematic standard uncertainty contribution $(\theta_i b_{\hat{X}_i})^2$	Absolute random standard uncertainty contribution $(\theta_i s_{\hat{X}_i})^2$
θ_h	Hydrodynamic torque	Nm	44.87	0.03	0.0146	0.0038	$1.32x10^{-8}$	$3.14x10^{-9}$
ω_t	Rotation rate	rad/s	5.97	0.012	0.0098	0.0288	$1.19x10^{-8}$	$8.00x10^{-8}$
U_∞	Inflow velocity	m/s	1.62	0.009	0.001	-0.319	$8.40x10^{-6}$	$9.42x10^{-8}$
ρ	Water density	kg/m^3	1000	NA				
A	Projected area	m^2	0.733	NA				
Calculated Result								
Symbol	Description	Unit	Nominal value	Absolute systematic standard uncertainty, b_r	Absolute random standard uncertainty s_r	Absolute combined standard uncertainty u_r	Absolute expanded (95%) uncertainty, U_r	
C_P	Coefficient of performance	-	0.172	0.0029	0.0004	0.003	**0.006**	

Appendix C

COMPARISON OF LABORATORY AND FIELD PERFORMANCE

Torque control was utilized to characterize the performance of both a field (Chapter 3) and lab-scale turbine (Chapter 2). The laboratory rotor's dimensions are $\frac{1}{4}$ of the field rotor's. As discussed in Chapter 1, similar performance of a small-scale turbine may be achieved if a minimum value of Re_c is achieved. Upon reaching Reynolds independence, it is hypothesized laboratory and field scale performance would agree. Utilizing kinematic viscosity for water at 16°C ($1.1x10^{-6}$ m^2/s), maximum Re_c was obtained for laboratory experiments at U_∞ of 1.2 m/s, yielding a value of $4.4x10^4$. Minimum Re_c was obtained for the field-scale turbine (tested at a similar water temperature) at the slowest tow speed of 1.0 m/s, yielding a value of $1.5x10^5$. Therefore, field testing was conducted under conditions leading to Re_c at least 3.4-times as high as lab testing. A comparison of laboratory and field performance results is shown in Figure C.1. $C_P(\lambda)$ appears qualitatively similar at the slowest field-scale tow speed and highest laboratory-scale flume speed. However, there is no evidence to suggest performance would not continue to increase for the laboratory-scale turbine at higher Re_c than was achievable due to limitations of the flume. Additionally, the confounding effect of blockage, present at the laboratory scale but negligible in the field experiments, is likely boosting the smaller turbine's C_P and shifting it towards higher λ [17]. At the field scale, it appears the turbine is achieving Reynolds independence, as discussed in Chapter 3. Therefore, strong conclusions about similar performance cannot be claimed. Ongoing work is intended to enhance understanding of the relationship between turbine performance and Reynolds number through parametric studies at the laboratory-scale, and characterization of field-scale rotors on a vessel-based test platform.

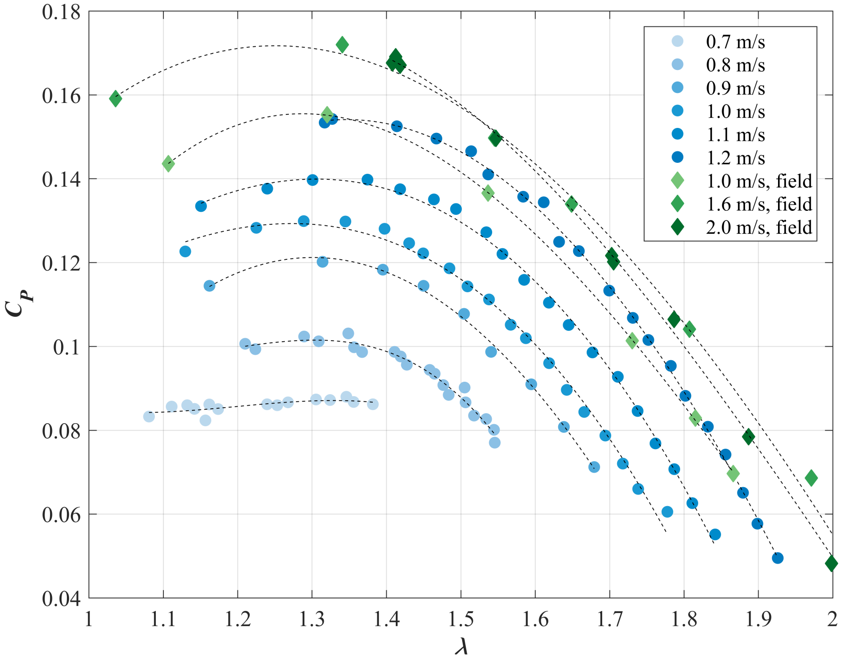

Figure C.1: Comparison of field and laboratory-scale performance.